The Dissertation Committee for Thomas Dominique Deconinck
certifies that this is the approved version of the following dissertation:

Simulation Studies of Direct-Current Microdischarges for Electric Propulsion

Committee:

Laxminarayan L. Raja, Supervisor

Noel T. Clemens

Philip L. Varghese

Gary A. Hallock

Roger D. Bengtson

Simulation Studies of Direct-Current Microdischarges for Electric Propulsion

by

Thomas Dominique Deconinck, Ir.

Dissertation

Presented to the Faculty of the Graduate School of

The University of Texas at Austin

in Partial Fulfillment

of the Requirements

for the Degree of

Doctor of Philosophy

The University of Texas at Austin

December 2008

To my family

Acknowledgments

My sincere thanks to Prof. Laxminarayan Raja for his constant encouragement and guidance during the course of my graduate studies. I am grateful to the Air Force Office of Scientific Research for funding this work (contract FA9550-06-1-0176). I thank my family for their patience and support in all my efforts. I also thank my past and current colleagues, Prashanth Kothnur, Jichul Shin, Guangye Chen, Shankar Mahadevan, Utsav K.C., Marshall Albright, Hariswaran Sitaraman, and Doug Breden for their help and input.

Thomas Dominique Deconinck

The University of Texas at Austin
December 2008

Simulation Studies of Direct-Current Microdischarges for Electric Propulsion

Publication No. ____________________

Thomas Dominique Deconinck, Ph.D.
The University of Texas at Austin, 2008

Supervisor: Laxminarayan L. Raja

The structure of direct-current microdischarges is investigated using a detailed two-dimensional multi-species continuum model. Microdischarges are direct-current discharges that operate at a relatively high pressure of about 100 Torr and geometric dimensions in the 10-100 micrometer range. Our motivation for the study of microdischarges comes from a potential application of these devices in microthrusters for small satellite propulsion. The Micro Plasma Thruster (MPT) concept consists of a direct-current microdischarge in a geometry comprising a constant area flow section followed by a diverging exit nozzle. A detailed description of the plasma dynamics inside the MPT including power deposition, ionization, coupling of the plasma phenomena with high-speed flow, and propulsion system performance is reported in this study.

A two-dimensional model is developed as part of this study. The model consists of a plasma module coupled to a flow module and is solved on a hybrid unstructured mesh framework. The plasma module provides a self-consistent, multi-species, multi-temperature description of the microdischarge phenomena while the flow module provides a description of the low Reynolds number compressible flow through the system. The plasma module solves conservation equations for plasma species continuity and electron energy, and Poisson's equation for the self-consistent electric field. The flow module solves mass, bulk gas momentum and energy equations. The coupling of energy from the electrostatic field to the plasma species is modeled by the Joule heating term which appears in the electron and heavy species energy equations. Discretization of the Joule heating term on unstructured meshes requires special attention. We propose a new robust method for the numerical discretization of the Joule heating term on such meshes using a cell-centered, finite volume approach.

A prototypical microhollow cathode discharge (MHCD) is studied to guide and validate the modeling effort for the MPT. Computational results for the impedance characteristics as well as electrodynamic and chemical features of the discharge are reported and compared to experimental results. At low current ($< \sim 0.1$ mA), the plasma activity is localized inside the cylindrical hollow region of the discharge operating in the so-called "abnormal regime". For larger currents, the discharge expands over the outer flat surface of the cathode and operates in the "normal regime". Transient relaxation oscillations are predicted in the plasma properties for intermediate discharge currents ranging from $\sim$0.1 mA to $\sim$0.3 mA; a phenomenon that is reported in experiments.

The MPT, in its present configuration, is found to operate as an electrothermal, rather than as an electrostatic thruster. A significant increase in specific impulse, compared to the cold gas micronozzle, is obtained from the power deposition into the expanding gas. For a discharge voltage of 750 V, a power input of 650 mW, and an argon mass flow rate of 5 sccm, the specific impulse of the device is increased by a factor of $\sim$1.5 to a value of 74 s. The microdischarge remains mostly confined inside the micronozzle and operates in an abnormal regime. Gas heating, primarily due to ion Joule heating, is found to have a strong influence on the overall discharge behavior. The study provides crucial understanding to aid in the design of direct-current microdischarge based thrusters.

Contents

List of Tables

List of Figures

List of Symbols

k	Species index
k_b	Background species index
m_k	Atomic mass of species k
Z_k	Charge number of species k
n_k	Number density of species k
n_e	Number density of electrons
T_e	Electron temperature
T_g	Gas temperature
P	Pressure
Φ	Electrostatic potential
ρ	Bulk gas density
$\vec{V}$	Bulk gas velocity
V_x, V_r	Bulk gas velocity components in the axial and radial directions
D_k	Species diffusivity
I_{sp}	Specific impulse
μ_k	Species mobility
$\dot{G}_k$	Production rate of species k

Γ_k	Number flux of species k
Γ_e	Number flux of electrons
ΔE_j^e	Inelastic energy lost by electron in gas phase reaction j
r_j	Rate of progress of reaction j
I_g	Total number of gas-phase reactions
$\bar{\nu}_{e,k_b}$	Electron momentum transfer collision frequency with background gas
$\bar{\nu}_{i,k_b}$	Ion momentum transfer collision frequency with background gas
C_{p_k}	Constant-pressure specific heat for species k
$h_{k,\text{sens}}$	Sensible enthalpy of species k
η_k	Mixture thermal conductivity of species k
$\bar{\bar{\sigma}}_{k,k_b}$	Hard-sphere momentum transfer collision cross section
ρ_s	Areal surface charge density
ϵ_d	Permittivity of the dielectric surface
α_J	Fraction of ion joule energy thermalized to gas thermal energy
γ_{eff}	Effective secondary electron coefficient
MHCD	Microhollow cathode discharge
MPT	Micro Plasma Thruster

Chapter 1

Introduction

The plasma state is referred to as the fourth state of matter because of its unique properties that distinguish it from solids, liquids, and neutral gases. Free electrically charged particles such as electrons and ions make the plasma electrically conductive so that it interacts with external electromagnetic fields. The plasma also produces its own electromagnetic fields due to space charge effects and charge-carrier currents [1–3]. Plasma is the most prevalent state of matter in the universe. Estimates suggest that up to 99% of matter in the entire visible universe is plasma. In a laboratory, a plasma is typically produced by the coupling of electromagnetic energy into a neutral gas through a discharge [4, 5]. There are many different types of discharges, that employ different physical principles for plasma generation. Such discharge mechanisms include direct-current (DC) glow discharges, arc discharges, capacitively coupled plasma (CCP) discharges, inductively coupled plasma (ICP) discharges, etc. A particular class of DC discharges, called microdischarges, is the focus of this study.

Common laboratory plasmas can be categorized as either "thermal" plasmas or "non-thermal" plasmas. The main constituents (ions, electrons, neutrals) of a thermal plasma are in thermodynamic equilibrium and can be characterized by a single temperature. In a non-thermal plasma, the electron temperature is much higher (~10,000 K to ~100,000 K) than the temperature of the ions and neutrals, which are roughly the same and, in most cases, not much higher than the room temperature.

The DC glow discharge plasma is a weakly ionized non-thermal plasma [6]: the fraction of ionized atoms is 10^{-8} - 10^{-4}. Due to the low ionization degree, recombination is of minor importance, and most of the charged particles are lost by transport to solid surfaces. Glow discharges are used in a large number of application fields, ranging from analytical chemistry [7], to the micro-electronics industry [8], and to generate lasers [9], light sources [10], etc. For voltages above the breakdown threshold, DC discharges are sustained by emission of secondary electrons from the cathode, mostly due to positive ion bombardment. A distinctive feature of DC discharges is a layer of positive space charge in front of the cathode, with strong electric fields and a considerable potential drop. This drop, known as the cathode fall, screens the remainder of the glow discharge from the applied electric field. Glow discharges generally operate at pressures below tens of Torr. At higher pressure, the onset of instabilities prevents stable glow discharge operation. For example, thermal instabilities can switch the discharge mode from glow to a filamentary or arc mode (glow-to-arc transition). Operating the plasma at low pressure has several drawbacks, which include expensive vacuum systems and high maintenance costs of such systems.

Over the last decade, a new class of discharges, called microdischarges, have gained considerable interest in the plasma community [11]. These are special high-pressure ($\sim$100 Torr) glow discharges, stabilized by operating with relatively small characteristic dimensions (10-100 microns). Glow discharges (including microdischarges) obey similarity principles based on Paschen's law. The product of pressure and interelectrode distance (a measure for the number of atoms an electron collides with on its path from the cathode to the anode) is a similarity parameter for glow discharges. The voltage required to ignite a discharge depends on the value of this product and follows the so-called "Paschen curve", as shown schematically in Fig. 1.1. Typical glow discharges operate at 1 - 10 Torr-cm because of the reasonably low breakdown voltage (several 100's of volts) associated with these operating conditions. At atmospheric pressure and electrode separation of a few centimeters (which are typical operating conditions for low-pressure plasmas), breakdown voltages on the order of 10 kV are required to ignite the discharge. The high breakdown voltage leads to a high current density after the discharge is ignited. The high current density is the source of discharge instabilities in the cathode fall region, which quickly lead to the formation of an arc. As a consequence of Paschen's law, the breakdown voltage can be kept low if the electrode separation is reduced when the pressure is increased.

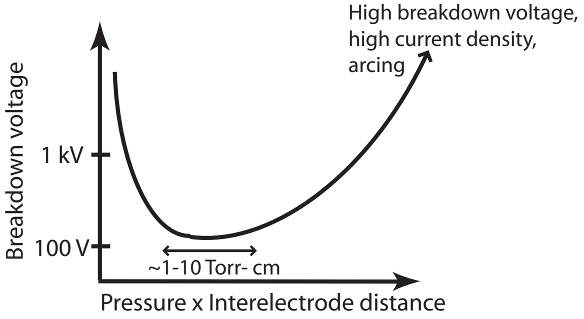

Figure 1.1: Schematic diagram of a typical Paschen curve, i.e. a plot of the breakdown voltage vs. the product of pressure and electrode separation

Microdischarges have several unique properties compared to their large-scale counterparts. Increased collisionality at high pressure causes a large fraction of the input power to be dissipated into gas heating. The gas heat is in turn lost efficiently to the discharge surfaces due to the large surface-to-volume ratio of these devices, resulting in a high degree of thermal non-equilibrium, despite the high-pressures. The thermal non-equilibrium is accompanied by chemical non-equilibrium effects. At the higher pressures, three-body collisions such as atomic ion conversion to molecular ions and three-body quenching of excited states become important, resulting in a significantly different thermo-chemical environment compared to both low-pressure classical glow discharges and high-pressure arcs. These properties of microdischarges open up possibilities for new applications. Indeed, novel uses of microdischarges have been proposed in photonics [12], environmental applications [13], and chemical analysis [14].

A new microthruster concept called the Micro Plasma Thruster (MPT) was recently proposed [15]. The MPT consists of a direct-current microdischarge in a geometry comprising a constant area flow section followed by a diverging exit nozzle. Geometric dimensions are typically on the order of hundreds of microns. In the MPT concept, a stable microdischarge is generated at low propellant flow rates (few sccm). The propellant gas in the microdischarge is eventually expelled from the diverging nozzle. The MPT design is shown in Fig. 1.2. The MPT requires no external magnetic fields or external electron emission sources to stabilize the discharge. Thrust is produced by the expanding gas flow, which is preheated by the microdischarge. Additional thrust may be provided by fast ions that are expelled by the MPT down an electrostatic potential gradient into the vacuum.

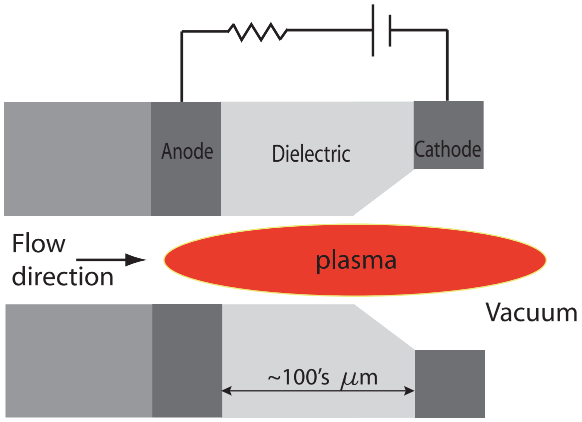

Figure 1.2: Schematic of the proposed microdischarge-based thruster concept

A successful design of the proposed microthruster requires a detailed understanding of microdischarge phenomena as well as plasma-flow interactions. Experimental investigations of the microdischarge are hindered by the extremely small geometries, where well-established plasma diagnostic techniques are inadequate. Computational modeling can therefore have a big impact in developing a fundamental understanding of the proposed microthruster.

In Chapter 2, a brief literature review on microdischarges and plasma modeling is presented. The motivation and objectives of the present work are discussed in Chapter 3.

A preliminary study on microthrusters is reported on Chapter 4. In this chapter, simulations of micronozzle flows are conducted with a commercially available Navier-Stokes solver.

Chapter 5 describes the model used for this study. The model comprises an integrated plasma module and a flow module. A fluid (continuum) approach has been chosen for simulating the plasma. The numerical model is based on a cell-centered, finite-volume discretization of the gas discharge governing equations on unstructured meshes. A semi-implicit technique has been implemented for the time differencing of the governing equations. Part of Chapter 5 is devoted to a discussion of a new approach to the discretization of the Joule heating term appearing in the energy equations.

There is a growing body of experimental data on a specific type of microdischarge, namely the microhollow cathode discharge (MHCD). For example, detailed information regarding the voltage-current characterisitcs of these devices and estimates of electron and gas temperatures are available [16]. These data provide quantitative and qualitative results to guide and validate the computational modeling efforts. Results and discussion on MHCD phenomena and, in particular, on more transition behavior are presented in Chapter 6.

Plasma-flow interactions in the MPT are studied in Chapter 7. A detailed description of the plasma dynamics including power deposition, ionization, coupling of the plasma phenomena with high-speed flow, and propulsion system performance is reported.

Finally, conclusions are presented in Chapter 8, and validation of the plasma model with available analytical solutions is reported in Appendix A.

1.1 Contributions

The following contributions have been made in this study by the author:

- Development of a stable coupling strategy between the plasma and flow module.
- Inclusion of a gas energy equation in plasma module to capture the gas heating in microdischarges.
- Inclusion of ion momentum equation in plasma module to evaluate accurately the ion fluxes in the MPT.
- Development of an effective discretization scheme for the Joule heating source term on unstructured meshes.
- Computational model has been used to understand mode transition behavior in argon microhollow cathode discharges.
- Computational model has been used to study plasma-flow interactions inside the MPT. In its present configuration, the MPT is found to operate as an electrothermal, rather than as an electrostatic thruster. The effects of several parameters on the propulsion performance of the MPT have been studied numerically.

Chapter 2

Literature review

A review of experimental and computational studies in the literature relevant to this work is presented. We focus on microdischarges for the experimental part of this review. Literature on computational modeling of glow discharges in general (including microdischarges) will be reviewed since similar models are used for both microdischarges and macroscopic glow discharges.

2.1 Experimental studies

An important part of the research on microdischarges is driven by the flat panel display industry. The basic principles of the plasma display panel (PDP) were first demonstrated at the University of Illinois at Urbana-Champaign in the 1960's by Bitzer and Slottow [17]. A PDP consists of two glass plates, which hold an inert mixture of noble gases (neon and xenon). An array of tiny cells (with dimensions $\sim$100 μm) located between these panels support microdischarges, which excite a phosphor layer to emit visible light of different colors. There is extensive literature on the principles of PDPs, including several review articles [18–20].

A number of new configurations and devices have been developed for specific applications in the past decade [21]. We have selected a few relevant experimental studies on microdischarges that are discussed below.

Experimental studies of various microplasmas have been carried out using a variety of established techniques ranging from electrical characterization to various optical diagnostic methods and mass spectrometry. Because of the small spatial extent of microplasmas, the vast majority of these studies yield results averaged over the volume of the microdischarge. Recently, Wang *et al* [22] used optical emission spectroscopy with a 6 μm spatial resolution to determine the gas temperature profile across a 200 μm wide atmospheric pressure helium microplasma. Gas temperatures between 350 and 550 K were reported, with the peak value near the cathode.

Microdischarges can be operated using non-DC discharge modes, for example using pulsed excitation, radio-frequency (RF) or microwave excitation. The pulsed mode helps reduce the thermal loading on the electrodes at high currents. Pulsed excitation with microsecond pulses [23,24] and, in particular, with nanosecond pulses [25] causes significant changes in the plasma parameters and a noticeable increase in the ultraviolet emission intensity through excimer species produced in the plasma. Significant shifts in both the temperatures and energy distribution functions of ions and electrons are observed, which cause an increase in the ionization and excitation rate coefficients. This allows for the selective production of chemically reactive species. RF and microwave excitation of microplasmas have been demonstrated in several laboratories [26, 27] and have been explored as a means of generating stable plasmas in air at atmospheric pressure.

Many applications of microdischarges require the arrangement of these discharges in arrays. For example, it can be motivated by the prospect of increased excimer emittance. von Allmen *et al* [28] designed and tested multilayer ceramic structures in which each microdischarge was individually ballasted. Large arrays of microplasma devices have also been fabricated on silicon-based structures. A distinct advantage of silicon is the expertise that has been developed by the microelectronics community over the past several decades and that can now be used for realizing microdischarge devices having cavities with precisely-controlled cross-sections. Park *et al* [29] report the construction of silicon microplasma devices with square trench cathode cavities having cross-sections of (10 μm)^2 or (30 μm)^2 and a depth of 200 μm. The uniformity of emission over the entire array is one prominent characteristic of the Si device structures. Ostrom and Eden [30] also found that Si devices can be used as photodetectors in the visible and near-infrared.

The microhollow cathode discharge (MHCD) refers to a canonical microdischarge generated in a metal-dielectric-metal sandwich structure into which a through or blind hole is drilled. The thickness of the sandwich layers and the hole diameter is $\sim$10 to $\sim$100 micrometers. Early experimental studies on the MHCD were performed by Schoenbach *et al* [31] who reported a rich variety of stable operating regimes that range from a Townsend-like regime at low currents/powers, a glow regime at intermediate currents, to constricted arcing at higher currents/powers. Based on imaging studies and voltage-current characteristics of the MHCD, distinct structural features of the discharge operation have been described by several authors [16, 32, 33]. At low currents ($< \sim$0.1 mA), the discharge is confined to the hollow region with the discharge voltage exhibiting a steep increase with increasing current. This impedance characteristic essentially resembles an abnormal glow discharge, since the plasma remains confined to the hole and a current increase can only be sustained by increasing carrier density (electrical conductivity) through an increase in the MHCD voltage. For intermediate currents ($\sim$0.1 mA $<$ I $< \sim$1 mA), a region of negative resistivity is observed. Early studies attributed this to the onset of the classical hollow cathode effect [34], and hence the name microhollow cathode discharge. However, for typical operating conditions of the MHCD (PD $=\sim$ 1 Torr-cm, where D is the hole diameter), the hollow cathode effect is not necessarily active since the electron energy-loss mean free path is too short to allow electrons emitted from one part of the hollow cathode sheath to reach the opposite cathode sheath with enough energy to cause ionizing reactions. Boeuf *et al* [35] showed that the negative resistivity impedance characteristic in a MHCD was associated with the transition from the hole confined abnormal discharge to a normal glow discharge caused by spreading of discharge activity outside the hole along the outer flat cathode surface. In other words, despite the hollow area of the MHCD cathode and the outer flat area of the MHCD cathode being contiguous, the large outer flat surface area is not accessible as an active cathode until a threshold voltage is reached. Other MHCD discharge phenomena such as self-pulsing modes have been observed experimentally by Hsu and Graves [32] and by Aubert *et al* [16]. Hsu and Graves [32] assume that the self-pulsing mode is due to an instability resulting from the interaction between a negative differential resistivity in the current-voltage characteristics of the MHCD and the load line of the external circuit. They propose a qualitative equivalent circuit model to capture the essential physics of the self-pulsing mode. While this model produces self-pulsing features, it is unable to predict the observed shapes of the current waveforms correctly. Aubert *et al* [16] discuss the self-pulsing mode observed in the medium current range ($\sim$0.1 to $\sim$1mA), between the hole confined abnormal regime and the normal glow regime where the plasma expands to the outer flat cathode surface. They report that the self-pulsing frequency is a linear function of the time-averaged discharge current and decreases with the device capacitance. The self-pulsing is related to a fast expansion of the plasma outside the discharge hole over the outer cathode surface. They propose a simplified equivalent circuit model, using a bistable voltage-controlled variable resistor that gives predictions of the temporal evolution of the electrical parameters in reasonable agreement with the experiments. We must note that similar self-pulsing regimes have also been observed for macroscopic glow discharges. For example, Petrović *et al* [36] report self-sustained oscillations between parallel-plane electrodes (1 cm spacing) for which the self-pulsing mode occurs in the negative resistivity region of the glow discharge.

Microdischarges have been recently investigated for use as microthrusters. Horisawa and Kimura [37] investigated the feasibility of plasma-jet microthrusters using both gaseous (nitrogen) and solid propellants (Teflon). They generated millinewtons of thrust at nitrogen flow rates of about 100 sccm and found that increasing anode-cathode separation improved the thrust efficiency (incremental thrust per unit power). Slough *et al* [38] studied direct-current microdischarges in micronozzle flows with upstream pressure of ∼10 Torr consuming 1-5 W. They measured a specific impulse of up to 220 s at argon flow rates of 30 sccm resulting in a total thrust of 2.2 mN.

2.2 Computational studies

Numerous computational studies of low-pressure glow discharges have been performed since the 1960's. Most of the recent modeling has been concerned with glow discharges in two-dimensional geometry [39, 40]. Review papers containing detailed comparisons between models have been written by Lister [41] and Phelps [42].

The Boltzmann equation provides the foundation for most of the numerical models. The Boltzmann equation describes the particle conservation in seven-dimensional space $(\vec{x}, \vec{v}, t)$ for each species in the discharge. An important aspect of glow discharge modeling is the use of adequate data regarding cross-sections as input to solve the Boltzmann equations. Excitation and ionization of atoms by electrons is the major inelastic process in maintaining low-pressure glow discharges in noble gases (He, Ar, Ne). Radiation between atomic states is a further inelastic process to be included for lighting applications but also for interpretation of spectroscopic diagnostics. In general, collisions with neutral particles dominate all other elastic processes. Electron-electron collisions can be regarded as negligible for degrees of ionization below 10^{-5}, which is generally the case for glow discharges.

Fluid models describe the transport of electrons, ions and possibly other reactive species by the first few moments of the Boltzmann equation. These models provide spatial and temporal information on averaged properties such as species density and species temperature in discharges. The local field approximation (LFA) is an approximation made within the fluid model framework. In LFA models, ionized species are assumed to be in a steady-state motion at the local electric field (i.e. the local electron energy distribution function depends only on the local value of the electric field). The validity of this assumption becomes questionable in regions where the electric field varies significantly over length scales of the order of the electron mean free path. In LFA models, transport coefficients and rate coefficients are treated as functions of the reduced electric field (ratio of the local electric field to the gas density). Reasonable accuracy has been achieved when using such models in terms of predicting the global electrical characteristics of low-pressure glow discharges [43]. The LFA model can be improved by including an energy equation (the third moment of the Boltzmann equation) for the electrons [44]. Such models treat the electron coefficients (transport and rate coefficients) as functions of the local mean electron energy.

Non-local field models take into account the fact that the mean free paths of charged particles may be comparable to the thickness of the cathode-fall. Such models correctly describe how energy gained from the electric field at one position is dissipated in collisions with the gas or an electrode at another position. The terminology "hybrid model" is used to designate models that treat one part of the problem with non-local techniques. Fiala *et al* [45] developed a two-dimensional, hybrid model of low-pressure glow discharges where the source term for volume ionization is determined through a Monte Carlo simulation of the cathode-emitted electrons and their progeny. It was found that the spatial distribution of ionization events cannot be predicted accurately by traditional LFA fluid models. Nevertheless, the LFA models gave a reasonable prediction of the V-I characteristics of the discharge. The global discharge behavior was correctly predicted with the LFA model because the total number of ionization events (integrated across the cathode fall) agreed well with the prediction from the Monte Carlo simulations.

Microdischarge simulations for display technology have been performed by several research groups [46–49]. Rauf and Kushner [47] used a detailed two-dimensional hybrid code to investigate the operation of a coplanar-electrode PDP cell in He/Ne/Xe gas mixtures. In their model, a Monte Carlo simulation for secondary electrons and a radiation transport model for visible light emission is coupled to the fluid equations (including the electron energy equation). Hagelaar and Kroesen [48] investigated the validity of LFA models for microdischarges in plasma addressed liquid crystal displays. For this purpose they developed a Monte Carlo model for electrons, which they compared to a fluid model. Although the electron energy distribution function calculated with the Monte Carlo model displays several non-equilibrium phenomena, both models lead to virtually the same electron density profile.

Recent computational studies have played an important role in elucidating the structure and the physical and chemical mechanisms occurring in MHCD discharges [35, 50–52]. Kushner [50] presents simulation results of an argon MHCD and describes the sensitivity of the MHCD to variations in the secondary electron emission coefficient by ions and photon impact at surfaces. Kushner [50] also describes the importance of gas heating occurring in MHCD discharges. For example, the formation of eximer species was found to be particularly sensitive to gas heating and rarefaction due to their dependence on three-body reaction processes. Kothnur and Raja [52] investigate a helium MHCD for different operating pressures and discharge currents. For sufficiently large currents ($> \sim$1mA), a significant part of the discharge volume is found to lie outside the hollow structure with the plasma occupying a region of a few hollow diameters above the flat cathode surface plane; a result that is in agreement with available experimental results. They also report high gas temperatures (several hundreds of Kelvin above room temperature), which is again confirmed by experiments [53].

Kothnur and Raja [54] studied direct-current microdischarges in a flowing gas stream for applications in electro-thermal microthrusters. For currents around 1 mA, the microdischarge is found to operate in an abnormal glow mode with positive differential resistivity. An increase in input electrical power results in an almost linear increase in the gas temperatures; this property of microdischarges is a key feature that can be exploited in the microdischarge-based thruster concept. Arakoni *et al* [55] studied a nominal microdischarge configuration with a flowing gas that resembles a thruster, although the flow modeling approach used in this study does not consider compressibility effects. Gas temperatures exceeding 1000 K are reported for power densities of tens of kilowatts per cubic centimetre at upstream pressure of tens of Torr. They found that the nozzle length and the location of the discharge in the nozzle have an important influence on the incremental thrust (above that of the cold flow).

Chapter 3

Motivation and objectives

Our motivation for the study of microdischarges comes from a potential application of these devices in microthrusters. There is currently a great interest in the miniaturization of spacecraft in the 1 - 100 kg class that are capable of meeting certain mission objectives. The development of an appropriate propulsion device is a major engineering challenge for such satellites. Small satellite propulsion devices are faced with stringent requirements concerning propellant usage and power utilization. Also importantly, these devices must be simple in design and occupy a very small volumetric footprint. The thruster should be highly controllable which is almost impossible with conventional combustion-based propulsion systems, because of issues related to ignitability of propellant at such small length scales and lack of adequate control over combustion processes. Given the likely presence of onboard electrical power generation, there would be significant benefit from using electric propulsion for improving the efficiency of propellant use as well as an increase in exhaust velocity. The extremely small dimensions of microdischarges combined with intense and controllable gas heating can be exploited for such space propulsion systems.

The main goal of this research is to obtain a self-consistent model, which is suitable for the simulation of our proposed microdischarge-based thruster, the Micro Plasma Thruster (MPT), and which can be used as a tool for optimizing the microdischarge operating conditions. In this model, a plasma solver is coupled to a high-speed flow solver. The plasma model provides a self-consistent, multi-species, multi-temperature description of the microdischarge phenomena while the gas dynamics model provides a description of the low Reynolds number compressible flow through the system. Modeling issues specific to this type of problem are highlighted and numerical techniques that have been developed to address those issues are reported. For example, traditional low-pressure glow discharge models do not account for gas heating and make assumptions regarding the species flux (the drift-dufusion approximation) that may not be valid for our problem. Stiffness of the governing equations also poses challenges to the numerical scheme.

Another goal of this work is to understand the plasma-flow interactions inside the MPT. In particular, we would like to understand how the microdischarge affects the micronozzle flow and determine whether the electrostatic component of thrust significantly contributes to the total thrust of the device. A detailed description of the plasma dynamics including predictions of power deposition, ionization, and propulsion system performance will be reported.

Chapter 4

Preliminary studies on microthrusters

4.1 Introduction

Microsatellites (mass less than 100 kg) have recently gained interest for various industry, military, and science space missions [54–61]. Several advantages, including a reduced launch cost, are associated with these devices. Mission costs can also be reduced by off-loading scientific instruments from a large, single spacecraft onto a fleet of microsatellites. In this configuration, the loss of a single microsatellite may not jeopardize the entire mission. Also, microsatellites can be launched "piggyback", using excess capacity on larger launch vehicles.

Present microsatellites are extremely power-limited, typically delivering less than a watt per kilogram of spacecraft mass [56]. Scaling traditional propulsion systems down in power and size to suit the needs of microsatellites is a major engineering challenge. Micropropulsion requirements can significantly vary given the diversity of microsatellite missions conceivable but are generally characterized by their very low thrust values (millinewtons and below) and low impulse bits for attitude control (tens of micronewton-seconds and below). High delta-v microsatellite missions require propulsion technologies with high specific impulses (I_{sp}), as can be seen from the Tsiolkovsky rocket equation [62],

$$\Delta v = I_{sp}\, g_0 \ln\frac{m_0}{m_1}, \tag{4.1}$$

where g_0 is the standard gravity, m_0 is the initial total mass, including propellant, and m_1 is the final total mass.

4.2 Overview of existing technologies for micropropulsion

Bipropellant engines are frequently considered for primary propulsion applications on conventional satellites, in particular for high delta-v maneuvers because of their relatively high specific impulse (~300 s). Disadvantages of these devices compared to other propulsion systems are their relative complexity and their large number of component parts. Scaling down these devices in size presents numerous challenges, including combustion efficiency losses due to the reduced mixing and vaporization. For these reasons, bipropellant systems are not well suited onboard a microsatellite. Hydrazine monopropellant thrusters have an engine technology substantially simpler that than that of bipropellant engines, at the expense of performance characteristics (specific impulses around 200 s). Miniaturized versions of hydrazine thrusters can be used on microsatellites as primary propulsion systems for low delta-v maneuvers. Millinewton hydrazine thrusters with impulse bit performances of ~100 μN-s are also being developed to serve needs of precise positioning control of satellites flying in constellation formations [63].

Ion engines and Hall thrusters are characterized by their large specific impulse (~1000 to ~3000 s). However, the propellant mass reduction associated with their high specific impulse has to be traded off against electric power requirements. Miniaturization of these devices to suitable size and power consumption for microsatellite presents several issues. For example, increased quenching of ionized species at the channel walls makes these devices less efficient at smaller length scales. For Hall thrusters, larger magnetic fields have to be provided to reduce electron gyration radii given the smaller channel dimensions.

FEEP (Field Emission Electric Propulsion) thrusters can be scaled down to deliver very low impulse bits ($\sim 10^{-8}$ N-s) and very low thrust values ($\sim 10^{-6}$ N) with a high specific impulse (∼5000 s) [64]. However, heavy power conditioning units are needed to deliver the high required voltages (∼10 kV). Also the low thrust-to-power values of these devices make them impractical for microsatellite applications. For the same level of thrust, the power requirements for colloid thrusters are lower than those of FEEP devices. Thrust levels in the millinewton range and specific impulses of about 1000 s can be achieved using a couple of watts of power with an array of colloid thrusters [56]. However, the voltage requirements for these thrusters are still very high (∼10 kV).

Cold gas thrusters are low-performance systems limited by their low values of specific impulse (∼50 s). Advantages of these devices compared to other propulsion systems include their low system complexity, their small impulse bit, their low-cost, and the fact that, when using benign propellants (e.g. N_2), they present no satellite contamination problem. Cold gas thrusters are well suited for attitude control applications of microsatellites when only limited spacecraft lifetimes are required, reducing leakage concern. They can also be used as primary propulsion system if the delta-v requirements are less than ∼100 m/s. Since nozzle throat diameters in the micrometer range are required for micropropulsion applications, the production of these microthrusters rely on MEMS-based technologies.

The extremely small dimensions of microdischarges combined with intense and controllable gas heating can be exploited in microthrusters. Like conventional cold gas thrusters, electrothermal microdischarge propulsion systems have extremely low mass and volume footprints. They are electrically simple, and, unlike other electric propulsion technologies, they do not require auxiliary systems such as neutralizers, heaters, or magnets. They have a unique capability in that thrust is available at different power levels, including zero power. We will show that a significant improvement in the specific impulse compared to conventional cold gas thrusters can be achieved with these systems. This would, in turn, increase the range of applicability of cold gas thrusters to missions with higher delta-v requirements.

4.3 Micronozzle flows

4.3.1 Scaling issues

Electrothermal microdischarge propulsion systems require the expansion of propellant gases through micronozzles. If we consider the entire expansion from the pressurized tank to outer space, the flow passes through all regimes, namely from continuum to free molecular flow (far from the exit of the nozzle). As discussed by Ketsdever in [56], nozzle operating conditions and physical dimensions must be scaled to obtain the reduced thrust levels and size requirements needed for microsatellites. In the limit of continuum isentropic flow through a large pressure drop, the nozzle's thrust is proportional to the total pressure and the throat area,

$$F \propto P_0 A_t \propto P_0 d_t^2. \tag{4.2}$$

The Reynolds number gives a measure of nozzle efficiency in terms of viscous flow losses. The Reynolds number at the nozzle throat is given by

$$Re = \rho\, a\, d_t/\mu \propto P_0 d_t / T_0^x, \tag{4.3}$$

where ρ, a, and μ are the density, the speed of sound, and the viscosity, respectively, evaluated at the nozzle throat and x is an exponent with value between 1 and 1.5, depending on the gas [56]. For the viscous losses to scale favorably, the Reynolds number, which is proportional to $P_0 d_t$ must remain constant or increase as the device is scaled down. For a constant stagnation pressure and temperature, the thrust in a micronozzle can be reduced by a factor of 100 by reducing the throat diameter by a factor of 10, which reduces the throat Reynolds number by only a factor of

10. Reducing the thrust level by a factor of 100 by reducing the stagnation pressure alone reduces the throat Reynolds number by a factor of 100, resulting in higher viscous losses.

To maintain a constant level of viscous losses (constant Re), a reduction in thrust by a factor of 100 requires a reduction in throat diameter by a factor of 100 and an increase in stagnation pressure by the same factor. Since pressure increases of this order are not realistic for microsatellites, the operational Reynolds number for micronozzles may in fact decrease to values as low as 100. Moreover, when heat is added into the micronozzle flow, Eq. 4.3 indicates that the flow will be at an increasingly low Reynolds number.

4.3.2 Model description and validation

Figure 4.1 shows the micronozzle configuration and computational domain considered for this study. The geometrical configuration of the thruster matches the one that will be used in Chapter 7 for more detailed studies of the Micro Plasma Thruster (MPT). The geometry consists of an axisymmetric constant area "pipe" section of 500 μm length, followed by a diverging section that is 200 μm in length, which is terminated by a 150 μm long constant area section. The radius of the upstream constant area pipe section is 50 μm, and the exit section is 150 μm in radius. For the base case, the inlet total pressure is 100 Torr, and a small but non-zero outlet pressure is required to stabilize the numerical scheme in the "vacuum" domain. The temperature is fixed at 300 K at the inlet, the outlet, and the solid walls. The selection of this geometry and of these operating conditions was driven by the experimental studies on the MPT performed with a similar micronozzle configuration [15].

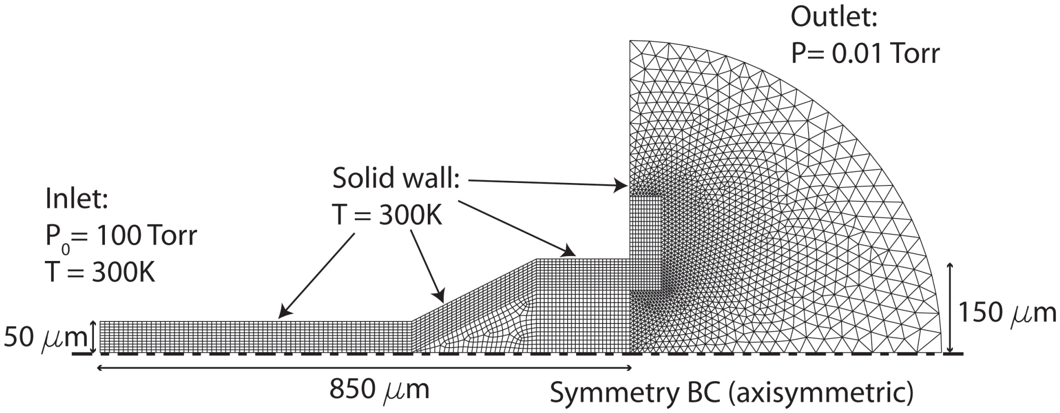

Figure 4.1: Micronozzle configuration and computational mesh. The geometry is cylindrically symmetric.

An argon gas is considered for this study. A calorically perfect gas with specific gas constant $R = 208.1$ J/(kg-K) and $\gamma = 1.67$ is assumed. The viscosity μ is calculated with Sutherland's law,

$$\frac{\mu}{\mu_0} = \left(\frac{T}{T_0}\right)^{\frac{3}{2}} \frac{T_0 + C}{T + C}, \tag{4.4}$$

where $C = 144$ K, $T_0 = 271$ K, and $\mu_0 = 2.125 \times 10^{-5}$ Pa-s. A constant Prandtl number, $Pr = 0.667$, is assumed to evaluate the thermal conductivity of argon. All the above approximations are accurate for values of the temperature varying from 200 K to 2000 K [65].

In the remainder of this chapter, we discuss the feasibility of improving the thruster performances through heat addition in the supersonic diverging portion of the nozzle. A commercially available Navier-Stokes solver (Fluent) is used for the simulation of micronozzle flows while the coupled plasma-flow simulations discussed in Chapter 7 use in-house codes developed in our research group. For the simulations presented here, the equations of conservation (mass, momentum, and energy) are solved implicitly with a density-based method and the fluxes are discretized using a second-order upwind scheme.

By applying the conservation of momentum to a control volume encompassing the entire satellite, the thrust of the device can be evaluated as

$$F = \int_0^R (\rho V_x^2 + P)(2\pi r)dr, \tag{4.5}$$

where V_x is the axial velocity and the integration is carried out over the exit plane of the nozzle. The value of the thrust will be used to monitor the accuracy of the results obtained with different models. For the base case, a no-slip boundary condition is imposed at the solid wall, which yields a value for the total thrust of 67.4 μN. For these conditions, the averaged Reynolds number at the throat (the intersection of the upstream constant area pipe section and the diverging section) is ~150. The Knudsen number varies from ~0.01 at the inlet to ~0.08 at the exit plane of the nozzle. For these values of Knudsen number, the no-slip boundary condition can break down [65]. Tests were performed where either a no-slip or slip-flow boundary condition was used. For the latter, the gas speed at and parallel to the wall, V_w, is given by

$$V_w = \lambda \frac{2 - \sigma_m}{\sigma_m} \frac{\partial V_w}{\partial y}, \tag{4.6}$$

where λ is the mean free path, σ_m is the transverse momentum accommodation coefficient (~1), and $\frac{\partial V_w}{\partial y}$ is the gradient of the parallel (to the wall) velocity component in the perpendicular direction. In the worst case, we found differences in our thrust calculations of 2-3% when comparing no slip and slip-flow boundary conditions. Case studies also showed that the wall-temperature jump boundary condition has very little effect on the final performance of the nozzle. These findings are confirmed by previous studies on micronozzle flows [55]. Other studies also show that, for similar micronozzle geometries, results obtained with direct simulation Monte Carlo methods (DSMC) and fluid models are in good agreement with each other, and that the modeling data can reasonably match available experimental data [59, 66].

The Knudsen number becomes quite large in the exterior region of the nozzle and the continuum description of the flow clearly becomes invalid. We included this region to test the sensitivity of the computed thrust to the extrapolation boundary condition used at the outlet. The exit conditions consist of two regions, the supersonic core flow, and the subsonic boundary layer. While the supersonic core flow is extrapolated from the interior to the exit conditions, the subsonic boundary layer should be affected by the exit pressure since the governing equations become elliptic. By varying the value of the pressure at the outlet, we showed that this effect was negligible as long as the outlet pressure was less than ~0.5 Torr. We also performed simulations with a larger exterior section which confirmed the independence of the thrust value to the outlet boundary conditions. Simulations performed without the exterior section (with the boundary of the computational domain being the exit plane of the nozzle) yielded thrust values that are about 5% accurate.

4.3.3 Results

The flow properties are shown for the base case in Fig 4.2. Grid refinement studies showed that the grid is sufficiently fine, and that the results are independent of the mesh. The inlet flow rate is 0.14 mg s^{-1} (5.2 sccm) which corresponds approximately to a mean inlet flow velocity of 80 m/s. As shown in Fig 4.2.a, the pressure in the upstream constant area section of the nozzle drops nearly linearly from ~100 Torr at the inlet to ~30 Torr as the diverging section is approached. Owing to gas-dynamic expansion, the pressure drops rapidly in the diverging section to ~5 Torr near the exit plane. As shown in Fig 4.2.c, the bulk flow axial velocities at the centerline increases in the constant area section to reach a value of about 350 m/s at the end of this section. In the diverging section, the expansion accelerates the flow to a centerline velocity of about 450 m/s, which corresponds to a Mach number of ~3 (as shown in Fig 4.2.e).

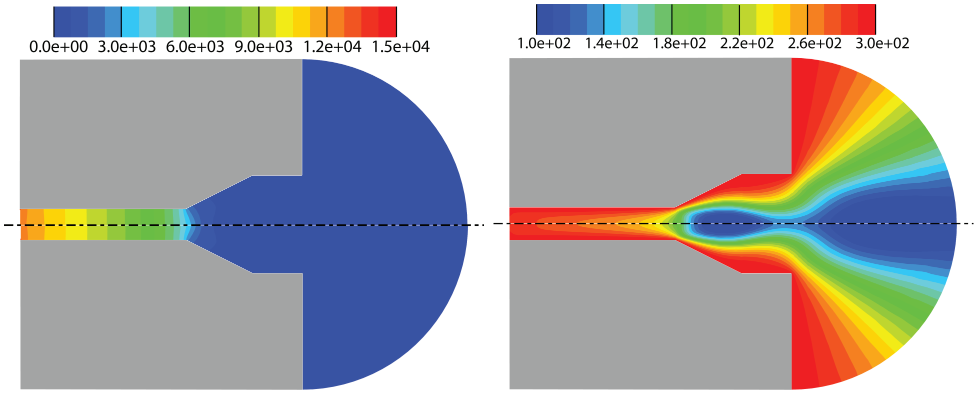

(a) Pressure (Pa) (b) Temperature (K)

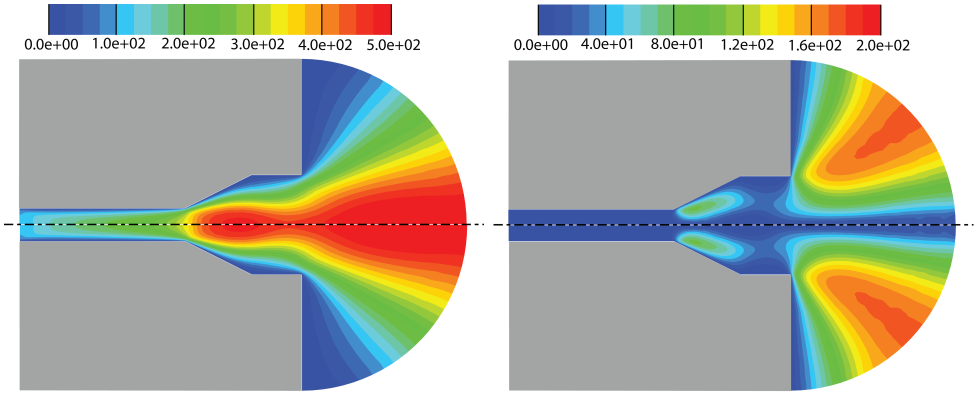

(c) Axial velocity (m/s) (d) Radial velocity (m/s)

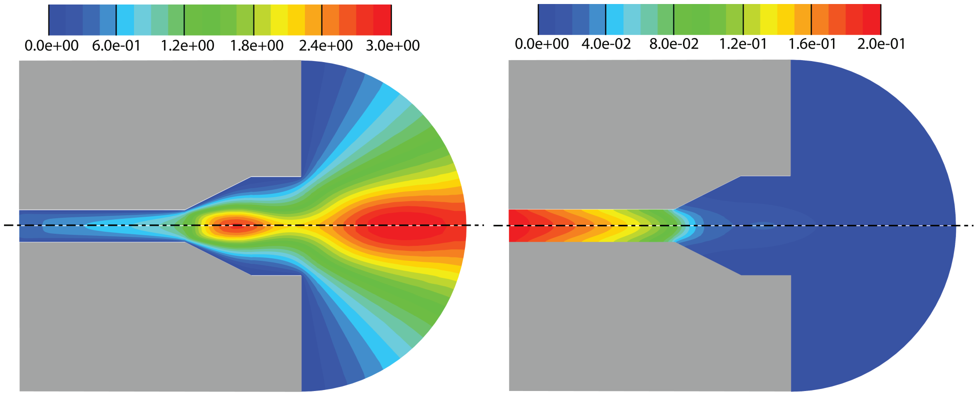

(e) Mach number (f) Density (kg/m^3)

Figure 4.2: Flow properties in the micronozzle. The inlet total pressure and temperature are fixed at 13300 Pa (100 Torr) and 300K, respectively. At the solid walls, no-slip boundary conditions are applied and the temperature is fixed at 300 K. The Reynolds number at the throat is ∼150.

The viscous nature of the flowfield is apparent from the large subsonic boundary layer, and the inviscid core is restricted to a small portion of the flow near the centerline. Therefore, viscous losses are expected to be quite significant. The inefficiencies arise from the adverse interaction of the subsonic boundary layer with the core of the supersonic flow causing the flow not to expand fully in the diverging nozzle section. For comparison, the ideal quasi-one dimensional isentropic expansion gives an exit Mach number of about 5 for a similar ratio between the throat area and the exit plane area ($\frac{A}{A^*} = 9$).

Assuming an isentropic expansion of a 300 K argon gas to zero pressure, a theoretical specific impulse (I_{sp}) of 57 s can be achieved. For our base case, the computed specific impulse (the thrust divided by the mass flow rate) is 49.8 s. Additional simulations were performed at higher back pressure and higher stagnation temperature. The stagnation temperature was varied by modifying the imposed temperature at all the boundaries. Table 4.1 summarizes the computed specific impulses obtained for the different operating conditions. Since the viscous flow losses decrease with increasing Reynolds number, the efficiency of the device improves with increasing stagnation pressure (as shown in Eq. 4.3). Although the overall performance of high-temperature systems through the micronozzle is better than cold gas systems, the efficiency of the thruster (the ratio between the computed and theoretical specific impulse) is reduced since viscous losses increase with temperature (as shown in Eq. 4.3).

Operating conditions	Computed I_{sp}	Theoretical I_{sp}
T = 300 K, P_0 = 100 Torr	49.8 s	57 s
T = 300 K, P_0 = 200 Torr	50.5 s	57 s
T = 300 K, P_0 = 400 Torr	51.6 s	57 s
T = 600 K, P_0 = 100 Torr	69.4 s	82 s
T = 600 K, P_0 = 200 Torr	70.1 s	82 s
T = 600 K, P_0 = 400 Torr	70.5 s	82 s

Table 4.1: Micronozzle specific impulse for various stagnation pressures and temperature with an argon propellant. The temperature, T, refers to the imposed temperature at all boundaries.

The effects of an external heat source on micronozzle flows is now investigated. The heat source is placed in the diverging section of the micronozzle and is considered to be uniformly distributed across a fictitious cylinder (as shown in Fig 4.3). The location and geometrical extent of the heating is a priori expected to be similar to those of the electrothermal heating from the microdischarge. One goal of the simulations is to determine the amount of power needed to significantly increase the thrust of the propulsion device. The consequences of a 100 mW heat deposition on flow properties are shown in Fig 4.3. Except for the additional volumetric heat source, the operating conditions are the same as those of the base case. As shown in Fig 4.3.b, the heating causes a significant increase in gas temperature whose peak now reaches a value of $\sim$1600 K. The axial velocity (shown in Fig 4.3.d) also increases at the exit plane compared to the base case, which indicates an increase in the thrust of the device. The new value of the thrust for this case is 105.4 μN. The flow in the upstream section of the nozzle appears not the be influenced by the addition of the heat source and the mass flow rate is the same as for the base case (0.14 mg s^{-1}). A large fraction ($\sim$60%) of the power deposited in the micronozzle is lost at solid walls. Therefore, the isothermal wall assumption is actually a very conservative assumption. In reality, the outer walls of the thruster are heated since they are not perfect conductors. As shown earlier, increasing the wall temperature results in an increased thrust.

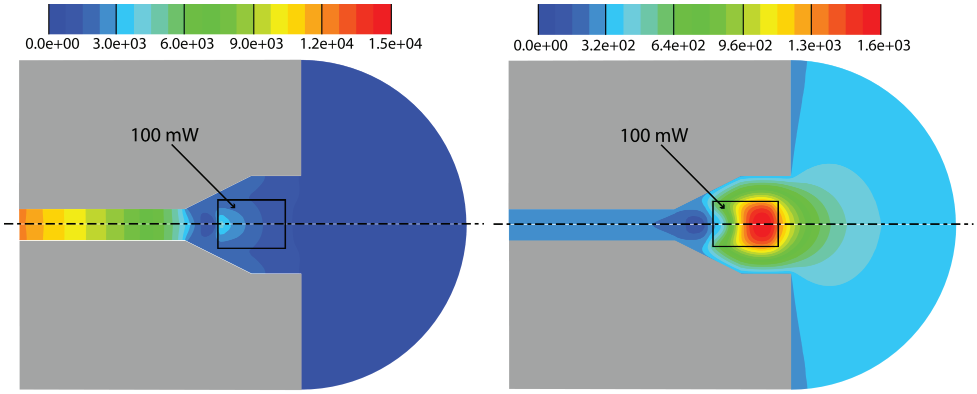

(a) Pressure (Pa) (b) Temperature (K)

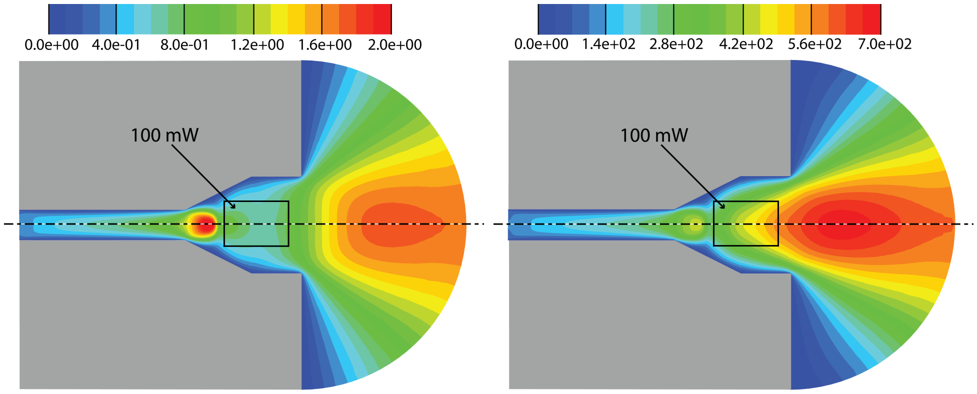

(c) Mach number (d) Axial velocity (m/s)

Figure 4.3: Flow properties in the micronozzle with 100 mW heat addition. The inlet total pressure and temperature are fixed at 13300 Pa (100 Torr) and 300K, respectively. At the solid walls, no-slip boundary conditions are applied and the temperature is fixed at 300 K. The Reynolds number at the throat is ∼150.

Figure 4.4 shows the specific impulse of the device as function of the power deposited into the flow. For a power deposition of 0.15 W, the maximum temperature in the micronozzle reaches about 2000 K, which constitutes the upper bound of the validity range for our model assumptions (see Section 4.3.2). The specific impulse increases more rapidly at low power and appears to saturate at higher powers. The saturation with power is due to an increase in heat losses to walls (due to a larger ΔT), and an increase in viscous losses. The amount of power that can be added to the flow before reaching saturation obviously scales with the mass flow rate (which depends on the inlet pressure).

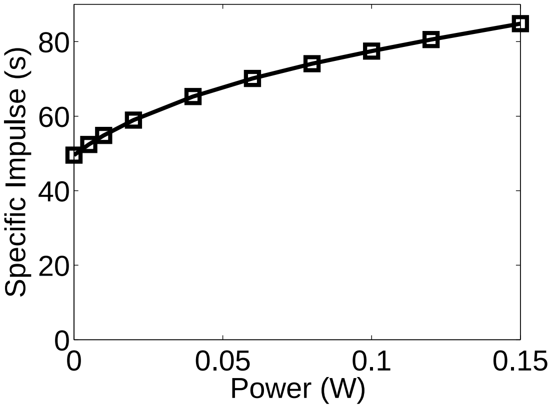

Figure 4.4: Specific impulse of the microthruster as function of power deposited in the diverging section of the micronozzle

4.4 Summary

Existing thruster technologies were reviewed for potential micropropulsion applications. Scaling down these devices in power and size constitutes a unique engineering challenge and only a few of the currently existing thruster technologies appear to be suitable for microsatellites. Cold gas thrusters are characterized by their low system complexity, and their low specific impulse. Recent advances in MEMS technologies are permitting the development of cold gas thrusters with nozzle throat diameters in the micrometer range. The inherent small Reynolds number of micronozzle flows make them prone to significant viscous losses, which further reduces the specific impulse of these devices.

Simulations of micronozzle flows were performed with a commercially available Navier-Stokes solver (Fluent). We showed that, for our operating conditions, a fluid model combined with no-slip boundary condition was appropriate to simulate micronozzle flows. For an inlet pressure of 100 Torr and an argon mass flow rate of 5.2 sccm, a thrust of 67.4 μN was obtained for our micronozzle geometry. This corresponds to a specific impulse of 49.8 s (which is ∼15% less than the maximum theoretical value one can achieve with argon for these conditions). Higher specific impulses are achieved by heating the flow in the diverging section of the micronozzle. For our operating conditions, a heat addition of ∼0.1 W is needed to increase the thrust (and the specific impulse) by a factor of ∼1.5. The specific impulse saturates at higher power due to an increase in heat losses to walls and an increase in viscous losses. In our MPT concept, this heat addition would be caused by electrothermal heating from the microdischarge. Such electrothermal thrusters can be used in power-limited situations for microsatellite attitude control or nanosatellite (10 kg or less) primary propulsion system with low delta-v requirements.

Chapter 5

Methodology

In order to study coupled plasma and flow phenomena in high-pressure microdischarges, a model comprising an integrated plasma module and flow module has been developed. In the Micro Plasma Thruster, the plasma and flow phenomena are strongly coupled: the plasma causes gas heating, which modifies the gas density, and hence the flow field; the bulk flow velocities, in turn, affect the distributions of number densities and temperatures of plasma species in the discharge.

5.1 Plasma Module

5.1.1 Model assumptions

The plasma module incorporates a number of simplifying assumptions:

1. A full continuum fluid approach is currently used to model the microdischarge phenomena. This is a reasonable model assumption at high pressures (10 - 1000 Torr) and for characteristic dimensions of ~100 μm or more. Under these conditions, the mean free paths of the heavy species are typically smaller than gradient length scales of discharge properties. For example, at $P = 25$ Torr and $T = 300$ K, the mean free path for ion-neutral and electron-neutral collisions in argon is ~1 μm. In the cathode-fall region of microdischarges, because

of the large electric fields, it becomes questionable to model the electrons emitted from the cathode with a fluid model. Nevertheless, past studies [45,48] have shown that the fluid model was able to correctly predict global discharge properties (including the electron number density profile) for microdischarges.

2. In our fluid model, all the transport properties are computed based on interactions with a dominant background species. Therefore, electron-electron collisions are not being considered, which is a valid assumption for weakly ionized plasmas. For microdischarges, the degree of ionization tends to become significant ($\sim 10^{-4}$). This is due to the similarity rules [2]: If the linear dimension of a discharge is divided by n and the pressure is multiplied by n, then the space-charge density is multiplied by n^2 so that the degree of ionization is multiplied by n. For our studies, the values of electron transport properties were not significantly affected when electron-electron collisions were considered.

3. Although a high degree of thermal nonequilibrium exists in microdischarges, a common heavy species temperature is assumed for ions and neutrals. For a 10 Torr argon plasma, the energy transfer mean free path is ~ 10 μm for argon ions colliding with argon neutrals, implying that ion Joule energy is rapidly (i.e. locally) redistributed among all heavy species, justifying the use of a common heavy species temperature. The electron temperature is treated separately.

4. The role of radiation from excited states in the overall energy balance is neglected. This is a reasonable assumption because of the relatively low contribution of radiation to the overall energy budget in microdischarges and glow discharges in general. For example, the efficiency of excimer emission observed from MHCD-based photonics devices is found experimentally to be about 2% [67].

5. Secondary electron emission due to field emission is neglected. Field emission

starts to contribute to the total emission of electrons from the cathode when the electric field becomes on the order of 10^9 V/m or larger [68]. In the cases studied here, the smaller value of the electric field at the cathode ($\sim 10^7$ V/m) allows us to neglect field emission processes.

5.1.2 Governing equations

Species continuity

The densities of individual species in the discharge are determined by the species continuity equation,

$$\frac{\partial n_k}{\partial t} + \vec{\nabla} \cdot \left(n_k \vec{V} \right) + \vec{\nabla} \cdot \vec{\Gamma}_k = \dot{G}_k, \qquad k = 1, \ldots, K_g \quad (k \neq k_b) \tag{5.1}$$

where n_k is the number density of species k, $\vec{V}$ is the bulk flow velocity, $\vec{\Gamma}_k$ is the flux density of species k, $\dot{G}_k$ is the gas-phase species generation rate through plasma chemical reactions, and K_g is the total number of gas species. The dominant neutral species is identified as the "background" species, and designated as k_b; its density being determined to satisfy the ideal gas law,

$$P = n_{k_b} k_B T_g + n_e k_B T_e + \sum_{k \neq k_e, k \neq k_b} n_k k_B T_g \tag{5.2}$$

where P is the local pressure, k_B is Boltzmann's constant, subscripts e and g denote electrons and the background gas respectively. If there is no bulk gas flow, the pressure is fixed at a specified constant value; otherwise it is computed as part of the flow solution.

Electron energy

The electron temperature, T_e, is explicitly computed in order to determine the reaction rates due to electron impact and the electron transport properties. The following electron energy equation is solved,

$$\begin{aligned}\frac{\partial}{\partial t}\left(\frac{3}{2}k_B n_e T_e\right) + \vec{\nabla}\cdot\left(\frac{5}{2}k_B T_e n_e \vec{V}\right) + \vec{\nabla}\cdot\left(\frac{5}{2}k_B T_e \vec{\Gamma}_e\right) - \vec{\nabla}\cdot(\eta_e \nabla T_e) \\ = e(\vec{\Gamma}_e + n_e\vec{V})\cdot\vec{\nabla}\Phi - \frac{3}{2}k_B n_e \frac{2m_e}{m_{k_b}}(T_e - T_g)\bar{\nu}_{e,k_b} - e\sum_{j=1}^{I_g}\Delta E_j^e r_j,\end{aligned} \tag{5.3}$$

where η_e is the thermal conductivity of electrons, m_e and m_{k_b} are the molecular mass of electron and dominant background gas species respectively, $\bar{\nu}_{e,k_b}$ is the electron momentum transfer collision frequency with the background gas, ΔE_j^e is the energy lost per electron (in eV) in an inelastic collision event represented by a gas-phase reaction j, r_j is the rate of progress of a reaction j (in units of #/m^3-s), and I_g is the total number of gas-phase reactions. In Eq. 5.3, the first term signifies time rate of change of electron thermal energy per unit volume, the second term is the transport of electron energy by the bulk flow, the third and fourth terms account for electron thermal energy flux due to species diffusion and thermal conduction, the first term on the right-hand side (RHS) signifies Joule heating, the second term on the RHS accounts for electron energy lost due to elastic collisions with the background gas, and the last term quantifies the energy lost from the electron swarm due to inelastic electron-impact reactions. Section 5.2 describes a new formulation for the discretization of the Joule heating term on unstructured meshes.

Gas energy equation

In case the flow solver is not used, the gas temperature is computed within the plasma module. The following gas energy equation is then solved,

$$\begin{aligned}\frac{\partial}{\partial t}\sum_h n_k h_{k,\mathrm{sens}} + \vec{\nabla}\cdot\sum_h \vec{\Gamma}_k h_{k,\mathrm{sens}} - \vec{\nabla}\cdot\left(\sum_h \eta_k \vec{\nabla} T_g\right) \\ = -\alpha_J\left(e\sum_h Z_k\vec{\Gamma}_k\cdot\vec{\nabla}\Phi\right) + \frac{3}{2}k_B n_e \frac{2m_e}{m_{k_b}}(T_e - T_g)\bar{\nu}_{e,k_b} - e\sum_{j=1}^{I_g}\Delta E_j^g r_j,\end{aligned} \tag{5.4}$$

where $h_{k,sens}$ is the sensible enthalpy of species k, η_k is the thermal conductivity of species k, the subscript h indicates that the summation is to be carried out over all the heavy species, and ΔE_j^g is the bond or ionization energy in an inelastic collision event represented by the gas-phase reaction j.

The first term in Eq. 5.4 is the time-dependent storage term. The second term signifies transport of heavy species energy due to species diffusion. The third term represents energy transport due to thermal conduction. The first term on the RHS represents the effective ion Joule heating, taken here to be a fraction α_J ($0 < \alpha_J < 1$) of the local Joule heating ($\vec{J}_{ion} \cdot \vec{E}$, where $\vec{J}_{ion}$ is the total ion current density and $\vec{E}$ is the local electric field). This fraction is less than one for cases where the ion mean free path is a non-negligible fraction of the plasma characteristic length scale, which results in incomplete conversion of the local kinetic energy gained by the ions in the electric field to the ion/heavy species thermal energy. For microdischarge conditions, we use a fixed value of $\alpha_J = 0.25$, as suggested in [35]. The second term on the RHS accounts for volumetric gas heating due to elastic collisions between electrons and background species. This term has the same magnitude as the first term on the RHS in the electron energy equation (Eq. 5.3). Finally the last term in Eq. 5.4 accounts for the energy transferred to/from the internal chemical energy of the species.

The sensible enthalpy is evaluated as

$$h_{k,\text{sens}} = \int_0^{T_g} C_{p_k} dT \approx C_{p_k} T_g \tag{5.5}$$

where the species constant-pressure specific heat equals $\frac{5}{2}k_B$ for monatomic species and $\frac{7}{2}k_B$ for diatomic species. Using Eq. 5.2 (where the pressure is prescribed) and the above equation for the sensible enthalpy, one can readily show that the enthalpy density $\sum_h n_k h_{k,\text{sens}}$ is constant for a weakly ionized gas. Equation 5.4 then reduces to the following heat conduction equation,

$$-\vec{\nabla}\cdot\left(\sum_h \eta_k \vec{\nabla} T_g\right) = -\alpha_J\left(e\sum_h Z_k \vec{\Gamma}_k \cdot \vec{\nabla}\Phi\right) + \frac{3}{2} k_B n_e \frac{2m_e}{m_{k_b}}(T_e - T_g)\bar{\nu}_{e,k_b} - e\sum_{j=1}^{I_g} \Delta E_j^g r_j. \tag{5.6}$$

Heat conduction through the solid walls and the increase in wall surface temperatures due to plasma phenomena are not considered in this study.

Electric potential

The self-consistent electric potential is determined using the electrostatic Poisson's equation,

$$\nabla^2\Phi + \frac{\mathrm{e}}{\epsilon_0}\sum_{k=1}^{K_g} Z_k n_k = 0, \tag{5.7}$$

where Φ is the potential, e is the unit electric charge, ϵ_0 is the permittivity of free space, and Z_k is the charge number of species k (e.g., -1 for electrons).

Ion momentum

The ion number flux densities are evaluated as $\vec{\Gamma}_i = n_i\vec{u}_i$, where $\vec{u}_i$ is the ion fluid velocity, which is determined using the first moment of the ion species Boltzmann equation, i.e., the ion species momentum equation,

$$\frac{\partial n_i\vec{u}_i}{\partial t} + \vec{\nabla}\cdot(n_i\vec{u}_i\vec{u}_i) = -\frac{en_i}{m_i}\vec{\nabla}\Phi - \frac{k_B T_i}{m_i}\vec{\nabla} n_i - n_i(\vec{u}_i - \vec{V})\bar{\nu}_{i,k_b}. \tag{5.8}$$

The first two terms on the LHS model the unsteady and inertial effects. The first and second terms on the RHS model electric field drift and density gradient diffusive contributions, respectively; and the last term accounts for the effect of interspecies friction drag.

5.1.3 Transport formulation

A simplified form of the species momentum equation is obtained by ignoring the inertia terms (the drift-diffusion approximation). This is a reasonable assumption despite the large electric fields in high-pressure microdischarges owing to the high-collisionality of the plasma. For the MPT simulations, since the pressure drops considerably towards the exit of the nozzle, the full ion momentum equation is solved. Using the drift-diffusion approximation, the species number flux density ($\vec{\Gamma}_k$) is found as

$$\vec{\Gamma}_k \;=\; -\mu_k n_k \vec{\nabla}\Phi - D_k \vec{\nabla} n_k, \qquad (k \neq k_b), \tag{5.9}$$

where μ_k is the species mobility (which is set to 0 for neutral species), and D_k is the species diffusion coefficient.

The operating gas considered for this study is argon. An independent solution of the zero-dimensional electron Boltzmann equation ("BOLSIG+" [69]) provides electron transport properties in an argon background tabulated as a function of the electron temperature. The ion mobilities are derived from experimental mobility data [70] and are approximated by the following expressions

$$\mu\, n_{k_b} = \frac{4 \times 10^{21}}{\{1 + (2.21 \times 10^{29} E/n_{k_b})^{1.5}\}^{0.33}} \qquad \text{for } Ar^{+}, \tag{5.10}$$

$$\mu\, n_{k_b} = \frac{7 \times 10^{21}}{\{1 + (2.21 \times 10^{29} E/n_{k_b})^{1.5}\}^{0.33}} \qquad \text{for } Ar^{2+}. \tag{5.11}$$

The ion diffusion coefficients are computed using the Einstein relation,

$$D_k = \frac{\mu_k k_B T_g}{e Z_k}, \tag{5.12}$$

The transport properties of metastable species are given by,

$$D_k \;=\; \frac{k_B T_k}{m_k \bar{\nu}_{k,k_b}}, \tag{5.13}$$

$$\mu_k \;=\; \frac{e Z_k D_k}{k_B T_k}. \tag{5.14}$$

The collision frequency between metastable species k and the background species k_b

is evaluated as

$$\bar{\nu}_{k,k_b} = n_{k_b}\bar{\bar{\sigma}}_{k,k_b}\bar{g}_k, \tag{5.15}$$

where $\bar{\bar{\sigma}}_{k,k_b}$ is an approximate hard-sphere momentum transfer collision cross section for the species k colliding with the background species k_b, and $\bar{g}_k$ is the average relative molecular speed of species k, given by

$$g_k = \sqrt{\frac{8k_BT_k}{\pi m_{k,r}}}, \tag{5.16}$$

where $m_{k,r} = \frac{m_k \times m_{k_b}}{m_k + m_{k_b}}$ is the reduced mass of species k. Constant cross sections based on the Lennard-Jones interaction potentials [71] are used in Eq. 5.15 for metastable species.

Finally, the thermal diffusivity that appears in the gas energy equation (Eq. 5.4) is evaluated as

$$\eta_k \quad = \quad \frac{5}{2}n_k k_B D_k. \tag{5.17}$$

5.1.4 Boundary conditions

Species number densities

For the electrons, kinetic Maxwellian flux conditions are imposed at solid walls (electrodes or dielectric surfaces), along with the secondary electron emission from the walls

$$\vec{\Gamma}_e \cdot \hat{n} = \frac{1}{4}n_e\left(\frac{8k_BT_e}{\pi m_e}\right)^{1/2} - \gamma_{eff}\vec{\Gamma}_{ion} \cdot \hat{n}, \tag{5.18}$$

where $\hat{n}$ is the unit vector normal pointed toward the wall. The first term in Eq. 5.18 is the Maxwellian flux of electrons to the surface and the second term is the secondary electron emission flux from the surface. Secondary electron emission coefficients are known to be very sensitive to surface properties and the history of gas/plasma exposure to the surface. An effective secondary emission coefficient (γ_{eff}) formulation described by Phelps and coworkers [70, 72] is used to model this process. The model relates the total secondary electron emission flux from the surface to the net ion flux impacting the surface $\vec{\Gamma}_{ion} \cdot \hat{n}$. The total secondary electron emission includes contributions from ion impact, fast atoms, metastable atoms, and ultraviolet photons.

The mobility limited flux condition is imposed for all ions at solid surfaces, given by

$$\vec{\Gamma}_i \cdot \hat{n} = \max(-\mu_i n_i \vec{\nabla}\Phi \cdot \hat{n}, 0), \tag{5.19}$$

and the Maxwellian flux condition is imposed for the neutral species, given by

$$\vec{\Gamma}_n \cdot \hat{n} = \frac{1}{4} n_n \left(\frac{8 k_B T_g}{\pi m_n} \right)^{1/2}. \tag{5.20}$$

Electron and gas temperature

For the electron energy equation, the following energy flux is imposed at solid walls

$$Q_e^W = \frac{5}{2} k_B T_e \Gamma_e^W, \tag{5.21}$$

where Γ_e^W is the electron wall number flux. The gas temperature is fixed at 300 K at solid walls.

Dielectric surfaces

The potential on dielectric surfaces is determined using the the total surface charge accumulated on the surface. The equation for evolution of the net surface charge density, ρ_s (units: C/m^2), is given by,

$$\frac{\partial \rho_s}{\partial t} = \sum_{k=1}^{K_g} e Z_k \vec{\Gamma}_k \cdot \hat{n}. \tag{5.22}$$

Gauss's law is used to approximate the potential on thin dielectric surfaces as,

$$\Phi_b = \frac{\Phi_c + \frac{\Delta x_n}{\epsilon_o}\left(\rho_s + \frac{\epsilon_d}{d}\Phi_s\right)}{1 + \frac{\epsilon_d \Delta x}{d\epsilon_o}}, \tag{5.23}$$

where Φ_c is the potential at a distance Δx_n normal to the dielectric surface in the plasma, ϵ_d represents the permittivity of the dielectric, d is the thickness of the dielectric, and Φ_s represents the potential on the backside of the dielectric (held grounded in our simulations). In this model, the potential Φ_c is evaluated at the first cell center located in a direction normal to the boundary.

Ion momentum

For all solid boundaries for which the electric field points away from the wall ($\vec{E} \cdot \hat{n} < 0$), the flux of positive ions is set to 0. If the electric field points towards the wall ($\vec{E} \cdot \hat{n} > 0$), the ion flux is extrapolated from the interior by imposing a zero gradient of the ion flux at the boundary.

5.1.5 Plasma chemistry

A pure argon plasma gas chemistry is used and comprises six species: electrons (e), atomic argon ions (Ar^+), molecular argon ions (Ar_2^+), electronically excited atoms (Ar^*), electronically excited molecules (Ar_2^*), and the background argon atoms (Ar). Dimer species are included because of the relatively high operating pressures (∼100 Torr). The list of reactions considered in the study is given in Table 5.1 and comprises electron impact ionization and excitation reactions, Penning ionization reactions, three-body reactions for dimer excited species and ion formation, quenching and deexcitation reactions. Electron impact reaction rates are determined a priori by solving the zero-dimensional electron Boltzmann equation (BOLSIG+ [69]) with appropriate electron energy-dependent reaction cross sections for a range of reduced electric fields (E/n_{k_b}). The electron impact reaction rate coefficients and the electron mean energies are determined as a function of E/n_{k_b} by the Boltzmann solver. These results are then used to tabulate the rate coefficients as a function of the electron mean energy (temperature) for use in the plasma discharge simulations. The following expressions approximate the tabulated rates for reactions G_2 to G_5,

$$\begin{aligned}
G_2 &: \exp(-\frac{4.31\times10^{29}}{T_e^6}+\frac{2.96\times10^{25}}{T_e^5}-\frac{7.91\times10^{20}}{T_e^4}+\frac{9.92\times10^{15}}{T_e^3}\\
&\qquad -\frac{6.45\times10^{10}}{T_e^2}+\frac{4.75\times10^{4}}{T_e}-30.8),\\
G_3 &: \exp(-\frac{2.15\times10^{30}}{T_e^6}+\frac{1.34\times10^{26}}{T_e^5}-\frac{3.23\times10^{21}}{T_e^4}+\frac{3.66\times10^{16}}{T_e^3}\\
&\qquad -\frac{1.97\times10^{11}}{T_e^2}+\frac{1.67\times10^{5}}{T_e}-29.8),\\
G_4 &: \exp(-\frac{5.51\times10^{28}}{T_e^6}+\frac{5.08\times10^{24}}{T_e^5}-\frac{1.85\times10^{20}}{T_e^4}+\frac{3.38\times10^{15}}{T_e^3}\\
&\qquad -\frac{3.34\times10^{10}}{T_e^2}+\frac{1.39\times10^{5}}{T_e}-29.7),\\
G_5 &: \exp(-\frac{4.82\times10^{4}}{T_e}-32.46),
\end{aligned}$$

where the electron temperature, T_e is in Kelvin and reaction rates have units of cm^3 s^{-1}.

At the surfaces all excited species and charged species are assumed to get quenched with unity sticking coefficient. Upon quenching at surfaces, each dimer ion and excited species is assumed to return to plasma a pair of ground state neutral *Ar* atoms, while the monomer species return as a single *Ar* atom.

5.2 Discretization of the Joule heating term on unstructured meshes

The Joule heating source term, i.e. the first term on the RHS of Eqs. 5.3 and 5.4, constitutes the main source term in the electron energy balance and often

#	Reactions	Reaction rate^a	Ref.
G_1	$e + Ar \Rightarrow e + Ar$	b	[69]
G_2	$e + Ar \Rightarrow e + Ar^*$	b	[69]
G_3	$e + Ar \Rightarrow 2e + Ar^+$	b	[69]
G_4	$e + Ar^* \Rightarrow 2e + Ar^+$	b	[69]
G_5	$e + Ar^* \Rightarrow e + Ar$	b	[69]
G_6	$e + Ar^+ \Rightarrow Ar^*$	$4.0 \times 10^{-13} T_e^{-0.5}$	[73]
G_7	$2e + Ar^+ \Rightarrow Ar^* + \mathrm{e}$	$5.0 \times 10^{-27} T_e^{-4.7}$ cm^6 s^{-1}	[73]
G_8	$e + Ar_2^+ \Rightarrow Ar^* + Ar$	$5.38 \times 10^{-8} T_e^{-0.66}$	[73]
G_9	$2Ar^* \Rightarrow Ar^+ + Ar + e$	5.0×10^{-10}	[73]
G_{10}	$2Ar_2^* \Rightarrow Ar_2^+ + 2Ar + e$	5.0×10^{-10}	[73]
G_{11}	$Ar^* + 2Ar \Rightarrow Ar_2^* + Ar$	1.14×10^{-32} cm^6 s^{-1}	[73]
G_{12}	$Ar^+ + 2Ar \Rightarrow Ar_2^+ + Ar$	2.5×10^{-31} cm^6 s^{-1}	[73]
G_{13}	$Ar_2^* \Rightarrow 2Ar$	6.0×10^{-7} s^{-1}	[73]
G_{14}	$e + Ar_2^* \Rightarrow 2e + Ar_2^+$	$9.0 \times 10^{-8} T_e^{0.7} \exp(-3.66/T_e)$	[73]
G_{15}	$e + Ar_2^* \Rightarrow e + 2Ar + e$	10^{-7}	[73]

[a] Rate coefficients have units of cm^3 s^{-1}, unless mentioned otherwise. The electron temperature, T_e, is in Kelvin

[b] Tabulated rate coefficient as a function of mean electron temperature was obtained by the Boltzmann equation solver "BOLSIG+" [69].

Table 5.1: High-pressure argon plasma gas-phase chemistry used in this model

times in the gas energy equation. Since reaction rates due to electron impact are exponential functions of the electron temperature, small deviations in the electron energy density can result in significant changes in the predicted discharge characteristics. Most reaction rates also depend on the number density of the background gas, and therefore on the gas temperature. The accuracy of the method used to compute the Joule heating term in the energy balance equations is therefore critical. As shown in [74], the stability of the numerical scheme depends on the technique used to compute the source term of the electron energy equation owing to temporal stiffness introduced by this term for several types of plasma discharge problems.

Complex two-dimensional or three-dimensional geometries are now commonly encountered in the modeling of plasma discharges. Local mesh refinement is often needed to capture the steep gradients in the number density and in the electric field profiles. For these reasons, the use of unstructured meshes is necessary, as is already the case for computational fluid dynamics. Robust and accurate numerical methods to simulate gas discharges on unstructured meshes must therefore be developed.

Several issues specific to the simulations of plasma phenomena arise in the context of unstructured meshes; the treatment of the Joule heating term being one. Here we discuss a simple and accurate approach for the numerical treatment of this term in the context of a cell-centered, finite-volume discretization of the plasma discharge governing equations on generalized unstructured meshes. The technique can be used on structured meshes as well, where it reduces to a simplified numerical stencil.

5.2.1 Numerical method

The governing equations (Eqs. 5.1, 5.3, 5.4, 5.7, 5.8) can be cast in an integral form, by integrating them over an arbitrary control volume V as

$$\int_V \frac{\partial \alpha}{\partial t} dV + \int_{\partial V} \vec{\Gamma}_\alpha \cdot d\vec{S} = \int_V S_\alpha dV, \tag{5.24}$$

where α is the dependent variable (e.g. the species number density, n_k), $\vec{\Gamma}_\alpha$ are the fluxes, and S_α are the source terms. In the cell-centered finite volume scheme for a fixed non-moving mesh, the following spatial discretization is used to approximate Eq. 5.24

$$V_{cell} \frac{\partial \alpha_{cc}}{\partial t} + \sum_f \Gamma_{\alpha,fc} A_f = V_{cell} S_{\alpha,cc} \tag{5.25}$$

where V_{cell} is the cell volume, the subscript cc and fc indicate the cell-centered value and the face-centered value of the corresponding variable, respectively, the index f indicates the summation over all the faces enclosing the cell, and A_f is the area of face f. For the gas discharge governing equations, the fluxes $\Gamma_{\alpha,fc}$ are the normal projections of the species fluxes, the electric field, and the electron and gas energy fluxes at the face centers and are assumed positive directed out of the cell. Figures 5.1 and 5.2, for example, show the locations at which the normal projections of the fluxes are evaluated for a structured and unstructured mesh, respectively.

Several discretization schemes of the fluxes at the face centers [75] are considered in this study. The consistency and accuracy of the following three methods

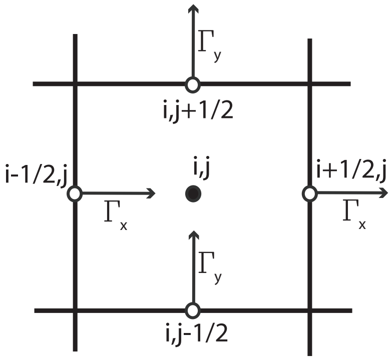

Figure 5.1: Orthogonal two-dimensional structured mesh. Scalar solution variables are evaluated at the cell center (point with solid circle). The x- and y-components of the fluxes are evaluated at the face centers (points with open circles).

will be tested:

- Central-difference flux

$$\Gamma_{\alpha,fc} = V_{fc}(\frac{\alpha_{cc,1} + \alpha_{cc,2}}{2}) - D_{fc}(\frac{\alpha_{cc,1} - \alpha_{cc,2}}{\delta}) \tag{5.26}$$

- Upwinded flux

$$\begin{aligned} \Gamma_{\alpha,fc} &= V_{fc}\,\alpha_{cc,1} - D_{fc}(\frac{\alpha_{cc,1} - \alpha_{cc,2}}{\delta}) \quad \text{if} \;\; V_{fc} > 0 \\ \Gamma_{\alpha,fc} &= V_{fc}\,\alpha_{cc,2} - D_{fc}(\frac{\alpha_{cc,1} - \alpha_{cc,2}}{\delta}) \quad \text{if} \;\; V_{fc} < 0 \end{aligned} \tag{5.27}$$

- Scharfetter-Gummel flux

$$\begin{aligned} \Gamma_{\alpha,fc} &= V_{fc}\left(\alpha_{cc,1} + \frac{\alpha_{cc,1} - \alpha_{cc,2}}{\exp(Pe) - 1}\right) \quad \text{if} \;\; Pe = \frac{V_{fc}\delta}{D_{fc}} > 0 \\ \Gamma_{\alpha,fc} &= V_{fc}\left(\alpha_{cc,2} + \frac{\alpha_{cc,1} - \alpha_{cc,2}}{\exp(-Pe) - 1}\right) \quad \text{if} \;\; Pe = \frac{V_{fc}\delta}{D_{fc}} < 0 \end{aligned} \tag{5.28}$$

where V_{fc} is the convective velocity at the face center (e.g., $-\mu_e E_{fc}$ for the electron flux), $\alpha_{cc,1}$ and $\alpha_{cc,2}$ are the solution variables at the two neighboring cell centers, and D_{fc} is the diffusion coefficient at the face center. The convective velocity and the flux are assumed positive directed from the first cell towards the second cell.

The cell-centered value of the Joule heating source term can be computed by first evaluating the components of this term at the face centers (where the fluxes are available), and then interpolating the Joule heating source term at the cell center. This technique has been used by several authors on structured meshes [52, 74, 76]. With this approach, the Joule heating is evaluated as follows on a two-dimensional structured mesh (see Fig. 5.1)

$$[\vec{E}\cdot\vec{\Gamma}](i,j) = \frac{1}{2}[E_x(i+1/2,j)\Gamma_x(i+1/2,j) + E_x(i-1/2,j)\Gamma_x(i-1/2,j)] \\ +\frac{1}{2}[E_y(i,j+1/2)\Gamma_y(i,j+1/2) + E_y(i,j-1/2)\Gamma_y(i,j-1/2)]. \quad (5.29)$$

In Eq. 5.29, the subscript k is dropped from the species flux term $\vec{\Gamma}_k$ for convenience. The subscripts x and y refer to the coordinate directions and the symbols i and j, refer to the node locations in a structured mesh (Fig. 5.1). The Joule heating in Eq. 5.29 is computed by adding the average contribution of the dot product in the x and y directions. Note that it is not simply an average of the product $\vec{E}\cdot\vec{\Gamma}$ computed on each face, in which case the factor in the denominator would have been 4 instead of 2. The reason this method can be used on structured meshes is because the face normals lie exactly along the coordinate directions. On an unstructured mesh, the face normal orientation is arbitrary and hence an extension of of this method is not straightforward.

We propose the following approach for computing the Joule heating source term on a general unstructured mesh with closed convex cells. The term is computed directly at the cell centers by evaluating the dot product of the electric field and the species flux at the cell centers. The two vector quantities can be evaluated explicitly at the cell centers ($\vec{E}_{cc}$ and $\vec{\Gamma}_{cc}$, respectively) using solution variables and fluxes already computed at the faces for the Poisson's (Eq. 5.7) and species continuity equations (Eq. 5.1) by the cell-centered finite-volume method. The face fluxes are nominally available at the face centers (fc).

The Green-Gauss or least-squares reconstruction techniques [77] are commonly used to evaluate the gradient of cell-centered solution variables. Because of ease of implementation, we chose to use the Green-Gauss method to obtain the electric field from the potential field. By this method, the gradient is constructed by applying the Green-Gauss theorem to individual cell volumes in the mesh as follows,

$$(\vec{\nabla}\Phi)_{cc} = \frac{1}{V_{cell}} \sum_{f} \Phi_{fc} \vec{A}_f, \tag{5.30}$$

where Φ_{fc} is the value of potential at the face center, $\vec{A}_f$ is the normal area vector of face f (pointing away from the cell), and the summation is over all the faces enclosing the cell. One can interpolate the face-centered value Φ_{fc} from the values of the potential at the two neighboring cells centers using a simple average or a higher-order weighted averaging procedure.

Evaluation of the species flux vector value at the cell center ($\vec{\Gamma}_{cc}$) however poses a special problem since only the normal projection of the species fluxes (Γ_{fc}) are available at the face centers, through the cell-centered finite-volume method. We propose to reconstruct the species flux vector at the cell center from these normal projections of the species fluxes at the faces enclosing the cell. We refer to this approach as the "Reconstruction-Flux" scheme which we depict in Fig. 5.2. To first order, we assume that the flux we are reconstructing ($\vec{\Gamma}$) is piecewise constant within each cell. This implies that the flux field is irrotational within each cell and that there exists a scalar, ψ, such that $\vec{\Gamma} = \vec{\nabla}\psi$. We assign an arbitrary constant value K to ψ at the cell center. At each face enclosing the cell, we define a new point fp, such that the face area normal vector through the point fp is collinear with the cell center cc. If the normal projection of the species flux at fc (Γ_{fc}) is assumed to be constant across the entire face, the normal projection of the species flux at the point fp (Γ_{fp}) is equal to Γ_{fc}. We can now estimate the value of ψ at fp (ψ_{fp}) for each face by performing a line integration along the line joining cc and fp, i.e.

$$\psi_{fp} = K + d_{cp}\Gamma_{fp}, \tag{5.31}$$

where d_{cp} is the distance between cc and fp.

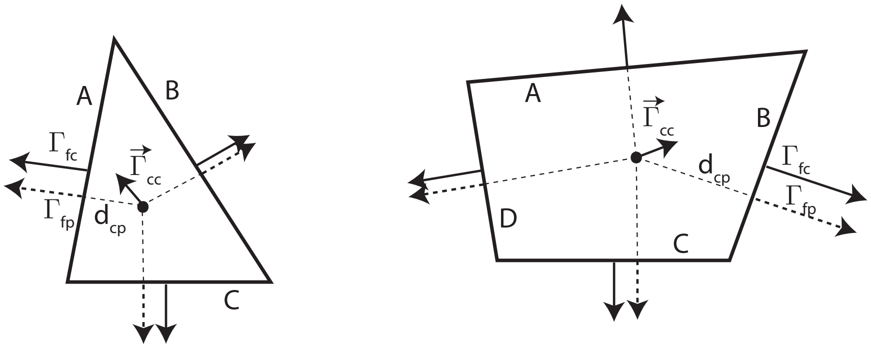

Figure 5.2: Reconstruction of the species flux at the cell center (for a triangular and quadrilateral cell) based on the normal projections of the fluxes at the face centers. The dotted lines intersecting the cell center are perpendiculars to the faces.

Finally, the Green-Gauss theorem is used to compute the "Reconstruction-Flux" at the cell center

$$\vec{\Gamma}_{cc} = \frac{1}{V_{cell}} \sum_f \psi_{fc} \vec{A}_f. \tag{5.32}$$

Here the value of ψ_{fc} is approximated as being equal to ψ_{fp}. Expanding the summation in Eq. 5.32, we obtain

$$\vec{\Gamma}_{cc} = \frac{1}{V_{cell}} \sum_f (K + d_{cp}\Gamma_{fp}) \vec{A}_f = \frac{1}{V_{cell}} \sum_f (d_{cp}\Gamma_{fp}) \vec{A}_f. \tag{5.33}$$

In Eq. 5.33, the term $\sum_f K\vec{A}_f (= K \sum_f \vec{A}_f)$ equals 0 for all closed cells. The above formulation reconstructs the cell-centered value of the species flux vector based on known normal projections of the species fluxes at the faces and other mesh information only.

For an orthogonal structured mesh (as shown in Fig. 5.1), the "Reconstruction-Flux" scheme reduces to

$$[\vec{E} \cdot \vec{\Gamma}](i,j) = \frac{[E_x(i+1/2,j) + E_x(i-1/2,j)]}{2} \frac{[\Gamma_x(i+1/2,j) + \Gamma_x(i-1/2,j)]}{2}$$

$$+\frac{[E_y(i,j+1/2)+E_y(i,j-1/2)]}{2}\frac{[\Gamma_y(i,j+1/2)+\Gamma_y(i,j-1/2)]}{2}. \qquad (5.34)$$

In Eq. 5.34, the electric field and species flux are evaluated at the cell center before performing their dot product, while in Eq. 5.29 the Joule heating is evaluated at the face centers and then interpolated at the cell center.

As an alternative to the above approach, one could also choose to recompute the species flux at the cell center with the same drift-diffusion approximation that is used to compute the flux at the face centers

$$\vec{\Gamma}_k = -\mu_k n_k \vec{\nabla}\Phi - D_k \vec{\nabla} n_k, \qquad (5.35)$$

where μ_k and D_k are the mobility and diffusion coefficients of species k. We will call this method the Recomputed-Flux scheme. The number density (n_k) is already available at the cell center and the electric field and gradient of the species number density can be evaluated by the Green-Gauss method (Eq. 5.30). In most models [48, 50, 52], electron fluxes at the face centers are discretized with the Scharfetter-Gummel exponential scheme to overcome the stiffness in the drift-diffusion form of the electron flux. This approach to evaluating the electron fluxes at the cell center (with reconstruction gradients) is therefore not consistent with the electron fluxes evaluated at the face centers (with the exponential scheme). Consequences of this inconsistency will be discussed in the next section.

5.2.2 Results

Test case

We consider a one-dimensional glow discharge between two infinitely large planar electrodes. The inter-electrode distance is 1 cm and the pressure is 1 Torr. A constant voltage difference of 250 Volts is applied between the two electrodes. A pure argon discharge gas is considered with the argon plasma modeled by three species (ground state atoms Ar, ions Ar^+, and electrons e^-). The species continuity equation is solved for the ions and the electrons, while the background argon number density is held constant. For computational expediency, we assume a simplified chemistry comprising a single ionization reaction due to electron impact ($e + Ar \Rightarrow 2e + Ar^+$). A constant value of the secondary emission coefficient of 0.05 is assumed for the ions impacting at the surface which produce a flux of electrons entering the discharge depending on the ion flux leaving the discharge to wall surfaces. We test our numerical method for computing the Joule heating term in the electron energy equation alone. The gas energy equation is not solved and a constant gas temperature of 300 K is assumed.

Figs. 5.3 and 5.4 show mesh-converged results for which the "Reconstruction-Flux" scheme has been used using a 1000-cell mesh as discussed below. The cathode is placed at $x = 0$ cm and the anode at $x = 1$cm. A peak number density of ionized species of $\sim 10^{16}$ $\#/\mathrm{m}^3$ is observed in the quasi-neutral region of the plasma. The cathode sheath occupies ∼25% of the discharge. A sharply peaked electron production profile (not shown) is located at the sheath edge. The electron temperature is ∼4 eV in the bulk plasma and increases to ∼20 eV in the cathode sheath. The current density for these conditions is ∼0.2 $\mathrm{mA/cm}^2$. Results obtained with different schemes will be compared next. We use the computed value of the current density as a metric for comparing the accuracy between the different numerical methods. The peak number density of the ionized species (Ar^+) has also been used and yield the same results.

One-dimensional mesh

We first discuss results for the above test case using a one-dimensional version of the self-consistent plasma model, where solution variables vary only in the direction perpendicular to the inter-electrode plane. Since a two-dimensional implementation of the above method is used, the numerical solution to this one-dimensional problem is enabled by stacking a layer of single quadrilateral cells in one direction and imposing zero-flux boundary conditions in the other directions. The numerical

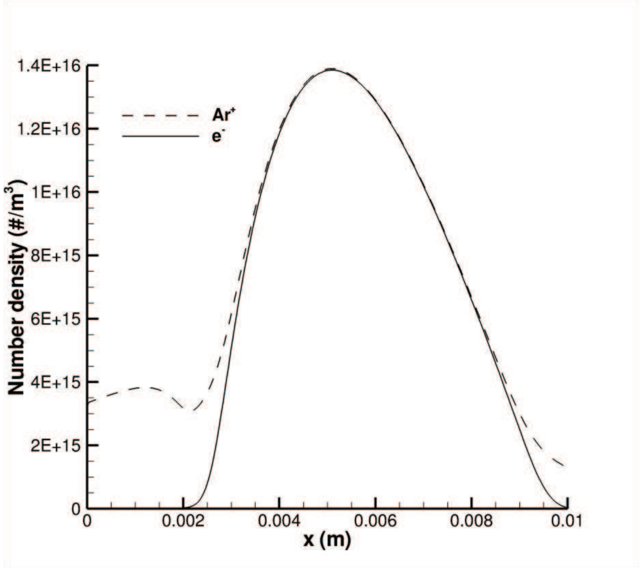

Figure 5.3: Charged species number density profile for a one-dimensional 250-V argon discharge (1 Torr) obtained using a 1000-cell mesh that satisfies mesh-convergence on all of the numerical methods used.

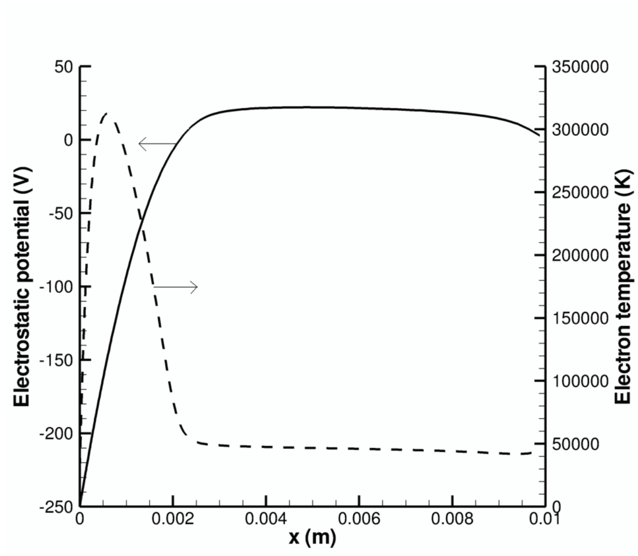

Figure 5.4: Electrostatic potential and electron temperature profiles for a one-dimensional 250-V argon discharge (1 Torr) obtained using a 1000-cell mesh that satisfies mesh-convergence on all of the numerical methods used.

schemes discussed above have been tested on three different meshes: a 60-cell, 250-cell, and 1000-cell mesh. These meshes are stretched to obtain a better resolution of the cathode sheath region. Note that most two-dimensional simulations of gas discharges presented in the literature do not use more than ∼50 mesh points in the electric field direction (interelectrode direction) to capture the cathode sheath of glow discharges. The coarsest mesh discussed in this paper is therefore representative of a majority of the modeling work reported in the literature. The three flux discretization schemes, together with the "Reconstruction-Flux" discretization for the Joule heating source term, were stable on the three meshes for time steps smaller than $\sim 10^{-9}$ s. The same discretization scheme was used for all the species fluxes and energy fluxes. Starting from arbitrary initial conditions, a steady state was reached after $\sim 10^{-4}$ s. Fig 5.5 shows the computed current density obtained at steady state for the different face flux discretization schemes on the three meshes. Only the exponential scheme provides reasonably accurate results on the coarsest mesh. The central scheme fails to yield accurate results on coarse meshes. Negative values and oscillations appear for the electron density and electron temperature profiles in the cathode sheath region, which pollute the entire solution. The upwind scheme is the most diffusive, and provides the least accurate solution even on the 1000-cell mesh. The good agreement between the solutions from the different schemes on the finest mesh confirms that all the numerical schemes are consistent. The "Reconstruction-Flux" discretization for the Joule heating source term was compared to the approach presented in [48] and both methods yield similar results for the different face flux discretization schemes. The difference in the computed current density was typically less than 1%.

The "Recomputed-Flux" Joule heating term discretization was also tested on the different meshes and with the three face flux discretization schemes. The upwind scheme, combined with the "Recomputed-Flux" discretization, was found to be unstable on the three meshes (for arbitrarily small values of the time step). For time steps smaller than $\sim 10^{-9}$ s, the central difference scheme is stable only on the 1000-

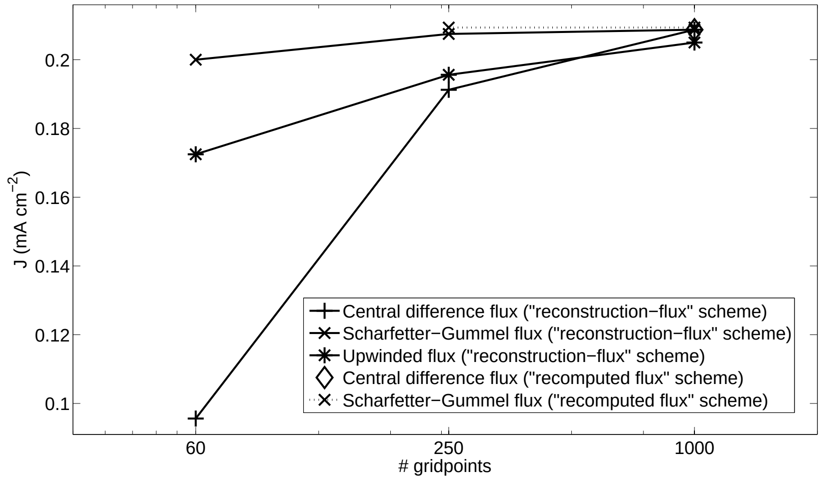

Figure 5.5: Computed current densities obtained on one-dimensional meshes with the different numerical schemes (see Fig 5.3 caption for physical conditions of the discharge).

cell mesh, while the exponential scheme is stable on the 250- and 1000-cell mesh. Fig 5.5 shows the current density obtained with the Recomputed-Flux Joule heating discretization for those cases where a stable solution was obtained. The accuracy of the solutions is comparable with those obtained with the "Reconstruction-Flux" Joule heating term discretization. Figure 5.6 shows the electron fluxes at the cell centers computed with the Scharfetter-Gummel exponential discretization scheme on the 250-cell and 1000-cell meshes. The "Recomputed-Flux" Joule heating term discretization fails to accurately estimate the electron flux on coarse meshes. The drift and diffusion components of the electron fluxes are sharply peaked at the cathode sheath and largely cancel each other if evaluated properly. The "Recomputed-Flux" discretization yields a non-monotonic electron flux on coarse meshes, which leads to numerical instabilities and therefore fails to predict discharge phenomena accurately.

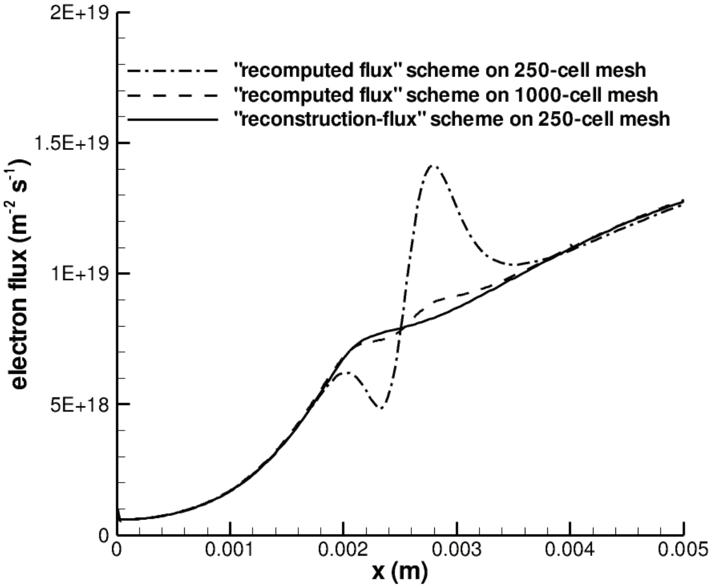

Figure 5.6: Computed electron fluxes on one-dimensional meshes with different numerical schemes (see Fig 5.3 caption for physical conditions of the discharge). The figure shows a close-up of the solution in the cathode sheath region.

Two-dimensional mesh

The above one-dimensional test case is now simulated using two-dimensional unstructured meshes by applying appropriate zero-flux boundary conditions for all equations in the second direction. Three different unstructured meshes are used to demonstrate our proposed “Reconstruction-Flux” discretization for the Joule heating source term. These two-dimensional meshes are shown in Fig. 5.7. Mesh (a) in Fig. 5.7 comprises relatively uniform triangles and is coarser than the triangular mesh (b) which is refined toward the cathode. Mesh (c) contains both triangular and quadrilateral cells and comprises highly skewed cells. The presence of highly skewed cells in mesh (c) leads to high discretization errors and can also affect stability of the numerical schemes. Meshes (a), (b), and (c) comprise 2016, 4972 cells, and 2228 cells, respectively. As with the one-dimensional meshes, the three face flux discretization schemes, together with the “Reconstruction-Flux” Joule heating discretization, are stable for time steps smaller than $\sim 10^{-9}$ s. Table 5.2 shows the current density obtained with the different numerical schemes. For comparison, the mesh-converged current density (obtained with the central-difference scheme or Schafetter-Gummel scheme on the 1000-cell one-dimensional mesh) was 0.209 mA cm^{-2}. The central difference discretization scheme is the most accurate method on the triangular meshes while the solution obtained with the Scharfetter-Gummel scheme is reasonably accurate. No oscillations or negative values of the electron temperature or electron density are observed on the two-dimensional triangular meshes. On mesh (c), the exponential scheme yields the most accurate results (small oscillations appears the for central difference scheme). The solution obtained with the upwind discretization scheme is quite diffusive on all meshes. Fig. 5.7 show the electron temperature profiles obtained with the exponential scheme. The nonuniformities that appear in the transverse direction (direction parallel to electrode plane) on mesh (c) clearly show the limitations of our first-order model for highly skewed cells.

The “Recomputed-Flux” Joule heating term discretization combined with the upwind or Scharfetter-Gummel exponential face flux discretization scheme is unstable on all the unstructured meshes (regardless of the value of the time step). Only the central-difference scheme is stable with this method for the two triangular unstructured meshes. This confirms that the “Recomputed-Flux” discretization is less robust than the “Reconstruction-Flux” discretization approach. As shown in Table 5.2, the results obtained with the “Recomputed-Flux” discretization are also less accurate than those obtained with the “Reconstruction-Flux” discretization.

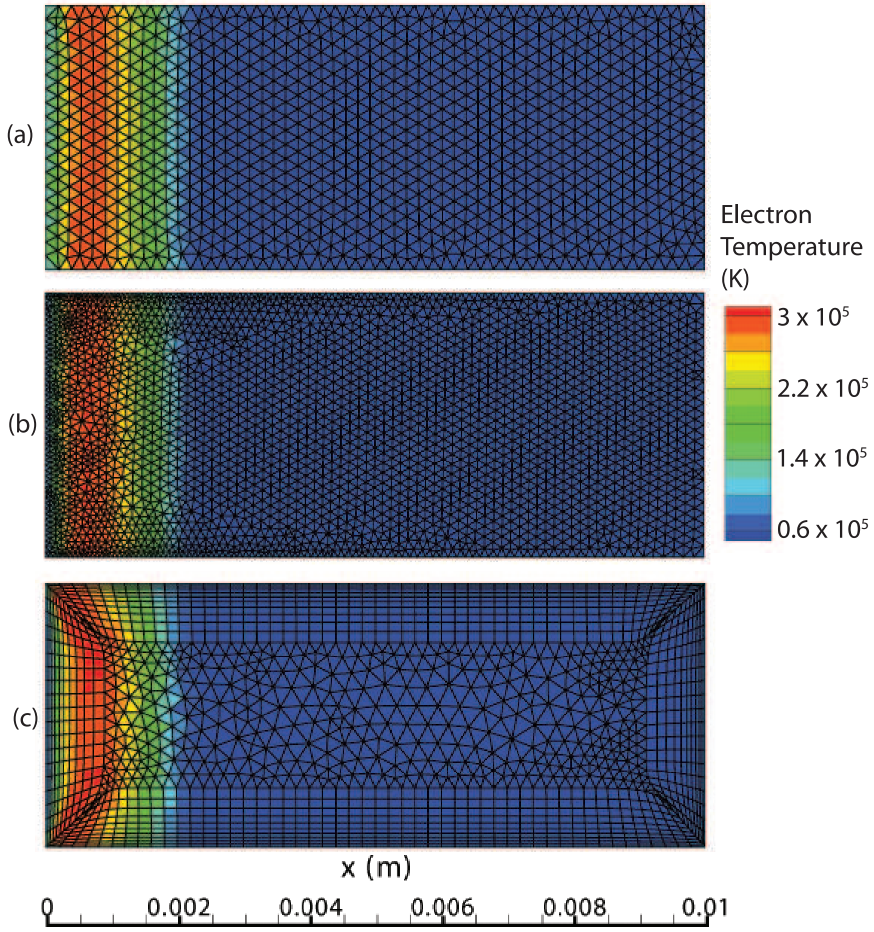

Figure 5.7: Computed electron temperature profiles obtained with the “Reconstruction-Flux” method (combined with the exponential discretization of the fluxes) on two-dimensional unstructured meshes (see Fig 5.3 caption for the conditions of the discharge).

	"Reconstruction-Flux" scheme			"Recomputed-Flux" scheme		
	Upwind	Central	S-G	Upwind	Central	S-G
Coarse triangular mesh (a)	0.167	0.198	0.193	×	0.181	×
Refined triangular mesh (b)	0.184	0.208	0.205	×	0.205	×
Mixed triangles and quadrilaterals with skewed cells mesh (c)	0.166	0.225	0.211	×	×	×

Table 5.2: Computed current densities (in mA cm^{-2}) obtained on the two-dimensional meshes with the different numerical schemes (see Fig 5.3 caption for conditions). The mesh-converged current density (obtained with the central-difference scheme on the 1000-cell one-dimensional mesh) is 0.209 mA cm^{-2}. Crosses indicate that a stable solution could not be obtained due to numerical instabilities.

5.3 Flow module

A Navier-Stokes solver has being developed in our research group [78, 79]. For the MPT studies, the governing equations are the time-dependent compressible Navier-Stokes equations in axisymmmetric form and can be written as

$$\frac{d\mathbf{U}}{dt} + \vec{\nabla} \,.\, \vec{\mathbf{F}}_{\text{inviscid}} = \vec{\nabla} \,.\, \vec{\mathbf{F}}_{\text{visc}} + \mathbf{S} \tag{5.36}$$

where $\mathbf{U}$ represents the conservative variables

$$\mathbf{U} = \begin{bmatrix} \rho \\ \rho V_x \\ \rho V_r \\ \rho e_t \end{bmatrix},$$

$\vec{\mathbf{F}}_{\text{inviscid}}$ represents the inviscid flux terms

$$\vec{\mathbf{F}}_{\text{inviscid}} = \begin{bmatrix} \rho V_x \\ \rho V_x^2 + P \\ \rho V_x V_r \\ (\rho e_t + P) V_x \end{bmatrix} \hat{\mathbf{n}}_x + \begin{bmatrix} \rho V_r \\ \rho V_r V_x \\ \rho V_r^2 + P \\ (\rho e_t + P) V_r \end{bmatrix} \hat{\mathbf{n}}_r \ ,$$

$\vec{\mathbf{F}}_{\text{visc}}$ represents the viscous flux terms

$$\vec{\mathbf{F}}_{\text{visc}} = \begin{bmatrix} 0 \\ \tau_{xx} \\ \tau_{xr} \\ V_x \tau_{xx} + V_r \tau_{xr} - \dot{q_x} \end{bmatrix} \hat{\mathbf{n}}_x + \begin{bmatrix} 0 \\ \tau_{rx} \\ \tau_{rr} \\ V_x \tau_{rx} + V_r \tau_{rr} - \dot{q_r} \end{bmatrix} \hat{\mathbf{n}}_r \ ,$$

and $\mathbf{S}$ represents the source terms

$$\mathbf{S} = \begin{bmatrix} 0 \\ f_x \\ f_r + \frac{P - \tau_{\theta\theta}}{r} \\ \vec{f}.\vec{V} + S_{\text{Heat}} \end{bmatrix} .$$

In these equations,

$e_t = \dfrac{P}{\rho(\gamma - 1)} + \dfrac{1}{2}(V_x^2 + V_r^2)$ is the total fluid energy (thermal and kinetic),

$\dot{q_x} = -k\dfrac{\partial T}{\partial x}$ and $\dot{q_r} = -k\dfrac{\partial T}{\partial r}$ are the components of the heat flux,

$\tau_{xx} = -\dfrac{2\mu}{3}\vec{\nabla} \cdot \vec{V} + 2\mu\dfrac{\partial V_x}{\partial x}$

$\tau_{rr} = -\dfrac{2\mu}{3}\vec{\nabla} \cdot \vec{V} + 2\mu\dfrac{\partial V_r}{\partial r}$

$\tau_{\theta\theta} = -\frac{2\mu}{3}\vec{\nabla} \cdot \vec{V} + 2\mu\frac{V_r}{r}$, and

$\tau_{xr} = \tau_{rx} = \mu \left(\frac{\partial V_x}{\partial r} + \frac{\partial V_r}{\partial x} \right)$,

are components of the normal and shear stresses respectively.

$\vec{V} = V_x \hat{\mathbf{n}}_x + V_r \hat{\mathbf{n}}_r$ is the velocity vector,

$\vec{f} = f_x \hat{\mathbf{n}}_x + f_r \hat{\mathbf{n}}_r$ is the external body force per unit volume, and

S_{Heat} is the external volumetric heat source term.

The Navier-Stokes equations are also spatially discretized with a finite volume scheme. A dual-time stepping algorithm is used to generate time-dependent solutions. The inviscid flux terms are evaluated with the Advection Upstream Splitting Method (AUSM) [80]. The gradient reconstruction is performed by the Green-Gauss method (see Eq. 5.30). Limiters are used to ensure that the reconstructed value is bounded by the minimum and maximum of the cell centroid and the neighboring centroid values, i.e. the scheme preserves monotonicity. In this study, the flux-limiter scheme of Venkatakrishnan [81] has been employed.

Results from the flow module were validated by solving the cold micronozzle flow presented as the base case in Sec 4.3.2. The solution obtained with our flow module is nearly indistinguishable from the solution obtained with the commerical software Fluent.

5.4 Overall solution procedure

Figure 5.8 shows the numerical algorithm used to solve the plasma governing equations. Each update step advances the corresponding variable by a certain time step. The first step consists of solving the Poisson's equation for the electric field. The species continuity equation for the electrons is then solved, followed by the electron energy equation. The next step consists of updating the number densities of ion and metastable species. If needed, the momentum equation for each ion species is then solved. Finally, in case the flow solver is not used, the gas energy equation is solved. This process is repeated until a steady state is reached.

The stiffness of the governing equations due to the wide disparity in neutral and charged species times scales requires the use of several numerical techniques to speed up the convergence to steady state. For example, the update of the neutral species density and of the gas temperature is typically performed every 100 time steps. Also, the step size used for updating the neutral species number densities is about 2 orders of magnitude larger than that for the update of the electric potential and charged species number densities. Such procedures are essential to obtain steady state solutions within a reasonable amount of CPU time.

The Poisson's equation poses a numerical challenge because of the sensitivity of the electric potential to relatively small changes in charge densities. When Poisson's equation is solved explicitly (i.e, the electric potential for a future time is found using present values of the charged species densities), time step limitation given by the dielectric relaxation time (Δt_d) apply,

$$\Delta t_d = \frac{\epsilon_0}{\sigma}. \tag{5.37}$$

Here, σ is the plasma conductivity, which is $\sim$100 $(\Omega m)^{-1}$ for our microdischarge conditions (assuming electron number densities of $\sim 10^{20}$ m^{-3}), which results in $\Delta t_d \approx 10^{-14} - 10^{-13}$ s. A typical numerical procedure, which involves treating Poisson's equation semi-implicitly (e.g., [74]), has been used to overcome the step size limitation imposed by Δt_d . In this technique, Poisson's equation is solved using predicted values of the charged species number densities at a future time based on the present values of the time derivatives.

The characteristic time-step size for the solution of transport equations is the Courant-Friedrichs-Lewy (CFL) time,

$$\Delta t_{CFL} = \frac{\Delta x}{\mu_k E}, \tag{5.38}$$

where Δx is a characteristic grid dimension, μ_k is the mobility of species k, and

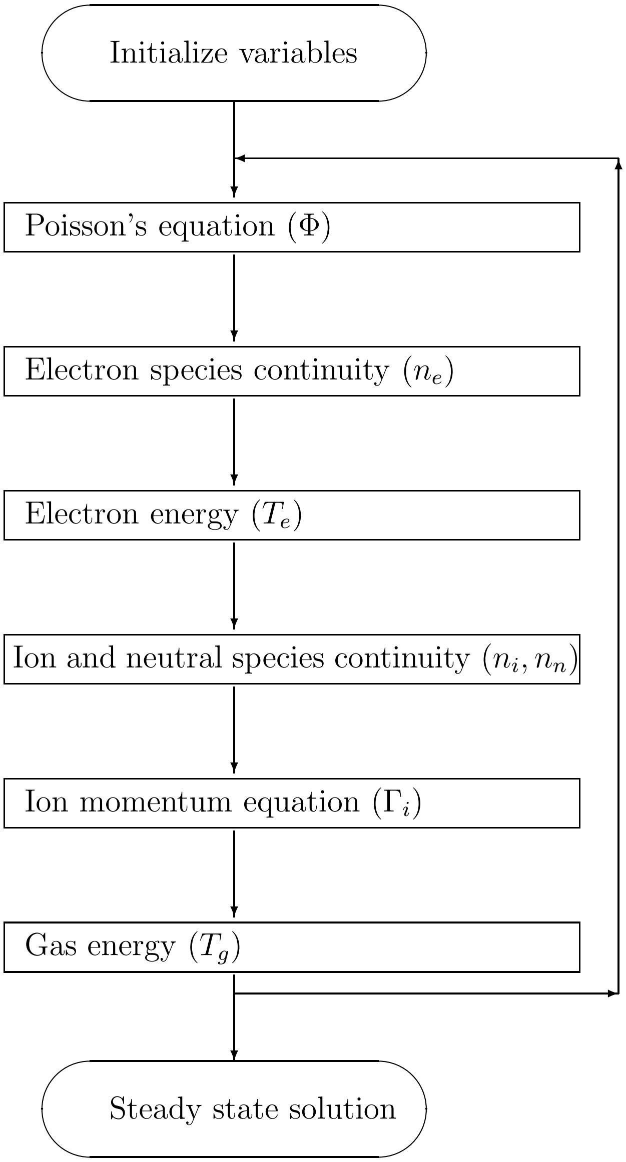

Figure 5.8: Numerical algorithm for the plasma module. Symbols in parentheses indicate which variables are updated.

E is the local electric field. Because of the high mobility of electrons, the limiting step size is usually the electron CFL time ($\sim 10^{-14}$ s for our conditions). The density in the transport term (Eq. 5.9) is treated implicitly to overcome the CFL time-step limitation. For our microdischarge simulations, time steps of the order of $\sim 10^{-13} - 10^{-12}$ s have been used for the governing equations of the charged species.

For each update step, the linear system resulting from the spatial and temporal disctretization of the relevant equation is solved using libraries provided by the PETSc (Parallel Extensible Toolkit for Scientific Computation) [82] package. The GMRES (Generalized Minimal Residual) method is employed with an incomplete LU factorization as a preconditioner. A relative tolerance of 10^{-8} and an absolute tolerance of 10^{-15} for the L_2 norm of the residual is used to identify convergence for the solution of the linear system at each time step.

The neutral fluid flow is obtained by solving the compressible Navier-Stokes equations on the same unstructured mesh as the plasma calculations. The flow solution influences the plasma discharge through the pressure, temperature and velocity fields (appearing in the gas discharge governing equations). On the other hand, electrostatic forces and electrothermal heating act as external body forces and external heat source, respectively, in the Navier-Stokes equations. These source terms are defined as

$$\vec{f} = \sum_i n_i(\vec{u}_i - \vec{V})\bar{\nu}_{i,k_b} - \frac{e n_e \vec{E}}{m_e}, \tag{5.39}$$

$$S_{Heat} = -\alpha_J\Big(e\sum_h Z_k\vec{\Gamma}_k \cdot \vec{\nabla}\Phi\Big) + \frac{3}{2}k_B n_e \frac{2m_e}{m_{k_b}}(T_e - T_g)\bar{\nu}_{e,k_b} - e\sum_{j=1}^{I_g}\Delta E_j^g r_j. \tag{5.40}$$

Figure 5.9 shows how the coupling between the plasma and flow modules has been implemented. Both modules run in parallel, on separate processors. After $\sim$1000 time steps, the plasma module passes the source terms to the flow module and reads the flow fields from the flow module. This process is repeated until a steady state is reached, which typically require $\sim$1000 rounds of data transfer between the modules.

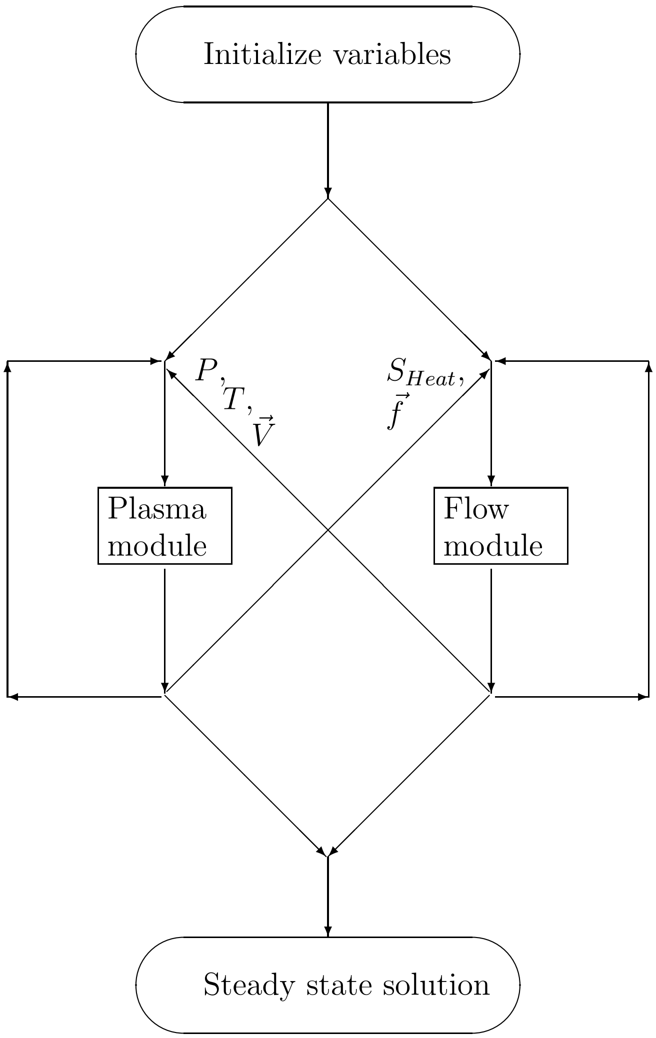

Figure 5.9: Numerical algorithm for the coupling between the plasma and flow modules

Chapter 6

Microhollow cathode discharges

Microhollow cathode discharges (MHCD) are stable, moderately high-pressure, non-equilibrium, sub-millimeter scale discharges generated in a geometry consisting of a cathode/dielectric/anode sandwich through which a blind or through hole is drilled. In this section, the plasma discharge model is used to help clarify physical mechanisms and understand different operating conditions of the MHCD. Necessary physical modeling approximations required to properly address microdischarge phenomena are discussed. Computational results for the impedance characteristics as well as electrodynamic and chemical features of the discharge are reported and compared to experimental results performed in a similar set-up [16].

6.1 Numerical details

For this study, the plasma discharge governing equations are solved without the inclusion of the flow module. The governing equations include the species continuity equations, the electron and gas energy equations, and the Poisson's equation; those equations have been described in detail in Sec 5.1.2. In the boundary-condition model for solid walls, an effective secondary emission coefficient formulation has been used for the electron flux. The model relates the total secondary electron emission flux from the surface to the net ion flux impacting the surface. The total secondary electron emission includes contributions from ion impact, fast atoms, metastable atoms, and ultraviolet photons. The effective secondary emission coefficient is approximated as a function of the reduced electric field at the cathode surface $(E/n_{k_b})_c$ as

$$\gamma_{eff} = 0.01 \left(\frac{E}{n_{k_b}} \right)_c^{0.6}, \tag{6.1}$$

where, the reduced electric field is expressed in units of kilo-Townsend (kTd). These values correspond to "practical" or "dirty" cathode surfaces interacting with an argon plasma [70, 72].

Farfield boundaries are defined as boundaries that are sufficiently far away from the primary discharge activity. Consequently, farfield boundaries do not pass a net electrical current. We implement farfield boundaries as essentially solid surfaces with a thin dielectric layer, backed by a grounded potential. All species density equation boundary conditions for a solid surface apply at the farfield boundary (without secondary electron emission for electrons). Also, the energy flux boundary condition at solid surfaces is used for the electron energy equation, while the gas temperature is fixed at 300 K at the farfield boundary.

Figure 6.1 shows the computational mesh and the cylindrically symmetric geometry of the MHCD used in this study. The geometry is similar to the one presented by Aubert *et al* [16], with a hole radius of 100 μm, metal foils (electrodes) of thickness 100 μm, and a dielectric layer thickness of 50 μm. As discussed earlier, outer farfield boundaries on the cathode and anode sides of the discharge are modeled as a thin dielectric layers with $\epsilon = 8\epsilon_0$. This boundary condition ensures that no secondary discharge is established between the electrodes and the outer boundaries given the finite size of the computational domain. The anode current therefore equals the cathode current without any other spurious current pathways in the domain. The radius of the outer cathode (starting from the symmetry axis) is 1mm.

The mesh consists of about 6200 cells of which about 5900 are in the plasma

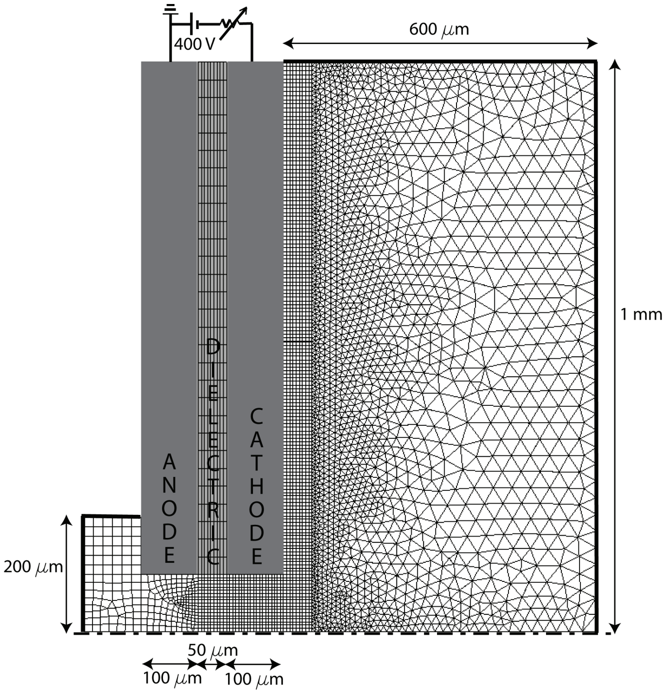

Figure 6.1: Schematic of the MHCD device and computational mesh. The geometry is cylindrically symmetric.

and about 300 are in the central dielectric layer. The electrodes are treated as perfect conductors and are therefore not meshed. The Poisson equation without a space charge is solved in the central dielectric layer. A combination of triangles and quadrilaterals is used in the plasma region to optimize requirements of solution resolution and cell count. The mesh is refined towards the cathode with quadrilaterals to capture the steep gradients that exist for most solution variables in the cathode sheath. In practice, the aspect ratio of quadrilateral cells in the high-gradient sheath region can be as high as 10. The use of a mixed cell (triangles and quadrilaterals) mesh constitutes a significant advantage compared to a pure triangle or pure quadrilateral mesh. With a pure triangle mesh the requirement of non-skewed cells for stability and accuracy reasons implies that the total cell count increases significantly if the high-gradient sheath regions are to be captured accurately. If a pure quadrilateral/rectangle cell mesh is used, the refinement in cathode sheaths has to be carried over to regions of the discharge that do not require such refinement and hence the overall cell count can again be much larger than a carefully designed mixed cell mesh.

MHCDs operate in regimes that have low or even negative differential resistivity. It is therefore difficult to stabilize the microdischarge by simply imposing fixed voltage boundary conditions at the electrodes. We use an external circuit model coupled to the discharge model. The external circuit model uses a series ballast resistance between the supply voltage and the anode. A constant dc supply voltage is applied, and the voltage at the electrode surface is determined based on the current through the discharge and Ohm's law. Different current levels can be established in the discharge by changing the ballast resistance.

6.2 Results and discussions

6.2.1 General discharge properties

The current-voltage ($I-V$) characteristics of the MHCD discharge predicted by the model is presented in Fig. 6.2. The predicted $I-V$ characteristics is compared to the experimental data presented in Fig. 2 of the paper by Aubert *et al* [16]. For the numerical results, two pressures of 50 and 100 Torr (corresponding to $pD =$ 1 and 2 Torr-cm, respectively, where D is the hole diameter) over a current range from about 0.02 to 1.2 mA are shown. Results obtained using a constant secondary electron emission coefficient of 0.03 at 50 Torr are also shown. For the model that includes the variable secondary emission coefficient, a negative differential resistivity regime is observed at low currents ($0.02 - 0.1$ mA), and a low positive differential resistivity regime is observed at higher currents ($0.3 - 1.2$ mA). In between these two regimes, a transition regime with larger positive differential resistivity is observed. This transition regime is characterized by oscillatory discharge behavior and hence the $I-V$ data in Fig. 6.2 for this regime are the time-averaged values. The three regimes observed experimentally present strong similarities with the computational results in our study (Fig. 6.2). However, at low currents ($<\sim$0.2 mA), a constricted regime with a steep positive differential resistivity is observed experimentally which we fail to predict using the computational model. The constricted behavior of the discharge inside the hollow at low currents is nonetheless reproduced by our model. At intermediate currents, an unsteady behavior of the discharge is observed both experimentally (the self-pulsing regime) and computationally (the oscillatory regime). For higher currents, our model captures the flat $I - V$ curve that is representative of the normal regime, where the plasma expands outside the hollow towards the cathode backside. The transition from the oscillatory regime to the normal regime occurs at a current of ∼0.3 mA in our model, while the normal regime is experimentally observed for a current of ∼1.1 mA or higher. From a discussion with the authors of [16], the degree of purity of argon used in the experiments appears to determine the range of currents for which the self-pulsing regime is observed. In recent experimental results obtained with high purity argon (not published), the transition to the normal regime is observed at a current of 0.6 mA. The result with a fixed secondary electron emission coefficient of 0.03 fails to predict these different regimes, thereby emphasizing the role of variable secondary electron emission processes in the MHCD phenomena.

We further discuss detailed results for discharge properties at data points A, B, and C in Fig. 6.2. These cases are for a constant pressure of 50 Torr, but with varying discharge currents of 0.032 (case A), 0.25 mA (case B), and 0.82 mA (case C). Case A is representative of the constricted regime, while cases B and C are representative of the normal regime. Both the 50 Torr and 100 Torr cases exhibit similar trends, with the higher pressures resulting in a more constricted discharge at a given current.

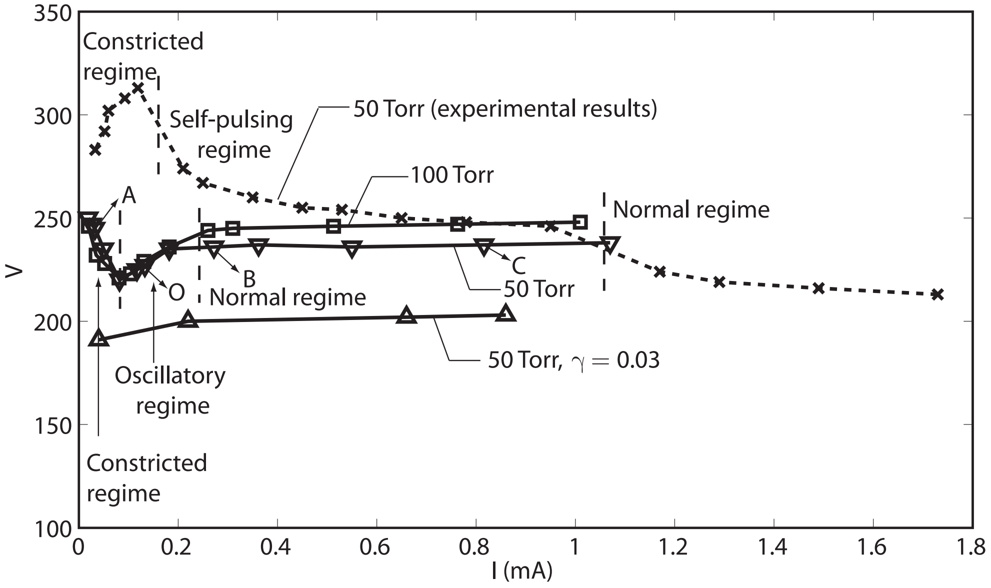

Figure 6.2: Comparison of experimental and simulated current-voltage ($I-V$) characteristics of the MHCD.

Figure 6.3 shows the electric potential contours in the discharge for the three cases. For case A, the cathode sheath thickness exceeds the radius of the hole. The electric potential gradients (or electric fields), within the hole are directed mainly along the hole axis and is close to the vacuum field for the geometry with small space charge distortion. For the higher current cases, a well defined ring-shaped (annular) sheath structure appears inside the hole adjacent to the cathode. For these cases, the cathode sheath is about 100 μm in thickness within the hollow and extends over the flat cathode surface outside the hollow. The sheath thickness, quantified by regions of large potential gradients adjacent to the cathode surface, increases with increasing radial distance over the flat outer cathode surface.

Electron, monomer ion (Ar^+) and dimer ion (Ar_2^+) number density profiles are shown in Figs. 6.4, 6.5, and 6.6, respectively. In all cases, a peak in the electron number density is observed at the centerline of the discharge within the hollow cathode region. A second peak appears outside the hollow for the higher current cases in the normal regime. The peak density is about 10^{19} #/m^3 in all cases and

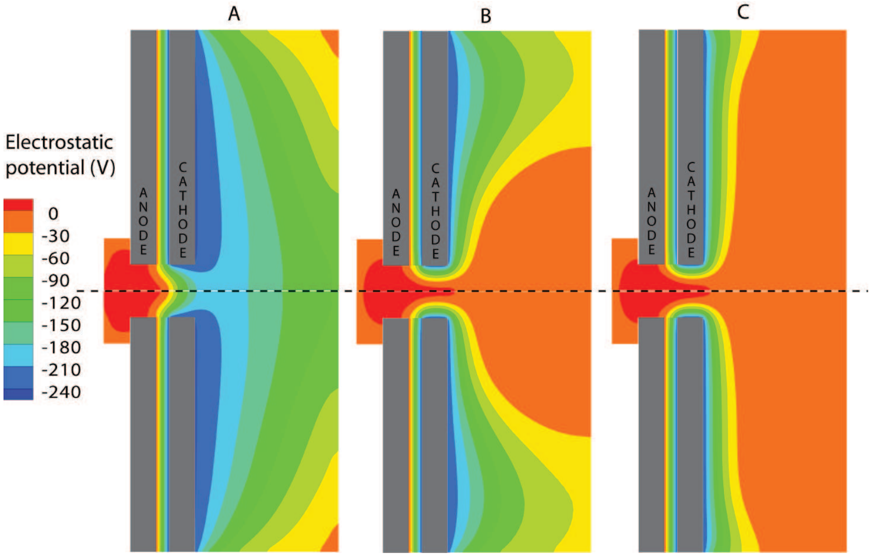

Figure 6.3: Plasma potential contours in the MHCD for case A, case B, and case C. (The operating conditions for these cases are indicated in Fig. 6.2)

increases with the current for a fixed pressure. The extent of the plasma volume outside the hollow increases with increasing current at a constant pressure. The ion density contours shown in Figs. 6.5 and 6.6 indicate that both monomer and dimer ions are important constituents of the plasma, in particular for the higher current cases in the normal regime. In all cases, the peak of the monomer ion density is observed at the centerline of the discharge within the hollow cathode region. For the cases in the normal regime, most of the dimers are located outside the hollow. Charged species loss due to wall quenching is less important outside the hollow resulting in larger lifetimes of the ionized species away from the hollow cathode region. This in turn allows for the slower three-body reaction G_{12} (see Table 5.1) to produce the dimer ions. For the higher pressure 100 Torr cases, the proportion of the dimers to the monomer ions increases since the three-body conversion reaction G_{10} via G_{11} and G_{12} favors the conversion of the monomer to the dimers (not shown).

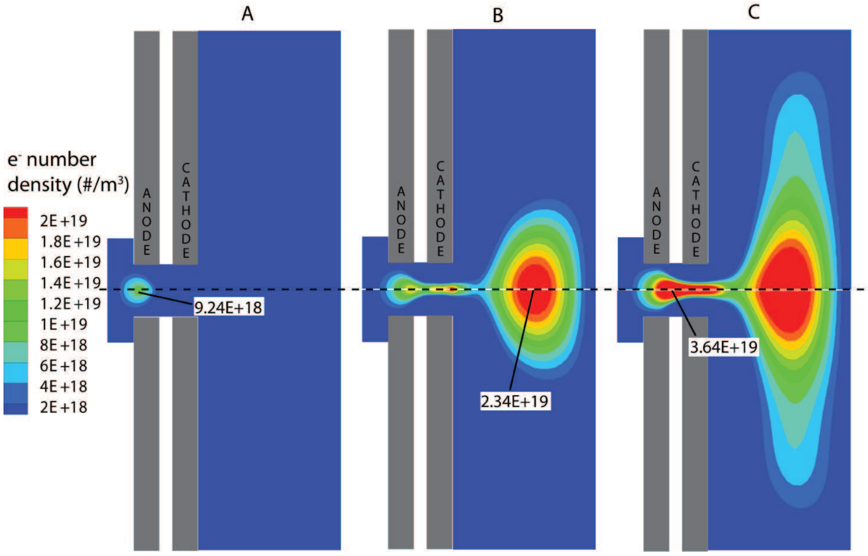

Figure 6.4: Electron number density contours in the MHCD for case A, case B, and case C. (The operating conditions for these cases are indicated in Fig. 6.2)

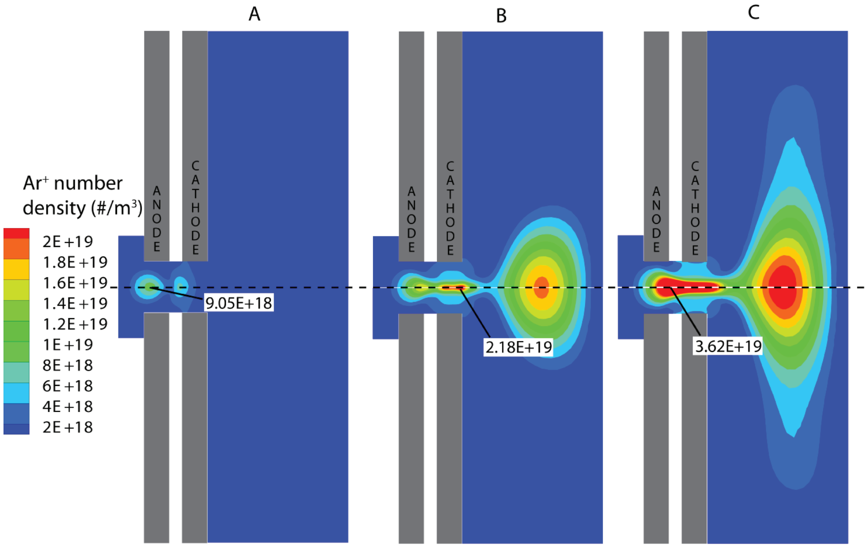

Figure 6.5: Monomer ion (Ar^+) number density contours in the MHCD for case A, case B, and case C. (The operating conditions for these cases are indicated in Fig. 6.2)

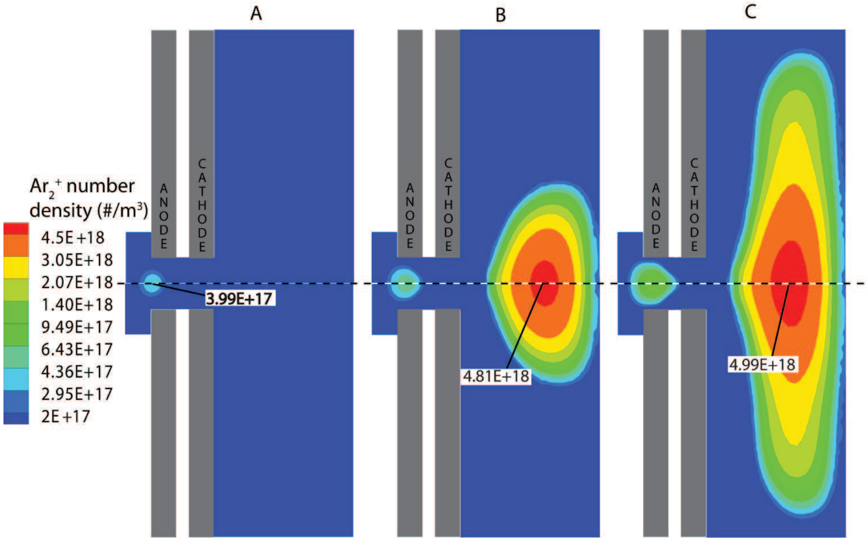

Figure 6.6: Dimer ion (Ar_+^2) number density contours in the MHCD for case A, case B, and case C. (The operating conditions for these cases are indicated in Fig. 6.2)

Figures 6.7 and 6.8 show the electron temperature and gas temperature contours, respectively. Electron temperatures are highest in the cathode sheath region within the MHCD hollow with peak temperatures of the orders of 20 eV. Only the region of the domain with significant electron numbers densities is shown in Fig. 6.7. The electron temperature in the bulk plasma is of the order of 1 eV. The cathode sheath electron temperatures increase with increasing currents for a fixed pressure. The gas temperature contours (Fig. 6.8) indicate non-negligible thermal heating of the gas for all cases. The peak gas temperature occurs along the discharge centerline in the vicinity of the hollow cathode. The gas temperature increases with increasing currents. In all cases, the ion Joule heating is found to be the dominant heating mechanism for the gas. Note that the gas temperature estimated in MHCDs in argon at 50 Torr by Penache *et al* [53] at 0.5 mA is about 400 K, which is in good agreement with our results.

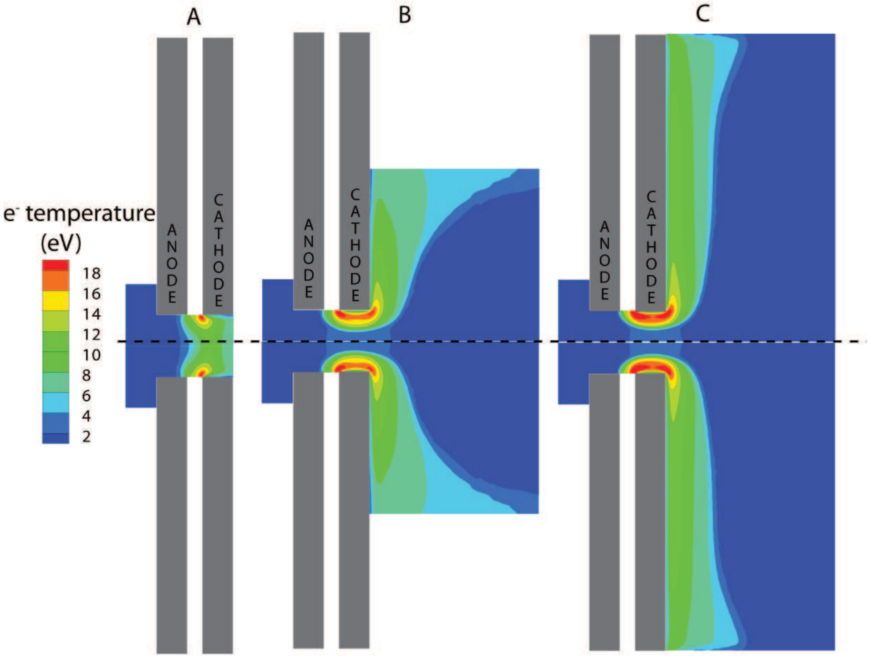

Figure 6.7: Electron temperature contours in the MHCD for case A, case B, and case C. (The operating conditions for these cases are indicated in Fig. 6.2)

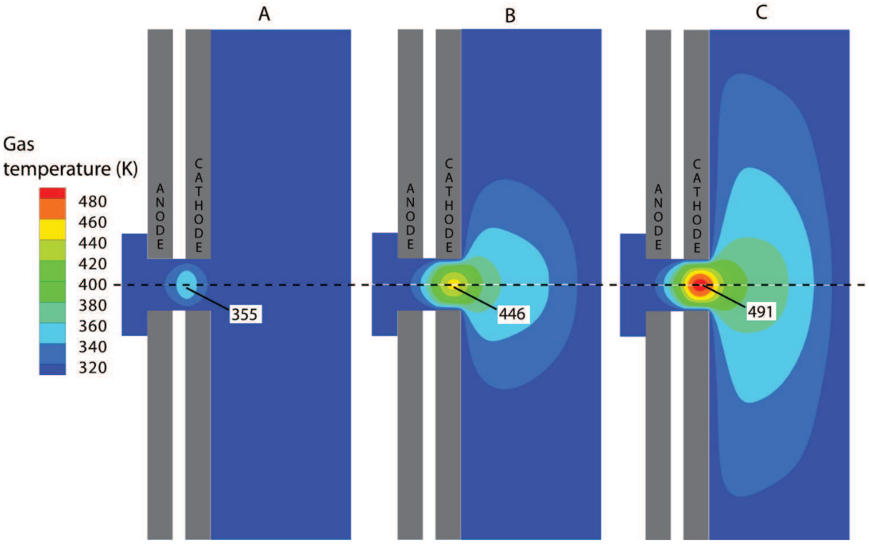

Figure 6.8: Gas temperature contours in the MHCD for case A, case B, and case C. (The operating conditions for these cases are indicated in Fig. 6.2)

Figure 6.9 shows contours for the net volumetric production rate of electrons through plasma reactions. In the low current constricted (abnormal) regime (case A), the electron production is confined to the hollow cathode region. At higher currents, discharge activity extends outside the hollow with significant electron production seen along the axis of the discharge immediately outside the hole on the cathode side and at the sheath edge of the flat outer cathode region. At sufficiently high currents the net electron production outside the hole exceeds the electron production within the hole.

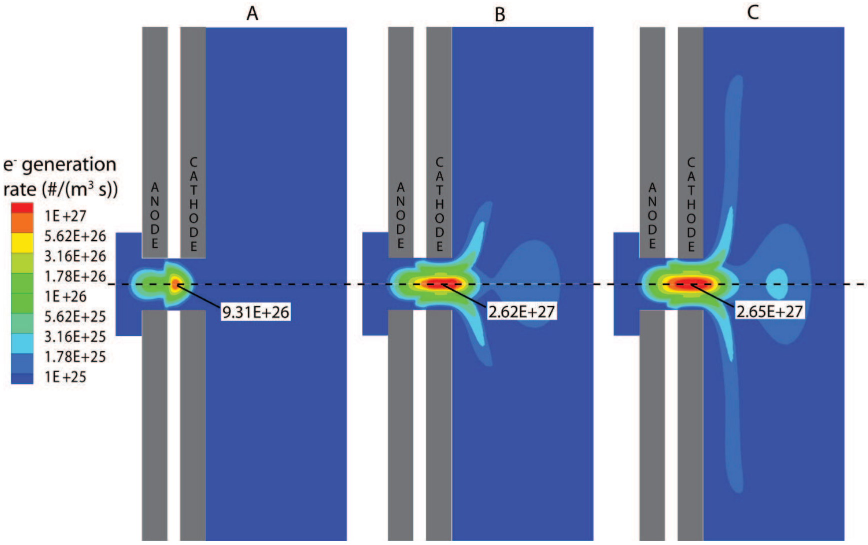

Figure 6.9: Net volumetric generation rate of electrons in the MHCD for case A, case B, and case C. (The operating conditions for these cases are indicated in Fig. 6.2)

6.2.2 Oscillatory regime

Periodic oscillations in discharge properties are observed for discharge currents ranging from about 0.1 mA to 0.3 mA. In Fig 6.2, this corresponds to the region between the minimum voltage point of the $I - V$ characteristics and the beginning of the normal regime. Figure 6.10 shows time transients of the currents through the hollow part of the cathode and through the flat outer cathode surface for two oscillation cycles. This simulation corresponds to point O in Fig. 6.2 with operating pressure of 50 Torr. The frequency of the oscillations is about 2 MHz. The discharge voltage remains relatively constant in this regime, since the total current passing through the ballast resistor (the sum of the currents through the hollow and outer flat cathode surfaces) remains nearly constant. Snapshots of the potential, electron density, and electron generation rate profiles are shown in Fig. 6.11 at different time instances during the oscillation cycle (indicated in Fig. 6.10). In this regime, the cathode sheath thickness is about the same size as the hollow radius. The discharge is characterized by two separate plasma zones that remain relatively static during the transients. A high density plasma zone is located within the hollow and another lower density plasma zone is located outside the hollow. The oscillation cycle is caused by the stable plasma within the hollow releasing a blob of plasma that moves along the axis in the direction of the cathode. Once this blob reaches a location just outside the hollow it rapidly merges with the stable outer plasma zone.

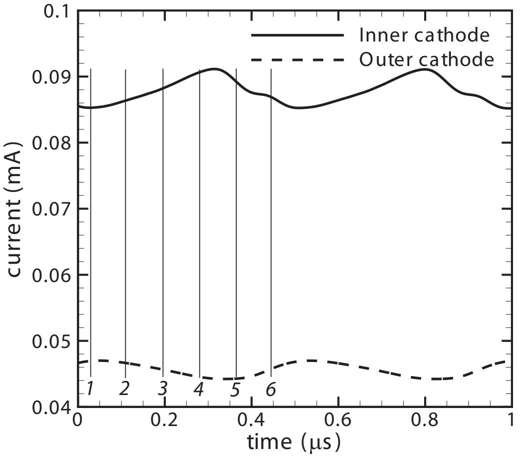

Figure 6.10: Time evolution of discharge currents through the hollow part of the cathode surface and through the flat outer cathode surface for two oscillation cycles.

The first snapshot of the electron density contours in Fig. 6.11 shows the formation of a new blob of plasma just as a previous blob located outside the hollow is beginning to merge with the outer stable plasma zone. In the second and following snapshots the new blob begins to detach from the plasma within the hollow until

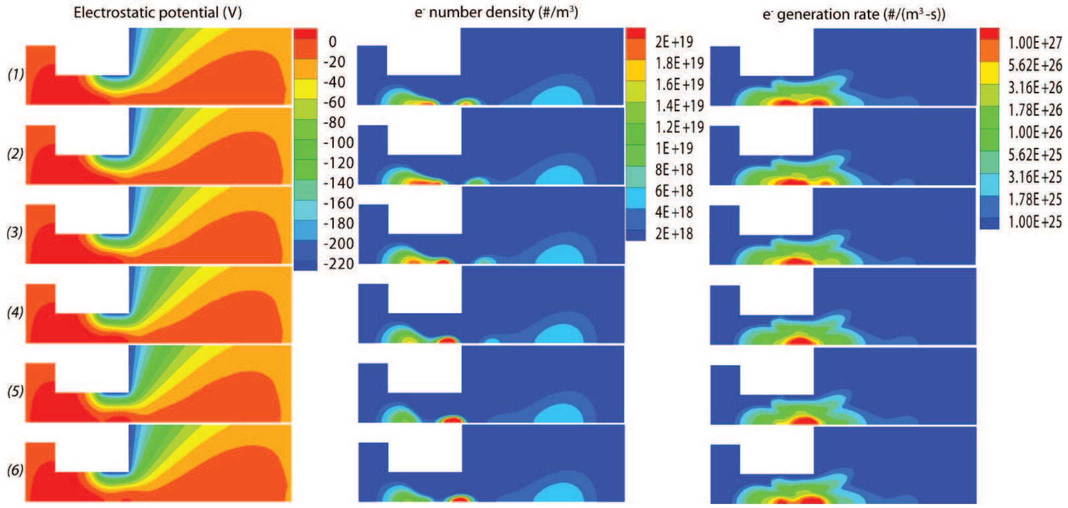

Figure 6.11: Snapshots of the electrostatic potential, electron number density, and electron generation rate profiles at different times of the oscillations. (The time indices (1)-(6) correspond to those indicated in Fig. 6.10)

it experiences the same fate as the previous blob. Snapshots for the electrostatic potential in the discharge undergo transient oscillations that are consistent with the motion of the plasma blob. High potential gradients (electric fields) coincide with the head of the blob as it moves along the axis, resulting in rapid ionization of the gas to sustain the motion of the blob. The motion of the blob is sustained by the ionization front, rather than a gross transport of charged particles detached from the stable plasma zone in the hollow. This is seen from the snapshots of the volumetric generation rate of the electrons/ions in Fig. 6.11. From snapshots of charged species fluxes (not shown) we observe that the net motion of electrons is from right to left (owing to drift transport), i.e. in the direction opposite to the blob motion, while the ions follow the motion of the blob. Electrons are rapidly accelerated through the potential gradient between blobs, and initiating an ionization avalanche that sustains the growth of the new blob. Once a blob leaves the hollow region, it is no longer sustained by electrons from the previous blob (which has already merged with the outer plasma zone), and starts decaying as it provides seed electrons to the new blob. Ions from the blob are eventually lost due to quenching at the cathode.

Recombination of the ionized species due to chemical reactions occurs at much larger time scales than the blob motion and plays a negligible role in the decay mechanism.

Self-pulsing regimes have been observed experimentally [16] in the medium current range (∼0.1 − ∼1mA). In [16], the voltage is observed to increase up to a critical value at which it abruptly declines to a lower value, typically several hundred volts less than the peak value. The current is very low during the voltage build-up (∼0.1 mA), and peaks sharply to tens of mA for a brief period, then returns to near-zero. The cycle then repeats at frequencies ranging from tens of kHz to hundreds of kHz, which is more than an order of magnitude lower than the observed frequency of our oscillations. In [16], the current pulse is related to a fast expansion of the plasma on a large region of the outer cathode surface (∼3 mm in radius), while in our case the plasma outside the hollow is confined in a relatively small volume (∼0.1 mm in radius). As in the experimentally observed pulsing [16], the frequency of our oscillations increases with the mean discharge current. Previous simplified models based on an equivalent electrical circuit of the microplasma [16,83] needed to include an external device capacitance in order to model the self-pulsing phenomena and the frequency of the experimentally observed pulsing was also found to be affected by including an external capacitor. In our simulations, the frequency of the oscillations was found not to be affected by the addition of a capacitor in the external circuit, in between the two electrodes. A self-consistent model for the displacement current through the electrode-dielectric interfaces may help capture the dependency of the oscillations frequency on the device capacitance. In summary, although the oscillations in [16] are of a different nature compared to the oscillation seen in out computational study, the unsteady oscillatory feature of the discharge in the medium current range is predicted by our model.

The relatively high discharge voltage observed in our $I-V$ characteristics at low currents with the variable electron yield model is consistent with the higher voltages reported for the constricted regime in [16]. However, our model is not able to capture a positive differential resistivity regime at very low currents [16], which can be attributed to a weak Townsend-like discharge regime. Also, the experimentally observed voltage difference between the constricted and normal regime is about 100 V, which is higher than the voltage increase in our $I-V$ characteristics. Previous numerical studies of the MHCD failed to capture the increase in voltage for the constricted (abnormal) regime [35, 52]. Results from the different models presented in Fig. 6.2 show that the variable secondary electron emission coefficient allows us to capture this phenomenon. In this model, the emission coefficient decreases as the normal component of the electric field decreases (see Eq. 6.1). Figure 6.12 shows the plasma potential contours and electric field vectors in front of the cathode for cases A (representative of the constricted regime) and B (representative of the normal regime). Since the cathode sheath thickness is larger for case A, the average surface-normal electric field is lower for the constricted (abnormal) case than for the normal regime case. The low effective yield of electrons at the cathode in the constricted case results in a higher voltage needed to sustain the discharge in this regime.

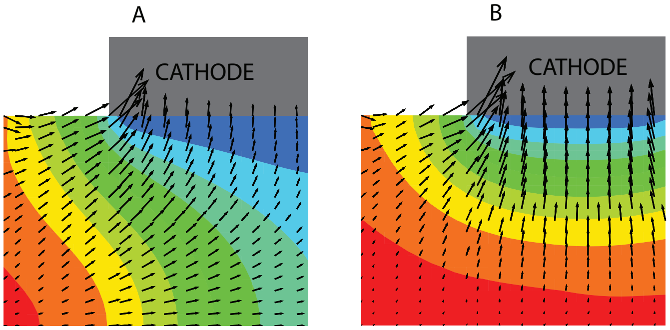

Figure 6.12: Plasma potential contours and electric field vectors in front of the cathode for case A and case B. (The operating conditions for these cases are indicated in Fig. 6.2)

6.2.3 Additional comments

Several observations can be made regarding the requirements for computational modeling of the MHCD and microdischarges in general. From the solutions presented for the constricted regime (case A), it is clear that all discharge activity is confined to the hollow and near hollow region. Consequently, the geometrical size of the computational domain can be greatly reduced for the simulation in this regime. This can be important considering the relatively large CPU time requirement of about 300 hours for a typical MHCD run with the full mesh on a 2.8 GHz workstation. A smaller domain with about 800 cells in the gas has been used for some of the data points presented in Fig. 6.2 and the accuracy of the solutions with the smaller domain are verified by comparisons with solution obtained with the full mesh (see Fig. 6.1). The CPU time requirement for the smaller domain size problem is about 40 hours. The large computational domain which covers significant radial distances over the flat outer cathode surface are required to simulate the higher current normal regime (with low differential resistivity). In fact for the full mesh used in our studies we can only achieve a maximum of $\sim$1.5 mA discharge current before the discharge fills the entire outer flat surface of the cathode and a further increase in current can be achieved only with a non-physical increase in discharge voltage. This is simply a physical modeling artifact. Absence of a clear low differential resistivity regime in previous numerical investigations is most likely a consequence of limited geometrical size of their numerical domain [35, 52].

The large driving forces (electric fields) in the MHCD can limit accuracy of the drift-diffusion approximation (Eq. 5.9), especially for ions. We have performed additional simulations for some cases with the ion momentum equation used instead of the drift-diffusion approximation for ion transport. Results for these cases are nearly indistinguishable from cases where the drift-diffusion approximation is used for the ions indicating that this approximation is adequate for simulation of typical MHCD operating conditions discussed in this study.

6.3 Summary

Discharge phenomena in an argon microhollow cathode discharge (MHCD) are investigated using a two-dimensional fluid computational model. MHCD with operating pressures of 50 and 100 Torr are modeled, with discharge currents ranging from ∼0.02 to ∼1 mA. Several operating regimes of the MHCD are observed. At low currents ($< \sim 0.1$ mA), our model predicts the discharge is constricted within the hollow in agreement with experiments [16, 34]. For larger currents ($> \sim 0.3$ mA), a significant part of the discharge volume lies outside the hollow structure with the plasma occupying a region of a few hollow diameters above the flat cathode surface plane. In this regime, the discharge operates as a normal glow; an observation that is again confirmed by experimental data available in the literature. Our model includes a surface-normal electric-field dependent electron secondary emission coefficient which allows the model to capture the rise in discharge voltage that is observed experimentally in the low-current constricted regime. Charged species densities of the order of 10^{19} $\#/\mathrm{m}^3$ are predicted for the conditions investigated. Electron temperatures of the order of 15 eV in the cathode sheath and of the order of 1 eV in the bulk plasma are predicted. Gas heating is significant particularly for the higher-current normal regime where gas temperatures of up to 200 K above room temperature are predicted. This is also consistent with experimental data [53].

Oscillations in the numerical solutions are observed for intermediate discharge currents ranging from ∼0.1 mA to ∼0.3 mA. These oscillations show some similarities with the self-pulsing regime reported experimentally by [16] which was also observed to occur at intermediate currents between the constricted and normal regime. The frequency of the oscillations increases with the averaged current as for the experimentally observed pulsing. However, some important discrepancies concerning the shape and the frequency of the oscillations still need to be reconciled.

Chapter 7

Micro Plasma Thruster studies

The simulation of microdischarges in the presence of bulk gas flow for microthruster applications is the subject of this chapter. We will identify important effects of the microhollow cathode discharge on the micronozzle flow. Spatial distributions of various plasma and flow parameters such as species number densities, electron and gas temperatures, and flow velocity fields are presented for different values of the power input. The sensitivity of the results to certain model parameters will be discussed.

7.1 Numerical details and operating conditions

Figure 7.1 shows the geometry of the MPT used for the simulations. The geometry of the micronozzle and the boundary conditions for the flow module are similar to those employed for the micronozzle flow studies (Sec. 4.3.2). The ring shaped electrodes have an axial thickness of 150 μm, while the dielectric layer has an axial thickness of 550 μm. The mesh consists of $\sim$3600 cells, which include a combination of triangles and quadrilaterals.

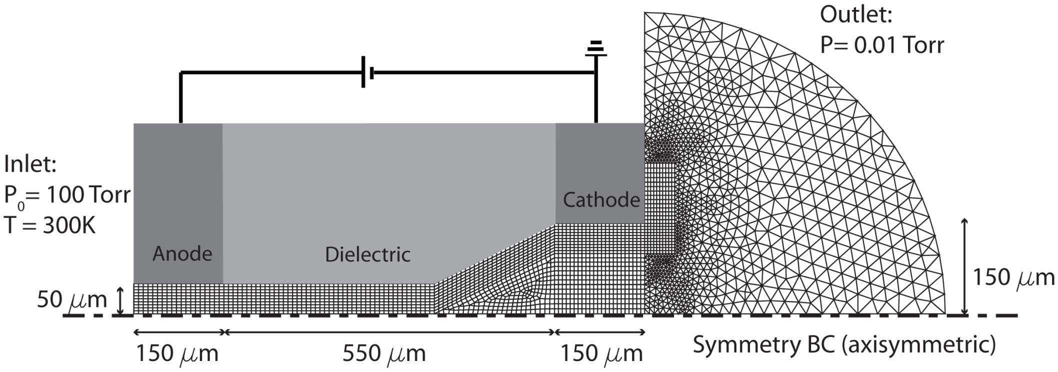

Figure 7.1: Schematic of the MPT device and computational mesh. The geometry is cylindrically symmetric.

The boundary conditions used in the plasma module are summarized in Table 7.1. We refer the reader to Sec. 5.1.4 for the detailed implementation of these boundary conditions. For numerical stability reasons, zero-flux boundary conditions were used for the gas discharge governing equations at the inlet and outer cathode surface boundaries. These boundaries are sufficiently away from the main discharge region and do not influence the presented results. The farfield boundary on the right side of the computational domain is modeled as an "outflow" boundary, where the plasma variables are convected away by the bulk flow. The value of the plasma variable from the adjacent interior cell is used to interpolate the flux at this farfield boundary. The power input is provided by applying a fixed positive DC voltage at the anode (without ballast resistance), while the cathode is grounded. The effective secondary electron emission coefficient (γ_{eff}, see Eq. 5.18) is set at a value of 0.03.

Because of the low pressures encountered in the diverging section of the micronozzle, the thermal power deposition field (originating mostly from the ion Joule heating) requires special treatment. The energy-relaxation length of the ions is of the same order as the thickness of the cells close to the cathode (∼5 μm). Ions that are being accelerated close to the cathode are likely to release their energy directly to the solid cathode and not thermalize with the gas. We modeled this phenomena with a variable fraction of ion Joule energy thermalized with the gas

	Species cont.	e^- energy	Electric potential	Ion momentum
Inlet	zero flux	zero flux	zero flux	zero flux
Anode	wall flux	wall flux	imposed potential	zero flux
Dielectric	wall flux	wall flux	Gauss's law	extrap. flux
Inner cathode	wall flux	wall flux	imposed potential	extrap. flux
Outer cathode	zero flux	zero flux	zero flux	zero flux
Outlet	outflow	outflow	zero flux	outflow
Symmetry BC	zero flux	zero flux	zero flux	zero flux

Table 7.1: Boundary conditions used in the MPT geometry. See Sec. 5.1.4 for detailed implementation of the boundary conditions

(α_J in Eq. 5.4) that is set to zero if the distance from the cell center to the cathode is less than the energy-relaxation length. For the set of boundary conditions that we used, this model does not affect the flowfield solution since most of the thermal power deposited in the vicinity of the cathode would be lost to the isothermal solid surface by conduction.

Table 7.2 lists discharge conditions for which results are presented. Here, the characteristic discharge dimension D is taken to be the thickness of the dielectric layer located between the electrodes (550 μm) and the characteristic pressure is taken to be the inlet total pressure. Cases from series A are simulated with the same inlet pressure (and flow rate), but with different input powers. The total pressure imposed at the inlet determines the mass flow rate, which does not depend on the power input of the microdischarge. This is due to the fact that the flow is choked and that most of the actuation effects from the microdischarge take place in the diverging section of the micronozzle.

Case	Inlet total pressure (Torr)	PD (Torr-cm)	Flow rate (sccm)	Voltage (V)	Current (mA)	Power (mW)
A1	100 Torr	5.5	5.2	750	0.87	650
A2	100 Torr	5.5	5.2	850	1.2	1020
A3	100 Torr	5.5	5.2	1000	1.8	1800

Table 7.2: Operating conditions for the MPT geometry

7.2 Results and discussions

7.2.1 Base case

We will consider our base case to be the case A1, for which the inlet total pressure is 100 Torr, the discharge voltage is 750 V, and the discharge current is 0.87 mA. Plasma properties at steady state are shown in Fig. 7.2 for the base case. The charge density is high enough that the bulk plasma extends well into the cylindrical micronozzle creating a hollow-cathode-like annular cathode sheath. Under these operating conditions, the cathode sheath is about 100-μm thick (see Fig. 7.2.a), occupying a significant fraction of the total discharge volume. In the cathode fall, the potential drops by nearly 750V over ~100 μm producing a characteristic electric field strength of ~75 kV cm^{-1} and a reduced electric field (electric field/gas number density) of ~10^5 Townsend. Results for the electron temperature in Fig. 7.2.b are only shown for volumes where the electron number density is greater than 3×10^{17} #/m^3 (10^{-3} of the peak value of the electron number density). The electron energy content is negligible in the rest of the domain. The electron temperature remains nearly uniform (around 2 eV) over most of the constant area pipe section, and gradually increases in the diverging section of the device to temperatures around 3 eV at the cathode sheath edge.

The electron density, shown in Fig. 7.2.c, has two peaks. The first peak is inside the constant area pipe section (~7×10^{19} #/m^3), and the second peak is in the diverging section of the nozzle (~3×10^{20} #/m^3). The well-defined sheath structure and relatively high electron densities indicates that the discharge is operating in the glow discharge mode rather than the Townsend/predischarge mode. The generation rate of electrons in the discharge through gas-phase reactions is shown in Fig. 7.2.d. Significant generation of electrons is observed in a region encompassing most of the micronozzle with maximum generation observed in the diverging section. This location corresponds to a relatively high electron temperature (~3 eV) and high background density region. The argon monomer ion (Ar^+) and dimer ion (Ar_2^+)

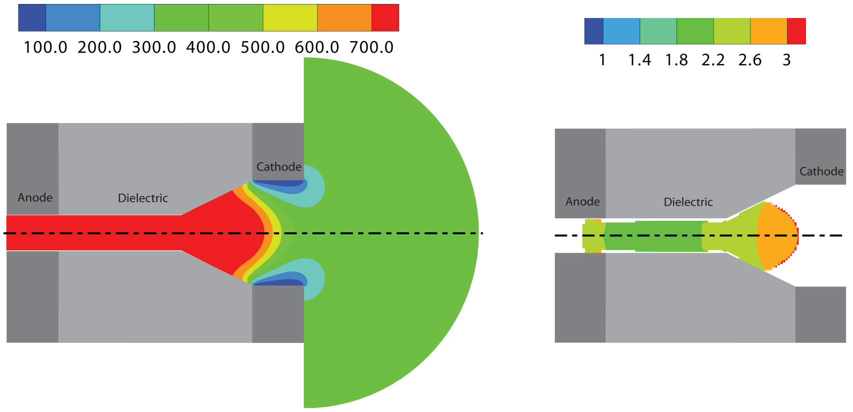

(a) Electrostatic potential (V) (b) Electron temperature (eV)

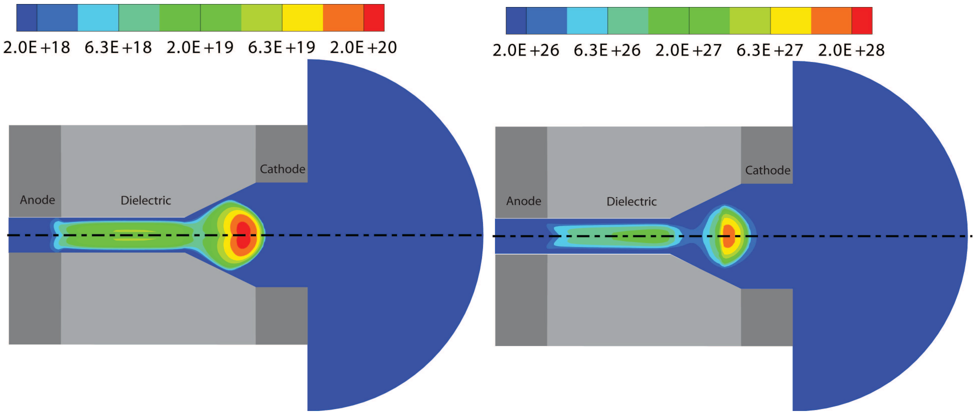

(c) Electron number density ($\#/\mathrm{m}^3$) (d) Electron generation rate ($\frac{\#}{\mathrm{m}^3\mathrm{s}}$)

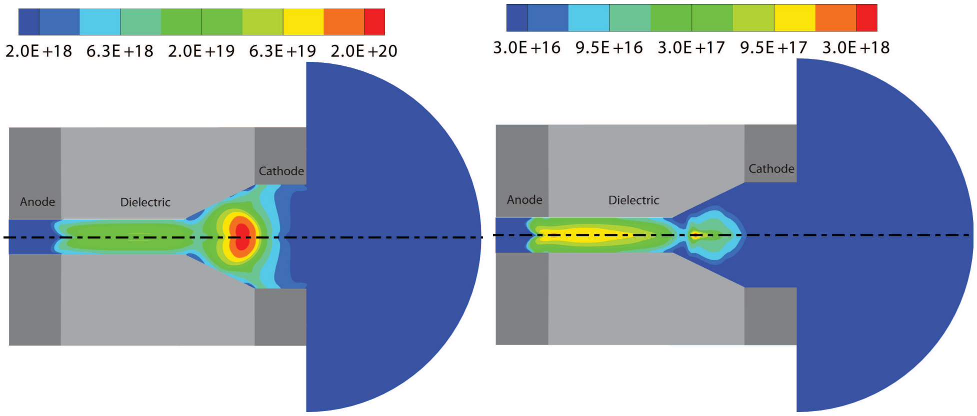

(e) Ar^+ number density ($\#/\mathrm{m}^3$) (f) Ar_2^+ number density ($\#/\mathrm{m}^3$)

Figure 7.2: Plasma properties in the MPT. The inlet total pressure is 13300 Pa (100 Torr) and the flow rate is 5.2 sccm. The applied potential difference between the electrodes is 750 V and the power input is 650 mW.

number densities are shown in Figs. 7.2.e and 7.2.f, respectively. Atomic argon ions constitute the dominant ion species in the microdischarge. High background densities favour the three-body reaction G_{12} (see Table 5.1) that forms dimer species. Therefore, most dimer ions are located in the constant area pipe section, where the pressure is relatively high. The ratio between the ions and the background species density does not exceed 10^{-3} throughout the nozzle, which indicates that the additional thrust due the electrostatic acceleration of the ions will be a small fraction of the value of the thrust due to the neutral flow. The electron and ion number density profiles show that the plasma is quasi-neutral in most of the micronozzle, except in the cathode fall and near the dielectric boundaries. The excess of ions near the dielectric boundaries indicates that the dielectric surfaces are slightly cathodic owing to net negative charge trapping at the dielectric surface. Since the electron wall flux equals the ion wall flux (at steady state), no net current is drawn through the dielectric surfaces.

The ion flux vector field, computed using the ion momentum equation (Eq. 5.8), is shown in Fig. 7.3. Significant differences in the results (about 20% for the peak value of the ionized species densities) were observed for cases where the drift-diffusion approximation was used (not shown), confirming the non-negligible effect of the ion inertia in the MPT configuration. It can be seen that most of the ions are quenched at the cathode and dielectric walls, and that a very small fraction of ions leave the nozzle (the ratio between the integrated flux value of ions leaving the thruster and impacting solid surfaces is less than 1%). This relatively small fraction of ion species expelled from the nozzle can be attributed to the large surface/volume ratio of the device (that favours wall quenching), and to the electric field distribution that propels most of the ions to the cathode. The small value of the ion flux at the exit plane results in an insignificant contribution of the electrostatic component of thrust to the overall thrust of the device.

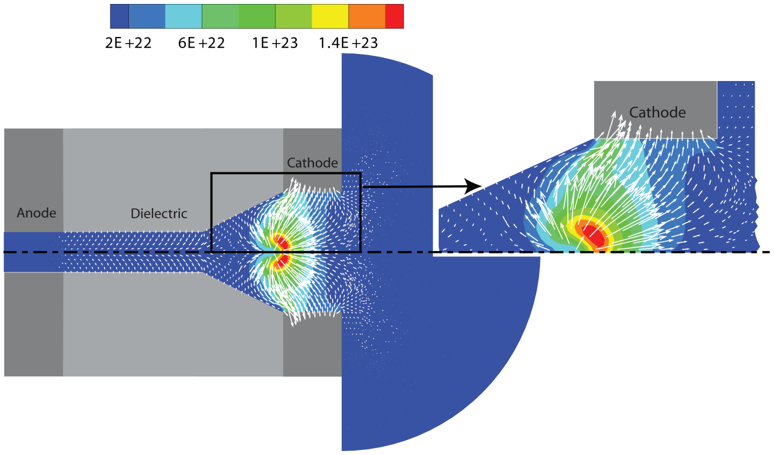

Figure 7.3: Ion flux ($\frac{\#}{\mathrm{m^2 s}}$) in the MPT. (The operating conditions are indicated in Fig. 7.2 caption)

The consequences of the presence of the microdischarge on the flow properties are shown in Fig. 7.4. The computational simulations confirm that the momentum source term (the electrostatic body force, Eq. 5.40) does not significantly influence the flow field. The major influence of the plasma on the flow field is through the heat addition that is shown in Fig. 7.4.a. The thermal power deposition originates in large part from ion Joule heating in the cathode sheath. Large values of the gas heating are observed at the interface between the dielectric and the cathode where the electric fields are the largest.

Gas temperature contours are shown in Fig. 7.4.b. The gas temperature peaks in an annular region near the cathode, while the peak in gas temperature occurred at the centerline in results from the preliminary studies on micronozzle flows (Sec. 4.3.3). The offset from the centerline is due to the ion Joule heating source term located primarily in the cathode sheath (see Fig. 7.4.a), while the source term was imposed in the center of the nozzle for the preliminary studies on micronozzle flows. Due to the advective flow, the heated gas is transported downstream, past the exit plane. The net power deposition into neutral gas (integrated over the entire domain) is 140 mW. The peak temperature (950 K) is less the peak temperature observed in the preliminary studies of microthrusters for a power deposition of 140

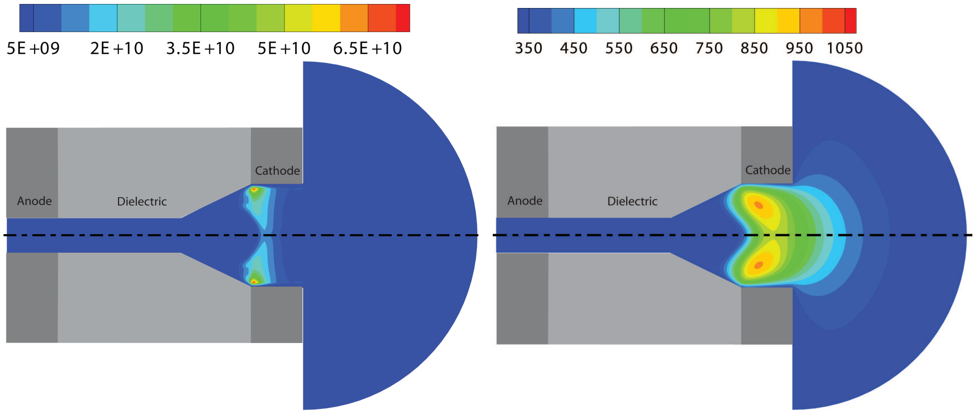

(a) Power deposition (W/m^3)   (b) Gas temperature (K)

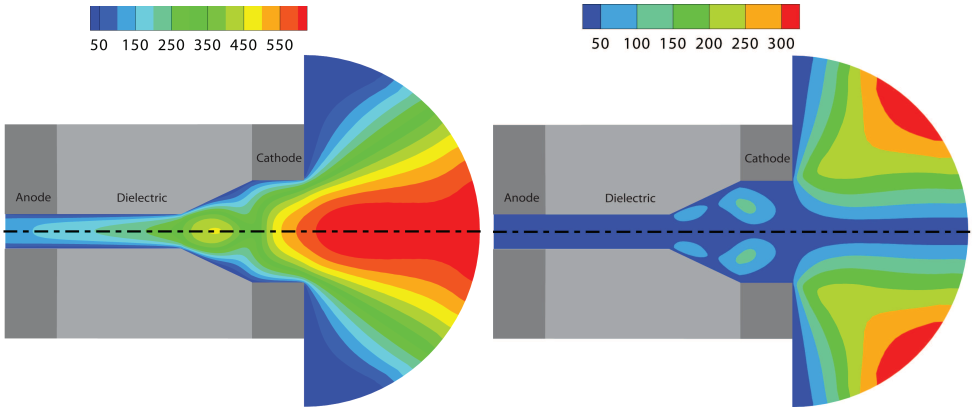

(c) Axial velocity (m/s)   (d) Radial velocity (m/s)

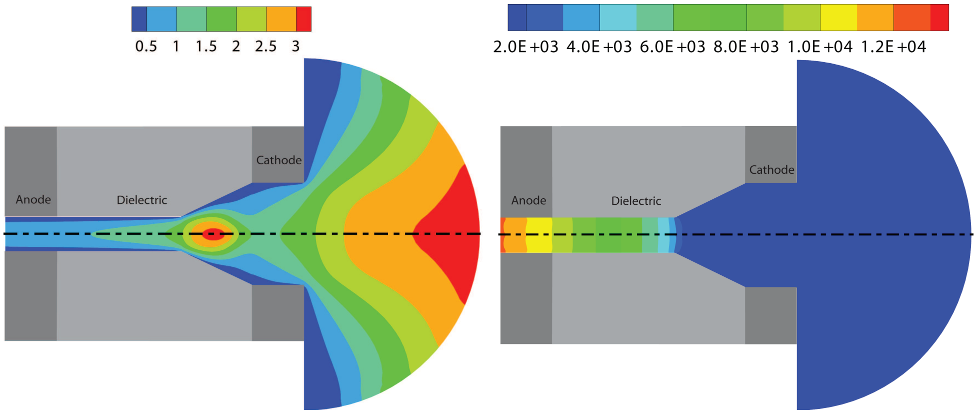

(e) Mach number   (f) Pressure (Pa)

Figure 7.4: Flow properties in the MPT. (The operating conditions are indicated in Fig. 7.2 caption)

mW (1900 K). The reduced gas temperature is due to the distribution field of the heat addition. Power deposition near the cathode leads to increased heat losses to the solid walls. While the gas temperature is fixed at 300 K at the solid-wall boundaries in our model, the temperature of the cathode, as well as of the other solid surfaces, rises significantly in reality. As will be shown Sec. 7.3.1, a higher cathode temperature reduces the heat losses and is beneficial for the thruster performance.

The velocity, Mach number and pressure fields are shown in Figs. 7.4.c to 7.4.f. Compared to the cold gas micronozzle case (see Sec. 4.3.3), the axial velocity increases at the exit plane due to the total enthalpy addition in the expanding section of the nozzle. For these operating conditions, the computed thrust is 100 μN (compared to 67 μN for the cold gas micronozzle case), which corresponds to a specific impulse of 74 s.

Figure 7.5 shows a schematic of the energy flow pathways in the MPT. The electrical power input (the discharge current times the discharge voltage) for the base case is 650 mW. The ion Joule heating, when integrated over the entire domain ($\int_V \vec{J}_{ion} \cdot \vec{E}\, dV$), is about 550 mW, while the electron Joule heating ($\int_V \vec{J}_{e^-} \cdot \vec{E}\, dV$) is about 45 mW. The total Joule heating (595 mW) does not equal to the electrical power input owing to discretization errors in our first order spatial discretization schemes. Clearly, higher order schemes must be pursued in future studies to remedy this discrepancy. Seventy-five percent of the power from the ion Joule heating is lost directly at solid walls, while 25% (α_J in Eq.5.4) is deposited in the heavy species thermal pool, that includes ion and neutral species. The direct deposition of power to solid walls constitutes the dominant energy flow pathway. A small fraction (less than 1%) of the power deposited in the heavy species thermal pool is then lost through inelastic collisions, while the rest is lost at solid walls and at the outflow section. The rate of energy transfer from the electron thermal pool to the heavy species thermal pool through elastic collisions amounts to small fraction of the electron Joule heating (less than 1%). A significant amount of power (35 mW or $\sim$80% of the electron Joule heating) is lost through inelastic collisions, while the

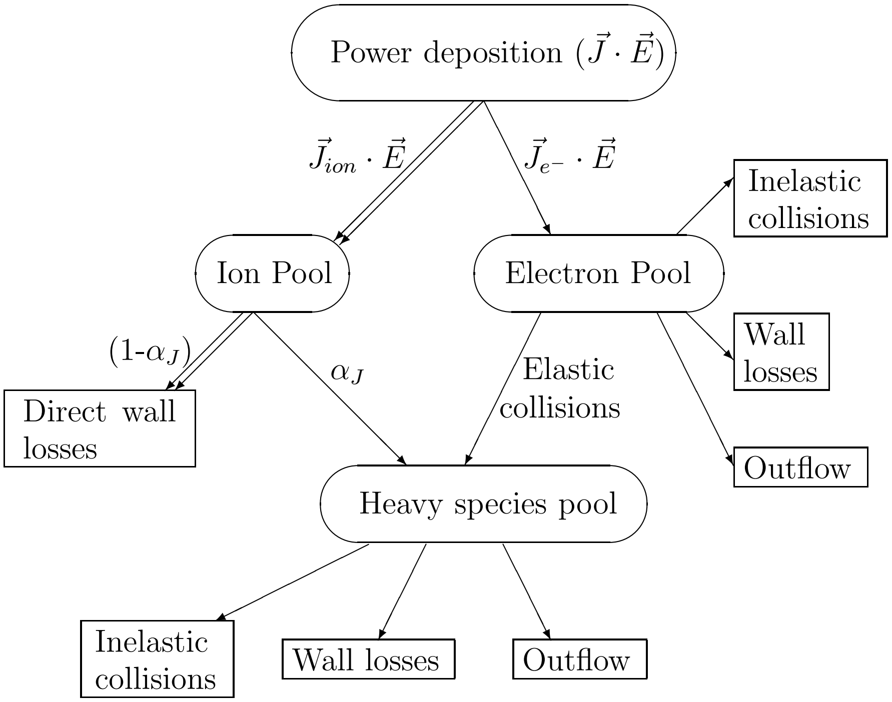

Figure 7.5: Energy flow pathways in the MPT

rest of the power deposited in the electron thermal pool is lost through transport at solid walls and at the outflow section.

7.2.2 Effect of power input

Figure 7.6 shows the effects of power input on discharge characteristics. Results are presented for case A1 (where the discharge voltage is fixed at 750 V) and for case A3 (where the discharge voltage is fixed at 1000 V). For both cases, the inlet total pressure is 100 Torr and the flow rate is 5.2 sccm. The plasma is more intense (i. e. the ionized species number densities are higher) for higher power inputs. Electron and Ar^+ number densities increase by a factor of $\sim$2 as the power input is increased from 650 mW (for case A1) to 1800 mW (for case A3).

Figure 7.7 shows the effect of power input on flow properties. Contours of the power deposition in the MPT are shown in Fig. 7.7.i. The net power deposition

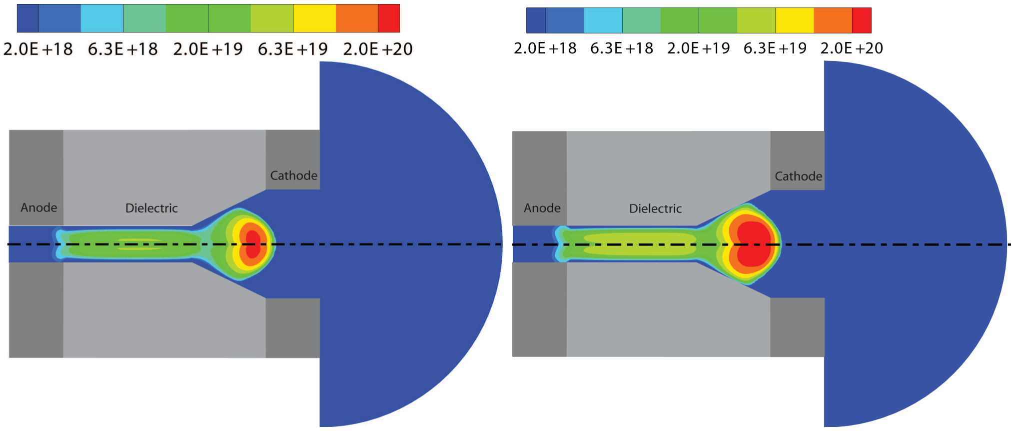

(i) Electron number density (#/m^3)

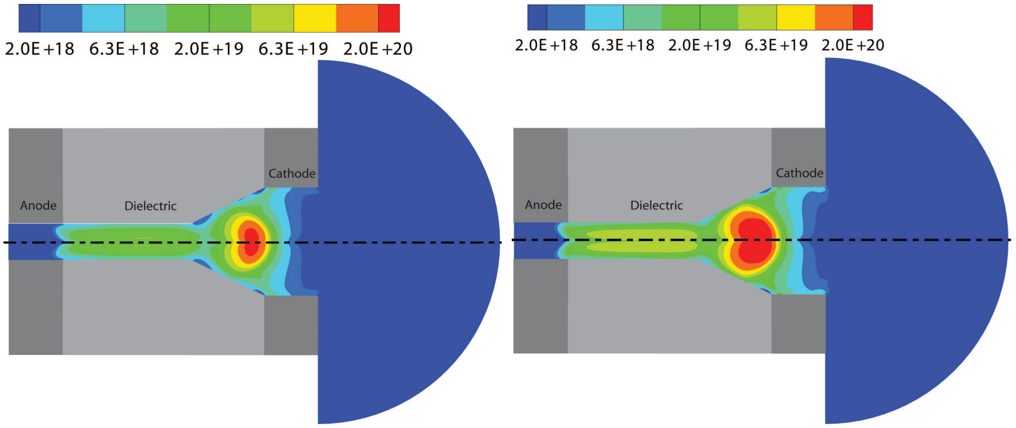

(ii) Ar^+ number density (#/m^3)

(a) Power input: 650 mW (case A1)

(b) Power input: 1800 mW (case A3)

Figure 7.6: Electron and ion (Ar^+) number density contours for different values of the power input. The inlet total pressure is 13300 Pa (100 Torr) and the flow rate is 5.2 sccm for both cases.

into neutral gas scales almost linearly with the power input as the ratio between theses two quantities remains equal to about 20% for both cases. Gas temperatures contours are shown in Fig. 7.7.ii. A peak temperature of 1850 K is reached for the high power case (compared to 950 K for the base case). Importantly, these results show that changing the external power input is an effective method to control the level of gas heating in the discharge, which, in turn, affects the gas temperature and the thrust value of the device. This constitutes a key feature of our proposed MPT concept. The computed thrust increases to a value of 128 μN for the high power case, which corresponds to a specific impulse of 95 s.

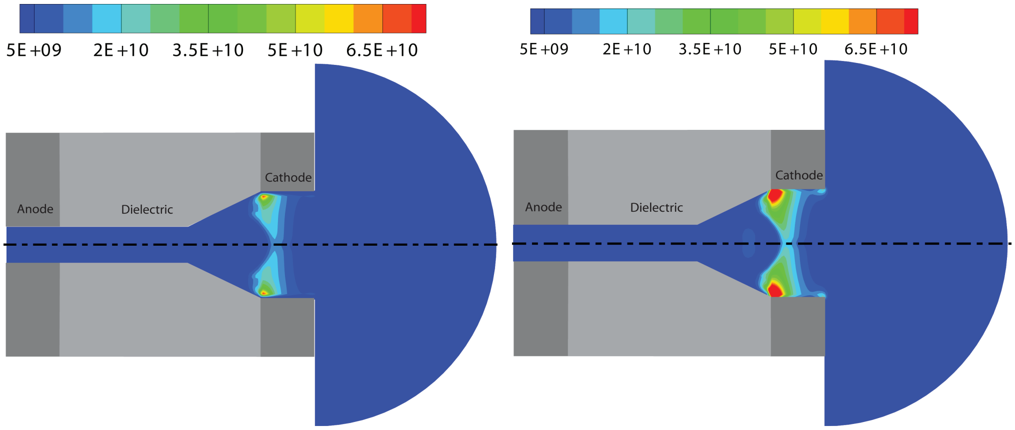

(i) Power deposition (W/m^3)

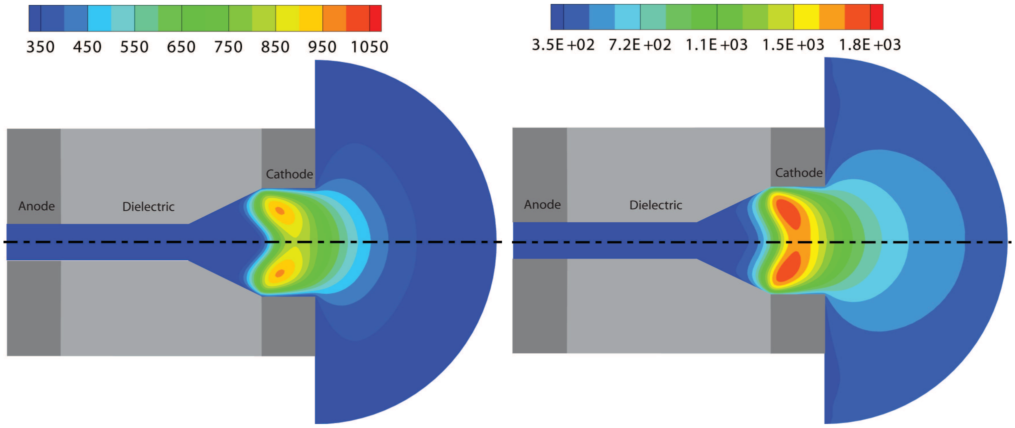

(ii) Gas temperature (K)

(a) Power input: 650 mW (case A1)

(b) Power input: 1800 mW (case A3)

Figure 7.7: Power deposition and gas temperature contours for different values of the power input. The inlet total pressure is 13300 Pa (100 Torr) and the flow rate is 5.2 sccm for both cases.

7.3 Sensitivity to model parameters

In this section, sensitivity of results to model parameters is discussed. All sensitivity studies are performed by using the same nominal (base) case operating conditions (A1), while varying uncertain model parameters. These parameters are the cathode temperature, the fraction of ion Joule heating that is locally converted to gas thermal energy, and the secondary electron coefficient. For all the cases, the inlet total pressure is 100 Torr, the flow rate is 5.2 sccm, and the discharge voltage is 750 V.

7.3.1 Cathode temperature

An accurate estimate of the cathode temperature would require solving an energy balance equation for the entire MPT device (including solid materials). In this study, we have approximated the solid surfaces as isothermal and the temperature at those surfaces (including the cathode) has been fixed to 300 K for all previously shown results.

The effect of the cathode temperature on the MPT performance is studied by comparing the base case solution (where the cathode temperature is fixed at 300 K) with a case where the cathode temperature is fixed at 1000 K. Figure 7.8.i plots gas temperature contours for the two cases. The spatial distribution of gas temperature appears strongly dependent on the cathode temperature. For the case where the cathode temperature is fixed at 1000 K, the peak gas temperature reaches 1150 K (compared to 950 K for the base case) and the region of high gas temperatures occupies a larger part of the MPT than for the base case. Increasing the cathode temperature reduces the temperature gradients at the cathode surface, thereby decreasing the net thermal loss.

The axial velocity contours are shown for the two cases in Fig 7.8.ii. As the cathode temperature is increased, the reduced heat losses allow for a further expansion of the gas in the diverging section of the micronozzle. The computed thrust therefore increases from a value of 100 μN for the base case to a value of

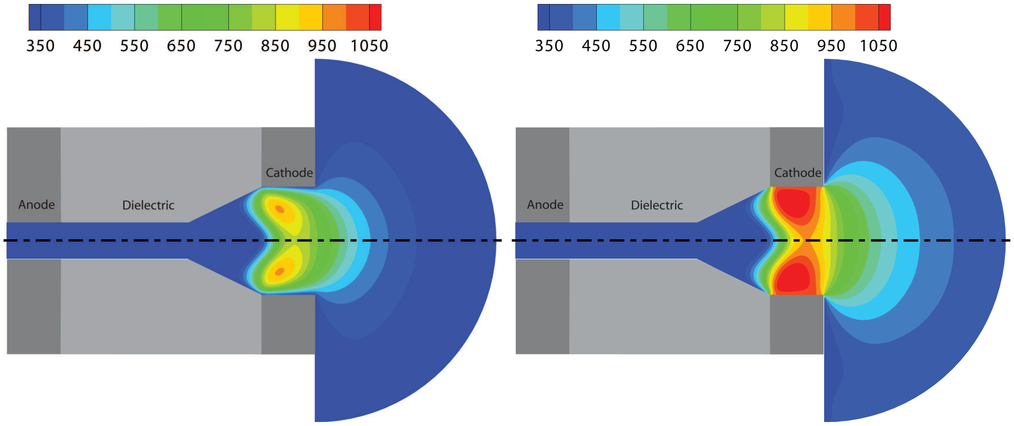

(i) Gas temperature (K)

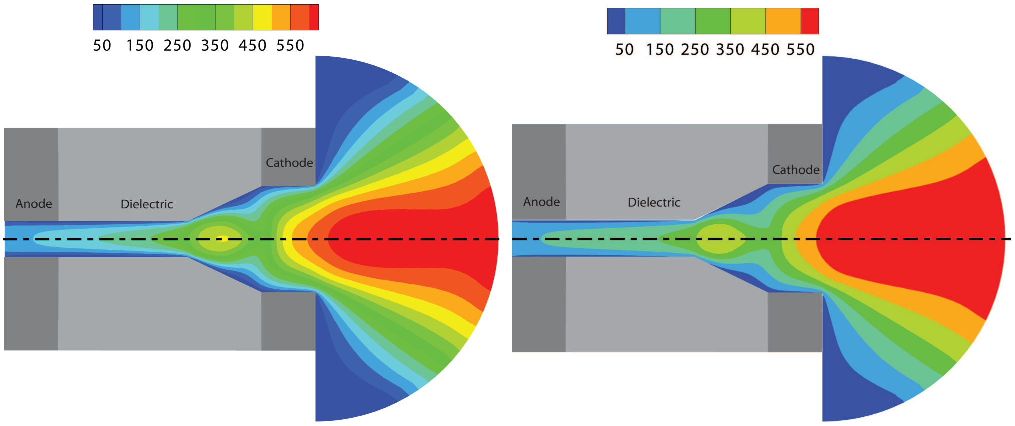

(ii) Axial velocity (m/s)

(a) Cathode temperature: 300 K (b) Cathode temperature: 1000 K

Figure 7.8: Gas temperature and axial velocity contours for different values of the the imposed temperature at the cathode. The flow rate is 5.2 sccm and the applied potential difference between the electrodes is 750 V.

112 μN for the case where the cathode temperature is fixed at 1000 K. It should be noted that, for this last case, the power input has decreased to a value of 540 mW, compared to 650 mW for the base case. The higher gas temperatures (and therefore lower background Ar densities) result in a decrease in ionization. The lower power/current can be attributed to the lower charge densities and hence to the lower plasma conductivity.

In reality, the cathode temperature probably reaches temperatures even larger than 1000 K, since damage of the molybdenum cathode surfaces of the MPT has been observed experimentally [15]. These results emphasize the importance of managing thermal loads on the cathode by using materials that can withstand high temperatures and the importance of limiting the heat transfer to the cathode to increase the efficiency of the MPT.

7.3.2 Fraction of ion Joule energy thermalized with the gas

A large fraction of the kinetic energy of the ions is deposited directly on the cathode, rather than to the background gas. This phenomena has been simulated by Revel *et al* [84], who report a one-dimensional study for an argon discharge in which the gas heating source terms are calculated using a Monte Carlo model. For current densities of ~20 A/m^2, an interelectrode distance of 1.5 cm, and a background pressure of 1 Torr, they observe that ~25% of the ion Joule energy is converted to gas thermal energy, with the remainder being transferred directly to the cathode. Boeuf *et al* used a nominal fixed value of $\alpha_J = 0.25$ for simulation studies of a 100 Torr xenon MHCD, which is the same value we chose to use for our base case.

The sensitivity of model results to the fraction of ion joule energy thermalized with the gas is investigated by comparing the base case solution with a case where $\alpha_J = 0.5$. The power deposition and gas temperatures contours are shown in Fig. 7.9 for both cases. Since most of the power deposition comes from the ion Joule heating, the net power deposition into neutral gas increases significantly from a value of 140 mW for the base case to 260 mW when $\alpha_J = 0.5$. At the same time, the input power of the MPT decreased to 540 mW (compared to 650 mW for the base case). As in the previous section, the increase of the gas temperature (to a peak value of 1350 K) can be invoked to justify the decrease in ionization and hence the decrease of the current/power value. The increased power deposition into neutral gas improves the efficiency of the device and increases the computed thrust to 116 μN (compared to 100 μN for the base case).

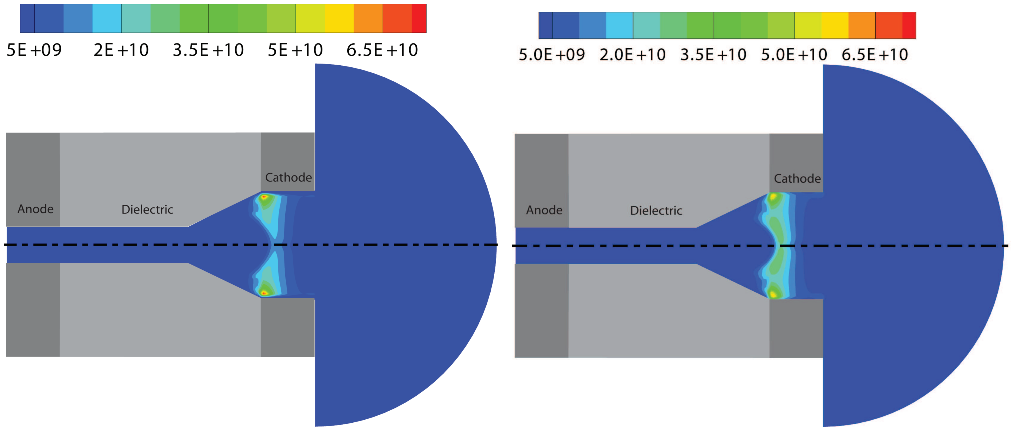

(i) Power deposition (W/m^3)

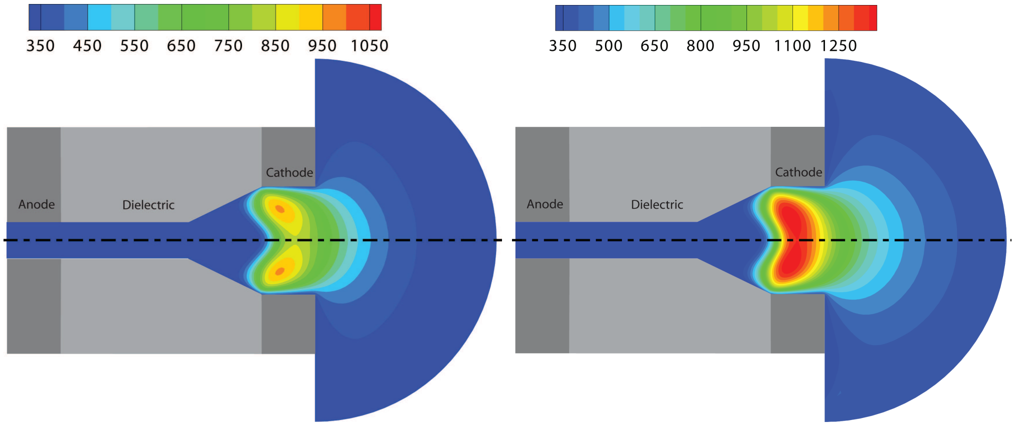

(ii) Gas temperature (K)

(a) $\alpha_J = 0.25$

(b) $\alpha_J = 0.5$

Figure 7.9: Power deposition and gas temperature contours for different fractions of ion Joule energy converted to gas thermal energy. The flow rate is 5.2 sccm and the applied potential difference between the electrodes is 750 V.

While our model assumes a constant value for the fraction of ion Joule energy thermalized with the gas, this fraction will depend on the local background pressure. Indeed, as the mean free path of ions decreases with increasing pressure, ions will deposit a larger fraction of their kinetic energy to the background gas. Future work must explore more accurate strategies (e.g. hybrid models) to determine the fraction of ion Joule energy thermalized with the gas.

7.3.3 Secondary electron coefficient

The value of the secondary electron emission coefficient constitutes an important uncertain parameter of the plasma module. This coefficient is sensitive to surface conditions and its value can vary by several orders of magnitude depending on the surface considered. While the value of the reduced electric field stays in the 10^3 - 10^4 Td range for the MHCD studies, the reduced electric field is of the order of 10^5 Td at the cathode surface for the MPT studies. A variable secondary emission coefficient model of the same type we used for the MHCD studies could not be found in the literature for these large values of the reduced electric field. In the previously shown MPT results, we chose to use a constant value for this coefficient equal to 0.03, corresponding to a nickel surface interacting with an argon plasma as suggested in [3]. The sensitivity of our results to this parameter is analyzed by comparing our base case with a case where $\gamma_{eff} = 0.01$. The discharge current is significantly reduced for the model with the lower secondary electron coefficient (to a value of 0.33 mA) since, for this last case, fewer electrons per ion impact are released from the cathode. These results are consistent with previous studies on microdischarges [50, 85].

Figure 7.10 shows the ion number density and gas temperature contours obtained with the two models for a discharge voltage of 750 V. While the peak ion number density has about the same value ($\sim 3\times10^{20}$ $\#/\text{m}^3$) for both cases, the discharge activity appears more constricted for the lower γ_{eff} case. Since the ion Joule heating scales with the current, a significant decrease in power deposition into the neutral gas is observed (not shown). This results in a decrease of the gas temperature (shown in Figure 7.10.ii) and a decrease of the computed thrust to a value of 87 μN, compared to 100 μN for the base case.

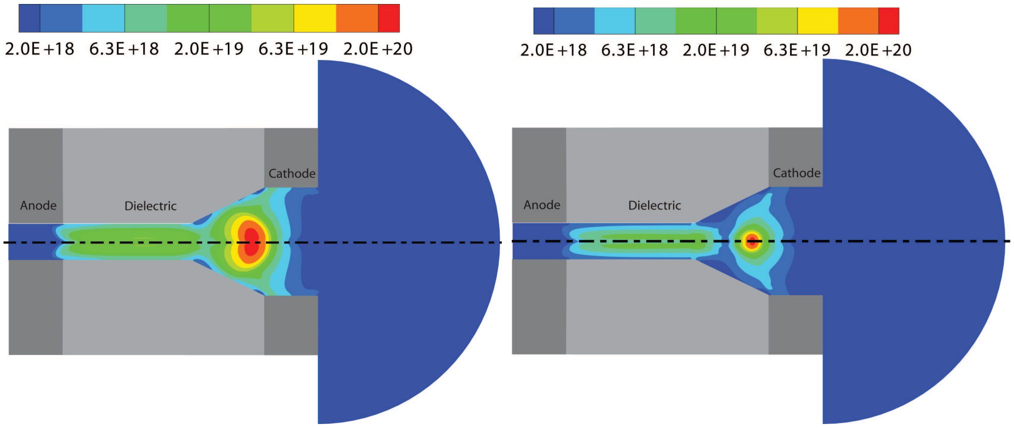

(i) Ar^+ number density (#/m^3)

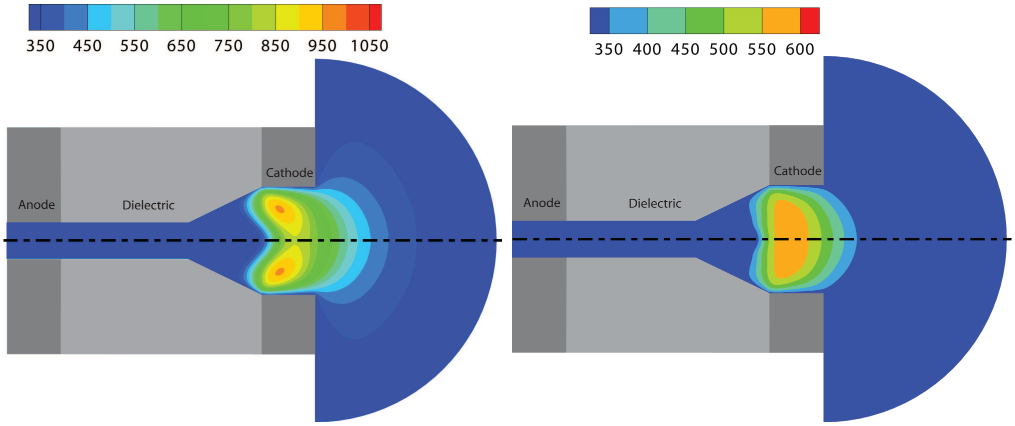

(ii) Gas temperature (K)

(a) $\gamma_{eff} = 0.03$ (b) $\gamma_{eff} = 0.01$

Figure 7.10: Ion number density and gas temperature contours for different values of the secondary electron emission coefficient. The flow rate is 5.2 sccm and the applied potential difference between the electrodes is 750 V.

7.4 Summary

The Micro Plasma Thruster (MPT) concept consists of a direct-current microdischarge in a geometry comprising a constant area flow section followed by a diverging exit nozzle. A self-consistent model comprising a plasma module and a flow module is used to study the MPT and to understand the plasma-flow interactions inside the micronozzle. The coupled plasma-flow simulations show that the electrostatic component of thrust is negligible for our current MPT configuration. Electrothermal heating is primarily due to the ion Joule heating occurring near the cathode surfaces. A large part of the input power is therefore deposited into the walls rather than to neutral gas heating. Future work must explore strategies that will allow for power deposition away from the wall, near the centerline.

For a discharge voltage of 750 V, a power input of 650 mW, and an argon mass flow rate of 5.2 sccm, the specific impulse of the device is 74 s, a factor of $\sim$1.5 increase compared to the cold gas micronozzle. For these conditions, charged species densities on the order of 5×10^{20} m^{-3} and peak gas temperatures of $\sim$1000 K are predicted. The microdischarge remains mostly confined inside the micronozzle and operates in an abnormal regime. Additional simulation studies on the MPT indicate that the power input has a strong influence on overall discharge properties. The net power deposition into the neutral gas scales with the power input, providing a method of controlling the gas temperature and the thrust level of the MPT. This feature constitutes an important advantage over traditional cold gas thrusters.

The sensitivity of our results to important uncertain parameters of the model has been studied. These parameters are the cathode temperature, the fraction of ion Joule heating that is locally converted to gas thermal energy, and the secondary electron coefficient. Our model would significantly benefit from more accurate estimates of these parameters. A higher cathode temperature is found to reduce the heat losses at solid walls and is beneficial for the thruster performance, which emphasizes the importance of managing the thermal load on the cathode. Since most of the power deposition comes from ion Joule heating, the net power deposition into the neutral gas scales with the fraction of ion Joule energy thermalized with the gas. Finally, the voltage-current characteristics of the device is found to be very sensitive to the value of the secondary electron coefficient used in the model.

Chapter 8

Conclusions and recommendations

Microdischarge and flow interaction phenomena for micropropulsion applications have been studied using a detailed self-consistent computational model. The model consists of a plasma module coupled to a flow module and is solved on a hybrid unstructured mesh framework. The plasma module provides a self-consistent, multi-species, multi-temperature description of the microdischarge phenomena while the flow module provides a description of the low Reynolds number compressible flow through the micropropulsion system.

An effective approach to numerical discretization of the Joule heating source term for fluid models of plasma discharge phenomena has been presented. The method, which we called the "Reconstruction-Flux" discretization, has been developed for a cell-centered finite volume scheme of the gas discharge governing equations on unstructured meshes. In this method, the Joule heating term is computed by evaluating the dot product of the electric field and the species flux at the cell center. The species flux at the cell center is reconstructed based on the normal projection of the species fluxes enclosing the cell. The method was validated by simulating a one-dimensional argon glow discharge on different meshes. The "Reconstruction-Flux" discretization approach is found to be a robust and accurate method on structured and unstructured meshes. This method, combined with the Scharfetter-Gummel exponential face flux discretization scheme, produces reasonably accurate results even on coarse meshes.

For the presented results, the Scharfetter-Gummel scheme reduces to a first-order upwind scheme in the cathode sheath because of the large value of the Peclet number at this location. Future studies should explore higher order methods to improve the accuracy of the plasma solver. The "Reconstruction-Flux" discretization scheme could become second order accurate if higher order methods are pursued for the evaluation of the fluxes at the face centers and for the potential gradient reconstructed at the cell center. The computational cost associated with solving the linear system of each governing equation will significantly increase if the higher order fluxes are evaluated implicitly. With the deferred correction approach, the higher order flux could be evaluated explicitly, while the Scharfetter-Gummel scheme could still be used implicitly for the initial estimate of the fluxes to maintain the stability of the numerical scheme.

A prototypical microhollow cathode discharge (MHCD) has been studied to guide and validate the plasma modeling effort. Several operating regimes of the MHCD have been observed. At low currents ($< \sim 0.1$ mA), our model predicts the discharge is constricted within the hollow in agreement with experiments [16, 34]. For larger currents ($> \sim 0.3$ mA), a significant part of the discharge volume lies outside the hollow structure, with the plasma occupying a region of a few hollow diameters above the flat cathode surface plane. In this regime, the discharge operates as a normal glow; an observation that is again confirmed by experimental data available in the literature. Our model includes a surface-normal electric-field dependent electron secondary emission coefficient which allows the model to capture the three operating regimes. Charged species densities of the order of 10^{19} m^{-3} are predicted for the conditions investigated. Electron temperatures on the order of 15 eV in the cathode sheath and of the order of 1 eV in the bulk plasma are predicted. Gas heating is significant particularly for the higher-current normal regime where gas temperatures of up to 200 K above room temperature were predicted; again consistent with experimental data [53].

Oscillations in the numerical solutions were observed for intermediate discharge currents ranging from ∼0.1 mA to ∼0.3 mA. These oscillations present some similarities with the self-pulsing regime reported experimentally by [16] which was also observed to occur at intermediate currents between the constricted and normal regime. The frequency of the oscillations increases with the averaged current as for the experimentally observed pulsing. However, some important discrepancies concerning the shape and the frequency of the oscillations still need to be reconciled.

The Micro Plasma Thruster (MPT) concept consists of a direct-current microdischarge in a geometry comprising a constant area flow section followed by a diverging exit nozzle. Preliminary studies on the MPT showed that by heating the flow in the diverging section of the micronozzle, a significant increase in specific impulse (compared to conventional cold gas thrusters) is obtained. The coupled plasma-flow simulations showed that the electrostatic component of thrust is negligible for our current MPT configuration. Electrothermal heating is due primarily from the ion Joule heating occurring near the cathode surfaces. A large part of the input power is therefore deposited into the walls rather than going to neutral gas heating. Future work must explore strategies that will allow for power deposition away from the wall, near the centerline. For example, radio-frequency operation of the microdischarge may help reduce the thermal load on the microdischarge, and increase the direct power deposition into the neutral gas.

For a discharge voltage of 750 V, a power input of 650 mW, and an argon mass flow rate of 5.2 sccm, the specific impulse of the device is 74 s, a factor of ∼1.5 increase compared to the cold gas micronozzle. For these conditions, charged species densities on the order of 5×10^{20} m^{-3} and peak gas temperatures of ∼1000 K are predicted. The microdischarge remains mostly confined inside the micronozzle and operates in an abnormal regime. Additional simulation studies on the MPT indicate that the power input has a strong influence on overall discharge properties.

The net power deposition into the neutral gas scales with the power input, providing a method of controlling the gas temperature and the thrust level of the MPT. This feature constitutes an important advantage over traditional cold gas thrusters.

The sensitivity of our results to important uncertain parameters of the model has been studied. These parameters are the cathode temperature, the fraction of ion Joule heating that is locally converted to gas thermal energy, and the secondary electron coefficient. Our model would significantly benefit from more accurate estimates of these parameters. A higher cathode temperature is found to reduce the heat losses at solid walls and is beneficial for the thruster performance, though there is obviously an upper limit to avoid damaging the cathode. Since most of the power deposition comes from ion Joule heating, the net power deposition into the neutral gas scales with the fraction of ion Joule energy thermalized with the gas. Finally, the voltage-current characteristics of the device is found to be very sensitive to the value of the secondary electron coefficient used in the model.

The cathode temperature could be evaluated by solving the solid thermal conduction equation in the dielectric and electrode material to quantify the overall thermal field in the MPT device. The thermal loads from the plasma at the wall surfaces will drive heat transfer into the device structure potentially resulting in "hot spots" that can be investigated through the simulations. These coupled "multi-physics" simulation results would in turn provide an informed approach to the better designs of the MPT device from a thermal viewpoint. A hybrid model could be used to simulate the ionized species in the cathode sheath. This would allow for a self-consistent modeling of the ion and electron Joule heating that is locally converted to thermal energy. Finally, future studies of the MPT should include a calibration and a validation of the model with experimental results.

Appendix A

Validation with analytical solutions

A.1 One-dimensional diffusion solutions

We consider the species continuity equation (Eqn. 5.1) where the bulk flow velocity is zero,

$$\frac{\partial n_k}{\partial t} + \vec{\nabla} \cdot \vec{\Gamma}_k = \dot{G}_k. \tag{A.1}$$

As shown in [3], at steady state for a 1D slab geometry (extending from $x = 0$ to $x = l$) where transport processes are dominated by diffusion, Eqn. A.1 reduces to,

$$-D_k \frac{d^2 n_k}{dx^2} = \dot{G}_k. \tag{A.2}$$

Let us assume a source term ($\dot{G}_k$) of the form,

$$\dot{G}_k = n_k n_{k_b} K_{iz,k}. \tag{A.3}$$

We have $\nu_{iz,k} = n_{k_b} K_{iz,k}$, where the subscript k refers to one of the charged species, $\nu_{iz,k}$ is the ionization frequency, n_{k_b} is the background species density, and $K_{iz,k}$ is the ionization rate. For constant D_k and $\nu_{iz,k}$, and boundary conditions $n_{0,k} =$

$n_{l,k} = 0$, Eqn. A.2 admits an analytical solution of the form,

$$n_k = n_{max,k}\sin(\beta_k x). \tag{A.4}$$

This problem is an eigenvalue problem since the ionization frequency, the diffusion coefficient and the length of the domain are related as follows,

$$\sqrt{\frac{\nu_{iz,k}}{D_k}} = \frac{\pi}{l}(= \beta_k). \tag{A.5}$$

The above analytical solution is now applied to a quasi-neutral, 3-species plasma (electrons, ions, and background species). The notion of an ambipolar diffusion coefficient can be used to capture the drift and diffusion phenomena in the discharge. The ambipolar diffusion coefficient is given by,

$$D_a = \frac{\mu_i D_e + \mu_e D_i}{\mu_i + \mu_e}, \tag{A.6}$$

where the subscripts i and e stand for ions and electrons respectively. The species transport properties are given by,

$$D_k = \frac{k_B T_k}{m_k \bar{\nu}_{k,k_b}}, \tag{A.7}$$

$$\mu_k = \frac{e Z_k D_k}{k_B T_k}. \tag{A.8}$$

The collision frequency between plasma species k and the background species k_b is evaluated as

$$\bar{\nu}_{k,k_b} = n_{k_b} \bar{\bar{\sigma}}_{k,k_b} \bar{g}_k, \tag{A.9}$$

where $\bar{\bar{\sigma}}_{k,k_b}$ is an approximate hard-sphere momentum transfer collision cross-section for the species k colliding with the background species k_b, and $\bar{g}_k$ is the average relative molecular speed of species k, given by

$$g_k = \sqrt{\frac{8 k_B T_k}{\pi m_{k,r}}}, \tag{A.10}$$

where $m_{k,r} = \frac{m_k \times m_{k_b}}{m_k + m_{k_b}}$ is the reduced mass of species k. A simple helium plasma with 3 species (electrons, helium ions, and background helium atoms) is considered. The experimentally derived cross-sections for electrons and ions with background helium are respectively 9 $\mathring{A}^2$ and 43 $\mathring{A}^2$ [86]. A single ionization reaction whose rate is given by $K_{iz} = 2.584 \times 10^{-12} T_e^{0.68} \exp(-\frac{2.854 \times 10^5}{T_e})$ is considered [47]. The pressure is 50 mTorr, hence the background helium atom density is 1.608×10^{21} m^{-3} (for a gas temperature of 300 K). The width l is taken to be 4 cm, so that Eqn. A.5 gives an analytical value of $\beta_k = 78.54$. With these given parameters, one can compute an analytical value of the electron temperature through Eqn. A.5. For the discharge conditions mentioned above, the obtained value is $T_{e,analytic} = 13$ eV.

It should be noted that, in the numerical problem, we can not impose an electron temperature and only solve the continuity equation (Eq. A.1). By doing so, the number density of the ionized species grows indefinitely if the imposed electron temperature is larger than the analytical value or decays to zero if it is lower than the analytical value. In order to stabilize the numerics, we need to also solve the electron energy equation. In this equation, we include an external power source to heat the electrons. Because of the relatively low pressure (and hence the high electron thermal conductivity), the heating results in a nearly uniform electron temperature over the domain. Starting from arbitrary initial conditions, the species continuity and electron energy equations are solved until a steady sate is reached. The grid is comprised of 250 uniform and aligned cells, which provides adequate spatial resolution for this problem. The analytical value of the electron temperature is imposed as boundary condition on both sides of the domain and the electrostatic potential is grounded at the boundaries. For the species continuity equation, a flux comprised of the drift due to the electric field and the Maxwellian flux is imposed at the boundaries.

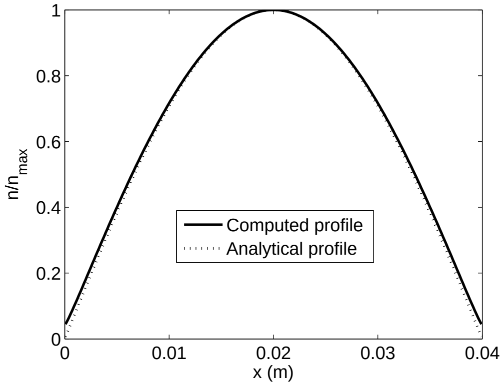

Figure A.1: Comparison between computed number density profile (solid line) and analytical profile (dashed line) from Eqn. A.4. Pressure is 50 mTorr, and external power input is 10^6 W/m^3

.

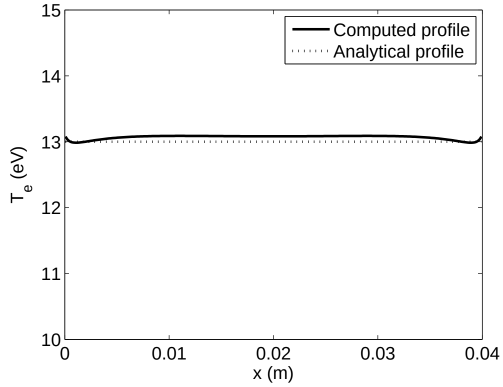

Figure A.2: Comparison between computed electron temperature profile (solid line) and analytical profile (dashed line). Pressure is 50 mTorr, and external power input is 10^6 W/m^3

.

Our simulation results are now compared with the analytical solutions. Fig. A.1 shows the computed plasma number density profile, and the analytical solution (Eqn. A.4). Fig. A.2 shows the comparison between computed and theoretical values of the electron temperature. The computed profiles in the plasma are in good agreement with the analytical solution. The difference between the analytical result and the computed result arises because the analytical solution makes certain simplifying assumptions in the derivation (e.g., simple boundary conditions at the walls), whereas the numerical simulation makes no such assumptions.

A.2 Self-similar solutions

In this section, we consider an argon direct-current discharge between two electrodes which we model with the one-dimensional version of our code. The simplified argon plasma comprises three species: electrons (e), atomic argon ions (Ar^+), and the background argon atoms (Ar). The only reaction considered is electron impact ionization ($e + Ar \rightarrow 2e + Ar^+$). An independent solution of the zero-dimensional electron Boltzmann equation (”BOLSIG+” [69]) provides electron transport properties tabulated as a function of the electron temperature. The ion transport properties are derived from experimental mobility data [86]. A nonuniform mesh comprised of 60 aligned cells is used. Grid clustering near cathode provides adequate resolution of the cathodic sheath area. A constant gas temperature of 300 K is assumed. The right boundary represents the cathode which is grounded, while a 250-volt potential is imposed at the right boundary (anode). A flux comprised of the drift due to the electric field and the Maxwellian flux is imposed at the boundaries for the species continuity equation. For electrons, secondary emission due to ion bombardment is taken into account at the cathode with a value of the effective secondary emission coefficient (Eqn. 5.18) set at 0.05. Finally, the electron energy flux given by Eqn. 5.21 is imposed at both boundaries.

Two self-similar discharge solutions are presented in this section. The linear dimension and the background pressure in the first discharge are 4 cm and 0.25 Torr, respectively. For the second discharge, the linear dimension has been divided by 100 (0.4 mm), while the pressure has been multiplied by 100 (25 Torr). The product PD equals 1 Torr-cm for both discharges. Since gas heating is not considered and since the process of ionization by single collision follows the similarity rules, the two discharges should be perfectly similar [2].

The number densities of the ionized species are shown in Fig. A.3 for the two discharges. In the second discharge, the number density of the charged species is multiplied by 100^2 in accordance with the similarity rules [2]. For both discharges, the extent of the cathode sheath (where the plasma is not quasi-neutral) represents the same fraction of the total discharge length. The potential and the electron temperature profiles (not shown) are exactly the same for both discharges.

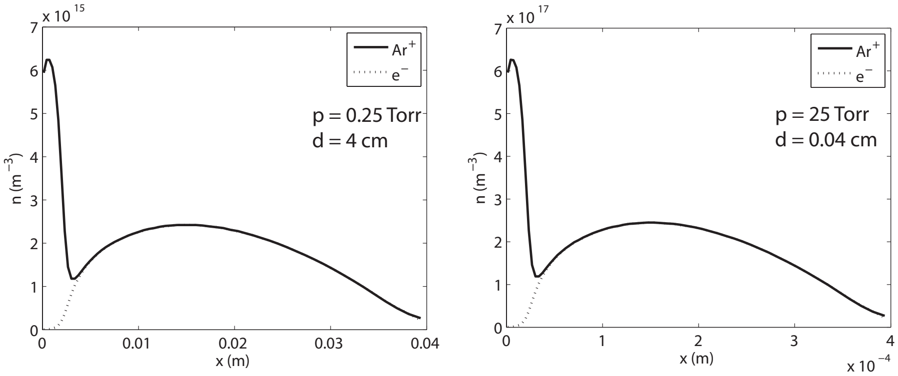

Figure A.3: Number density of argon ions (solid line) and electrons (dashed line) for two similar discharges. The discharge voltage is 250 V and the gas temperature is fixed at 300 K for both cases

.

Bibliography

[1] M. Mitchner and C. H. Kruger. *Partially Ionized Gases.* Wiley, 1973.

[2] A. von Engel. *Ionized Gases.* Springer, 1994.

[3] M. A. Lieberman and A. J. Lichtenberg. *Principles of Plasma Discharges and Materials Processing.* John Wiley & Sons, 1994.

[4] M. J. Druyvesteyn and F. M. Penning. The mechanism of electrical discharges in gases of low pressure. *Reviews of Modern Physics*, 12:87–174, 1940.

[5] Y. P. Raizer. *Gas Discharge Physics.* Springer, 1997.

[6] A. Bogaerts. The glow discharge: an exciting plasma! *Journal of Analytical Atomic Spectrometry*, 14:1375–1384, 1999.

[7] A. Bengtson. Glow discharge mass spectrometry: a current assessment. *Journal of Analytical Atomic Spectrometry*, 11:867–872, 1988.

[8] D. B. Graves. Plasma processing. *IEEE Transactions on Plasma Sciences*, 22:31–42, 1994.

[9] I. G. Ivanov, E. I. Latush, and M. F. Sem. *Metal Vapour Ion Lasers: Kinetic Processes and Gas Discharges.* Wiley, 1996.

[10] J. F. Waymouth. *Electric Discharges Lamps.* MIT Press, 1971.

[11] R. Foest, M. Schmidt, and K. Becker. Microplasmas, an emerging field of low-temperature plasma science and technology. *International Journal of Mass Spectrometry*, 2006:87–102, 2005.

[12] A. El-Habachi and K. H. Schoenbach. Emission of excimer radiation from direct current, high-pressure hollow cathode discharges. *Applied Physics Letters*, 72:22–24, 1998.

[13] K. Becker, A. Koutsospyros, S.-M. Yin, C. Christodoulatos, N. Abramzon, J. C. Joaquin, and G. Brelles-Mariño. Environmental and biological applications of microplasmas. *Plasma Physics and Controlled Fusion*, 47:B513–B523, 2005.

[14] M. Miclea, K. Kunze, U. Heitmann, S. Florek, J. Franzke, and K. Niemax. Diagnostics and application of the microhollow cathode discharge as an analytical plasma. *Journal of Physics D: Applied Physics*, 38:1709–1715, 2005.

[15] U. KC, J. Bingaman, P. L. Varghese, and L. L. Raja. Studies of a direct-current microdischarge based miniaturized plasma thruster. In *Proceedings of the 2nd European Conference for Aerospace Sciences*, Brussels, Belgium, 2007.

[16] X. Aubert, G. Bauville, J. Guillon, B. Lacour, V. Puech, and A. Rousseau. Analysis of the self-pulsing operating mode of a microdischarge. *Plasma Sources Science and Technology*, 16:23–32, 2007.

[17] D. L. Bitzer and H. G. Slottow. The plasma display panel - a digitally addressable display with inherent memory. *AFIPS Conference Proceedings*, 29:541–547, 1966.

[18] G. F. Weston. Plasma panel displays. *Journal of Physics E: Scientific Instruments*, 8:981–991, 1975.

[19] H. G. Slottow. Plasma displays. *IEEE Transactions on Electron Devices*, 23:760–772, 1976.

[20] A. Sobel. Plasma displays. *IEEE Transactions on Plasma Science*, 19:1032–1047, 1991.

[21] K. H. Becker, K. H. Schoenbach, and J. G. Eden. Microplasmas and applications. *Journal of Physics D: Applied Physics*, 39:R55–R70, 2006.

[22] Q. Wang, I. Koleva, V. M. Donnelly, and D. J. Economou. Spatially resolved diagnostics of an atmospheric pressure direct current helium microplasma. *Journal of Physics D: Applied Physics*, 38:1690–1697, 2005.

[23] F. Adler, E. Davliatchine, and E. Kindel. Comprehensive parameter study of a micro-hollow cathode discharge containing xenon. *Journal of Physics D: Applied Physics*, 35:2291–2297, 2002.

[24] I. Petzenhauser, L. D. Biborosch, U. Ernst, K. Frank, and K. H. Schoenbach. Comparison between the ultraviolet emission from pulsed microhollow cathode discharges in xenon and argon. *Applied Physics Letters*, 83:4279–4450, 2003.

[25] M. Moselhy, I. Petzenhauser, K. Frank, and K. H. Schoenbach. Excimer emission from microhollow cathode argon discharges. *Journal of Physics D: Applied Physics*, 36:2922–2927, 2003.

[26] F. Iza and J. A. Hopwood. Low-power microwave plasma source based on a microstrip split-ring resonator. *IEEE Transactions on Plasma Science*, 31:782–787, 2003.

[27] N. P. Ostrom, B. A. Vojak, and J. G. Eden. Radio frequency (10-23 MHz)-assisted excitation of a microdischarge with a piezoelectric transformer. *Plasma Sources Science and Technology*, 13:278–281, 2004.

[28] P. von Allmen, S. T. McCain, N. P. Ostrom, B. A. Vojak, J. G. Eden, F. Zenhausern, C. Jensen, and M. Oliver. Ceramic microdischarge arrays with individually ballasted pixels. *Applied Physics Letters*, 82:2562–2564, 2003.

[29] S.-J. Park, J. G. Eden, J. Chen, and C. Liu. Microdischarge devices with 10 or 30 μm square silicon cathode cavities: pd scaling and production of the XeO excimer. *Applied Physics Letters*, 85:4869–4871, 2004.

[30] N. P. Ostrom and J. G. Eden. Microcavity plasma photodetectors: Photosensitivity, dynamic range, and the plasma-semiconductor interface. *Applied Physics Letters*, 87:141101, 2005.

[31] K. H. Schoenbach, R. Verhappen, T. Tessnow, F. E. Peterkin, and W. W. Byszewski. Microhollow cathode discharges. *Applied Physics Letters*, 68:13–15, 1996.

[32] D. D. Hsu and D. B. Graves. Microhollow cathode discharge reactor chemistry. *Plasma Chemistry and Plasma Processing*, 25:1–17, 2005.

[33] B. N. Sismanoglu and J. Amorim. Microhollow cathode discharge and breakdown in micron separations. *European Physical Journal Applied Physics*, 41:165–172, 2008.

[34] K. H. Schoenbach, A. El-Habachi, W. Shi, and M. Ciocca. High-pressure hollow cathode discharges. *Plasma Sources Sciences and Technology*, 6:468477, 1997.

[35] J.-P. Boeuf, L. C. Pitchford, and K. H. Schoenbach. Predicted properties of microhollow cathode discharges in xenon. *Applied Physics Letters*, 86:071501, 2005.

[36] Z. Lj. Petrović and A. V. Phelps. Oscillations of low-current electrical discharges between parallel-plane electrodes. i. dc discharges. *Physical Review E*, 47:2806 – 2815, 1993.

[37] H. Horisawa and I. Kimura. Very low-power dc plasma-jet microthrusters. In *Proceedings of the 37th AIAA/ASME/SAE/ASEE Joint Propulsion Conference and Exhibit*, AIAA paper 2001-3791, Salt Lake City, UT, 2001.

[38] J. Slough, S. Andreason, T. Ziemba, and J. J. Ewing. Micro-discharge microthruster. In *Proceedings of the 41st AIAA/ASME/SAE/ASEE Joint Propulsion Conference and Exhibit*, AIAA paper 2005-4047, Tucson, AZ, 2005.

[39] J.-P. Boeuf. A two-dimensional model of dc glow discharges. *Journal of Applied Physics*, 63:1342–1349, 1988.

[40] S. T. Surzhikov and J. S. Shang. Two-component plasma model for two-dimensional glow discharge in magnetic field. *Journal of Computational Physics*, 199:437–464, 2004.

[41] G. G. Lister. Low-pressure gas discharge modelling. *Journal of Physics D: Applied Physics*, 25:1649–1680, 1992.

[42] A. V. Phelps. Abnormal glow discharges in Ar: experiments and models. *Plasma Sources Science and Technology*, 10:329–343, 2001.

[43] A. L. Ward. Calculations of cathode-fall characteristics. *Journal of Applied Physics*, 33:2789–2794, 1962.

[44] M. Meyyappan and J. P. Kreskovsky. Glow discharge simulation through solutions to the moments of the boltzmann transport equation. *Journal of Applied Physics*, 68:1506–1512, 1990.

[45] A. Fiala, L. C. Pitchford, and J.-P. Boeuf. Two-dimensional, hybrid model of low-pressure glow discharges. *Physical Review E*, 49:5607–5622, 1994.

[46] C. Punset, S. Candy, and J.-P. Boeuf. Addressing and sustaining in alternating current coplanar plasma display panels. *Journal of Applied Physics*, 86:124–133, 1999.

[47] S. Rauf and M. J. Kushner. Dynamics of a coplanar-electrode plasma display panel cell. I. basic operation. *Journal of Applied Physics*, 85:3460–3469, 1999.

[48] G. J. M. Hagelaar and G. M. W. Kroesen. A monte carlo modelling study of the electrons in the microdischarges in plasma addressed liquid crystal displays. *Plasma Sources Science and Technology*, 9:605–614, 200.

[49] H. C. Kim, M. S. Hur, S. S. Yang, S. W. Shin, and J. K. Lee. Three-dimensional fluid simulation of a plasma display panel cell. *Journal of Applied Physics*, 91:9513–9520, 2002.

[50] M. J. Kushner. Modelling of microdischarge devices: plasma and gas dynamics. *Journal of Physics D: Applied Physics*, 38:1633–1643, 2005.

[51] T. Farouk, B. Farouk, D. Staack, A. Gutsol, and A. Fridman. Simulation of dc atmospheric pressure argon micro glow-discharge. *Plasma Sources Sciences and Technology*, 15:676–688, 2006.

[52] P. S. Kothnur and L. L. Raja. Two-dimensional simulation of a direct-current microhollow cathode discharge. *Journal of Applied Physics*, 97:043305, 2005.

[53] C. Penache, M. Miclea, A. Brauning-Demian, O. Hohn, S. Schossler, T. Jahnke, K. Niemax, , and H. Schmidt-Böcking. Characterization of a high-pressure microdischarge using diode laser atomic absorption spectroscopy. *Plasma Sources Sciences and Technology*, 11:476–483, 2002.

[54] P. S. Kothnur and L. L. Raja. Simulation of direct-current microdischarges for application in electro-thermal class of small satellite propulsion devices. *Contributions to Plasma Physics*, 47:9–18, 2007.

[55] R. A. Arakoni, J. J. Ewing, and M. J. Kushner. Microdischarges for use as microthrusters: modelling and scaling. *Journal of Physics D: Applied Physics*, 41:105208, 2008.

[56] M. M. Micci and A. D. Ketsdever. *Micropropulsion for small spacecraft.* AIAA, 2000.

[57] W. B. Stein, A. A. Alexeenko, and I. Hrbud. RFCCD microthruster performance via numerical simulation. In *Proceedings of the 46th AIAA Aerospace Sciences Meeting and Exhibit*, AIAA paper 2008-962, Reno, NV, 2008.

[58] K. L. Williams, A. B. Eriksson, R. Thorslund, J. Köhler, M. Boman, and L. Stenmark. The electrothermal feasibility of carbon microcoil heaters for cold/hot gas microthrusters. *Journal of Micromechanics and Microengineering*, 16:1154–1161, 2006.

[59] C. Xie. Characteristics of micronozzle gas flows. *Physics of Fluids*, 19:037102, 2007.

[60] M. Caceres. The emerging nanosatellite market. *Aerospace America*, 2001.

[61] J. G. Reichbach, R. J. Sedwick, and M. Martinez-Sanchez. Micropropulsion system selection for precision formation flying satellites. In *Proceedings of the 37th AIAA/ASME/SAE/ASEE Joint Propulsion Conference and Exhibit*, AIAA paper 2001-3646, Salt Lake City, UT, 2001.

[62] C. D. Brown. *Spacecraft propulsion.* AIAA, 1995.

[63] M. Parker, D. Thunnissen, J. Blandino, and G. Ganapathi. The preliminary design and status of a hydrazine millinewton thruster development. In *Proceedings of the 35th AIAA/ASME/SAE/ASEE Joint Propulsion Conference and Exhibit*, AIAA paper 1999-2596, Los Angeles, CA, 1999.

[64] A. Genovese, S. Maruccio, and M. Andrenucci. Experimental characterization of FEEP emitters. In *Proceedings of the 2nd European Spacecraft Propulsion Conference*, ESA SP-398, Noordwijk, The Netherlands, 1997.

[65] F. M. White. *Viscous fluid flow.* McGaw-Hill, 1991.

[66] A. A. Alexeenco, D. A. Levin, S. F. Gimelshein, R. J. Collins, and B. D. Reed. Numerical modeling of axisymmetric and three-dimensional flows in microelectromechanical systems nozzles. *AIAA Journal*, 40:897–904, 2002.

[67] K. H. Schoenbach, A. El-Habachi, M. M. Moselhy, W. Shi, and R. H. Stark. Microhollow cathode discharge excimer lamps. *Physics of Plasmas*, 7:2186–2191, 2000.

[68] M. Radmilovic-Radjenovic and B. Radjenovic. A particle-in-cell simulation of the high-field effect in devices with micrometer gaps. *IEEE Transactions on Plasma Science*, 35:1223–1228, 2007.

[69] G. J. M. Hagelaar and L. C. Pitchford. Solving the Boltzmann equation to obtain electron transport coefficients and rate coefficients for fluid model. *Plasma Sources Science and Technology*, 14:722–733, 2005.

[70] A. V. Phelps and Z. L. Petrovic. Cold-cathode discharges and breakdown in argon: surface and gas phase production of secondary electrons. *Plasma Sources Science and Technology*, 8:R21–R44, 1999.

[71] R. Kee, G. Dixon-Lewis, J. Warnatz, M. Coltrin, and J. Miller. A fortran computer code package for the evaluation of gas-phase multicomponent transport properties. Technical report, Sandia Report SAND86-8246, 1995.

[72] Z. Donkó. Apparent secondary-electron emission coefficient and the voltage-current characteristics of argon glow discharges. *Physical Review E*, 64:026401, 2001.

[73] B. Lay, R. S. Moss, S. Rauf, and M. J. Kushner. Breakdown processes in metal halide lamps. *Plasma Sources Science and Technology*, 12:8–21, 2003.

[74] G. J. M. Hagelaar and G. M. W. Kroesen. Speeding up fluid models for gas discharges by implicit treatment of the electron energy source term. *Journal of Computational Physics*, 159:1–12, 2000.

[75] D. L. Scharfetter and H. K. Gummel. Large-signal analysis of a silicon Read diode oscillator. *IEEE Transactions on Electron Devices*, 16:64– 77, 1969.

[76] E. P. Hammond, K. Mahesh, and P. Moin. A numerical method to simulate radio-frequency plasma discharges. *Journal of of Computational Physics*, 176:402–429, 2002.

[77] J. H. Ferziger and M. Peric. *Computational Methods for Fluid Dynamics*. Springer, 1997.

[78] S. Mahadevan. Simulation of supersonic flow phenomena in the presence of direct-current surface plasma actuators. Master's thesis, The University of Texas at Austin, 2006.

[79] S. Mahadevan and L. L. Raja. Simulations of glow discharge phenomena in air for high-speed flow control. In *Proceedings of the 46th AIAA Aerospace Sciences Meeting and Exhibit*, AIAA paper 2008-1093, Reno, NV, 2008.

[80] M.-S. Liou and C. J. Steffen. A new flux-splitting scheme. *Journal of Computational Physics*, 107:23–39, 1993.

[81] V. Venkatakrishnan. Convergence to steady state solutions of the Euler equations on unstructured grids with limiters. *Journal of Computational Physics*, 118:120–130, 1995.

[82] S. Balay, K. Buschelman, W.D. Gropp, D. Kaushik, M.G. Knepley, L.C. McInnes, B.F. Smith, and H. Zhang. PETSc Web page, 2001. http://www.mcs.anl.gov/petsc.

[83] D. D. Hsu and D. B. Graves. Microhollow cathode discharge stability with flow and reaction. *Journal of Physics D: Applied Physics*, 36:2898–2907, 2003.

[84] I. Revel, L. C. Pitchford, and J.-P. Boeuf. Calculated gas temperature profiles in argon glow discharges. *Journal of Applied Physics*, 88:2234–2239, 2000.

[85] Q. Wang, D. J. Economou, and V. M. Donnelly. Simulation of a direct current microplasma discharge in helium at atmospheric pressure. *Journal of Applied Physics*, 100:023301, 2006.

[86] H. W. Ellis, R. Y. Pai, E. W. McDaniel, E. A. Mason, and L. A. Viehland. Transport properties of gaseous ions over a wide energy range. *Atomic Data and Nuclear Data Tables*, 17:177–210, 1976.

Vita

Thomas Dominique Deconinck was born in Ottignies-Louvain-la-Neuve, Belgium on March 10, 1982, the son of Jean-Marie Deconinck and Michèle Pétillon. After completing high school at Sint-Jan Berchmanscollege, Brussels, Belgium, he entered the Université Catholique de Louvain in 1999. He received the degree of Ingénieur Civil in Electo-Mechanical Engineering from the Université Catholique de Louvain in June 2004. He entered The Graduate School at The University of Texas at Austin in August 2004.

Permanent Address: 29, Rue malgré Madame
1400 Nivelles
Belgium

This dissertation was typeset with LaTeX 2ε[1] by the author.

---

[1] LaTeX 2ε is an extension of LaTeX. LaTeX is a collection of macros for TeX. TeX is a trademark of the American Mathematical Society. The macros used in formatting this dissertation were written by Dinesh Das, Department of Computer Sciences, The University of Texas at Austin, and extended by Bert Kay, James A. Bednar, and Ayman El-Khashab.